

Electronic Thesis and Dissertation Repository

1-10-2017 2:30 PM

Full-Waveform Inversion with Scaled-Sobolev Preconditioning Applied to Vibroseis Field Data

Benjamin Paul Consolvo
The University of Western Ontario

Supervisor
Pratt, R. Gerhard
The University of Western Ontario

Graduate Program in Geophysics
A thesis submitted in partial fulfillment of the requirements for the degree in Master of Science
© Benjamin Paul Consolvo 2017

Follow this and additional works at: <https://ir.lib.uwo.ca/etd>



Part of the [Geophysics and Seismology Commons](#)

Recommended Citation

Consolvo, Benjamin Paul, "Full-Waveform Inversion with Scaled-Sobolev Preconditioning Applied to Vibroseis Field Data" (2017). *Electronic Thesis and Dissertation Repository*. 5199.
<https://ir.lib.uwo.ca/etd/5199>

This Dissertation/Thesis is brought to you for free and open access by Scholarship@Western. It has been accepted for inclusion in Electronic Thesis and Dissertation Repository by an authorized administrator of Scholarship@Western. For more information, please contact wlsadmin@uwo.ca.

Abstract

I present an application of a high-resolution subsurface imaging technique known as “full-waveform inversion” (FWI) to a vibroseis seismic dataset from eastern Ohio, USA. The data were collected over a crooked line with rough topography, 3.5 km maximum offsets, and no significant frequency content below 12 Hz. These parameters present challenges to obtaining quality images from FWI. The use of a preconditioner—the ‘scaled-Sobolev preconditioner’ (SSP - [Zuberi and Pratt, 2017](#))—on the gradient of the misfit functional was key to obtaining low wavenumbers without discarding high wavenumbers. The results represent the first successful application of FWI with the SSP to a field dataset, with a high-resolution image that generally matches the trends of the Big Injun sand and Berea sandstone layers at the survey location. The novel FWI results confirm the absence of small scale structure (including the lack of visible faults) in the first 0.66 km.

Keywords: Ohio, Utica Shale, Seismic Exploration, Laplace-Fourier, Berea Sandstone, Big Injun Sand

Statement of Co-Authorship

The material presented in this thesis has been previously published in a condensed form as an extended abstract ([Consolvo et al., 2017](#)), and furthermore an extended version will be submitted to a peer-reviewed journal. The co-authors involved are M.A.H. Zuberi, PhD candidate at the University of Western Ontario, Dr. R. Gerhard Pratt, professor at the University of Western Ontario, and Dr. Peter W. Cary, Chief Processing Geophysicist at Arcis Seismic Solutions, A TGS Company. M.A.H. Zuberi is responsible for the development of the ‘scaled-Sobolev preconditioner’ (SSP) for the gradient. He formulated the mathematics and wrote the Fortran code necessary to implement SSP. He also has provided input on the theory sections I have written concerning SSP. Dr. R. Gerhard Pratt provided the instruction necessary to run his FWI code *fullwv*, provided the computing resources and lab space at the University of Western Ontario, and provided feedback on my final thesis. Dr. Peter W. Cary provided the field seismic data necessary to run all of the FWI tests, and input on my final thesis. Arcis distributed some of their internally processed data from the same survey, up to post-stack time migration. The reflection processing section is a compilation of my own work up to pre-stack depth migration, and some of the previous work completed by Arcis. All of the data analysis is my own work.

Acknowledgements

It is right that we should be thankful, for we have been given much. At the outset, I must admit that it is nearly impossible for me to properly acknowledge the many people who helped me during my degree. But here is my best shot. I first must thank my supervisor and co-author, Gerhard Pratt. From our first phone conversation in the spring of 2015 to the final submission of my thesis, he has been there every step of the way. Gerhard has made it a point to meet with me on a regular basis, something I cherish. He is also an excellent teacher in the classroom. I worked for him as a Teaching Assistant (TA) for the Geophysics Field School course in the fall of 2016 and 2017. During my time as a student, Gerhard juggled multiple roles including department chair and professor. Among his most notable traits in my mind aside from his great intellect are his compassion and ability to work with others. Throughout my degree, he was able to gently push me to better myself in my work. He is very well known in the field of geophysics, and more specifically in the field of full-waveform inversion (FWI). He is in large part responsible for bringing FWI to bear on the seismic exploration industry within oil and gas, yet he remains humble. I thank him for the use of his code *fullwv* to complete my tests in FWI. He has played the biggest role for me in ensuring that both the technical content and writing were of high caliber. Gerhard was my supervisor, but I also consider him a friend. On multiple occasions, he invited students into his home, a testament to his hospitality.

I thank the National Sciences and Engineering Research Council of Canada (NSERC) for a Discovery Grant given to Gerhard, which has provided some of the financial support required for my research in 2015-2017. I also would like to thank the Ontario government in partnership with the University of Western Ontario for providing me with an Ontario Graduate Scholarship (OGS), a significant portion of my financial support in 2016-2017. I must also thank ExxonMobil and Chevron, who on two separate occasions sponsored my participation in programs that were of significant value to my education in geophysics and my career development: in 2016, I attended the SEG/ExxonMobil Student Education Program and SEG Annual Meeting in Dallas, Texas; and in 2017, I attended the SEG/Chevron Student Leadership Symposium and SEG Annual Meeting in Houston, Texas. I am also grateful to the Canadian Society of Exploration Geophysicists (CSEG), for giving me the Bill Nickerson Education Award, a sponsored a trip to Calgary, Alberta, in 2017

to attend the 5 full days of geoscience courses taught by professors and industry professionals.

Countless helpful conversations occurred within the confines of Gerhard's research lab at the University of Western Ontario. The first of those helpful conversations that I must acknowledge are those I had with my co-author, Akbar Zuberi. Akbar was not only willing to help, but also a great teacher. I consider Akbar as one of the most mathematically rigorous individuals I have ever met—what a pleasure it has been to work alongside and learn from him during his PhD degree. Only a desk away from me, Akbar had an enormous influence on my academic research during my degree. I thank him for letting me apply his new scaled-Sobolev preconditioning (SSP) technique to a field data set, and for our many discussions that brought me up to speed in geophysics. I consider Akbar a friend. I thank Shaun Hadden for his review of my written work, his many suggestions to me during the completion of his Master's degree, and of course his friendship. My appreciation also goes out to Brendan Smithyman and Felix Hlousek for their helpful suggestions to me in the lab while they were here. I must also note that Brendan, along with another past student of Gerhard's, Rie Kamei, provided valuable work on FWI of land data. Many of the ideas presented in their papers provided me with a foundation for my research. Behind the scenes, Bernie Dunn (our systems administrator) made sure that all of the computer systems were updated and useable, including Landmark's "Y2K Tested" ProMAX software running on our precious Sun microsystems desktop computer.

Outside of Gerhard's research lab, I gained many valuable friendships who were fellow students, employees, and faculty at Western. These friends make up a circle of people who supported me in very important ways during the writing of my thesis. I thank Marie Schell for her support. For most of my time at Western, Marie worked in the Administrative Officer position for the department of Earth Sciences. But she was often described as the 'heart of the department'. I thank her for her prayers and her conversations with me. I thank Neil Banerjee for his mentorship and for chairing my thesis examination. I was a Teaching Assistant (TA) in one of Neil's undergraduate geology courses. I thank the special group of students who worked and excelled with me to compete in the 2016 AAPG Imperial Barrel Award, a 6-week seismic interpretation competition: Michelle MacRae, John Onwuemeka, Simon Thorpe, and Krista Kaski. I also must thank Burns Cheadle, the faculty member who guided us during this challenge. I wish to extend thanks to Patricia Corcoran, who I felt was one of the best university professors I have had. I also thank Ariel Nuñez, Tim Landry, Tim and Kim Parker, and Kyle Cameron.

A number of organizations provided data and software for my study. I want to acknowledge Peter Cary at Arcis for partnering with Gerhard at Western to provide Firestone 2D-3C, the seismic data I used for my study. I also would like to acknowledge Tidelands Geophysical Company who acquired the data in 2013. I am also indebted to the following companies: Schlumberger who provided free licenses of VISTA Seismic Processing software, GeoTomo for TomoPlus, Landmark for

SeisSpace ProMAX, INT for HTML5Viewer, and Shearwater GeoServices for Reveal/OpenCPS. The people involved in the support of these packages respectively were Gary Engler, Steve Syme, Marty Dyess, Curtis Childs, and Kent Stevens. Working with new software can be difficult, but the countless hours that these five individuals provided me made the learning much more manageable. I also thank ESRI for ArcGIS, and IHS Markit for Petra. I thank Biondo Biondi at the Stanford Exploration Project for his publicly available seismic processing package, Madagascar; and likewise John W. Stockwell, Jr. and Jack K. Cohen at the Center for Wave Phenomena at Colorado School of Mines for their publicly available package, Seismic Unix. I thank Romain Brossier of the SEISCOPE consortium for sharing his 3D elastic FWI code near the end of my studies, though I was not able to make as much use of it as I would have liked.

From January 30th to June 2nd of 2017, I interrupted my degree to complete a geophysics internship on an FWI research team at ExxonMobil Upstream Research Company in Houston. During my time at ExxonMobil, I learned a great deal about how FWI is used in industry and what top level research in the field looks like. The knowledge I gained there informed how I wrote about FWI in my thesis. I want to mention that my thanks go out to my internship mentor, Tetyana Vdovina, for her patience and countless hours with me, pouring over FWI results. My thanks also go to the many ExxonMobil employees who made an impact on me, including Gboyega Ayeni, Anatoly Baumstein, Hendrik Braaksma, Valeriy Brytik, Olivier Burtz, William Burnett, Glenn and Lorie Bear, Bill Curry, John Eastwood, Steve Gagnon, David Gaines, Craig Hyslop, Yaofeng He, Andy Kositsky, Spyros Lazaratos, Sunwoong Lee, Xu Li, Jonathan Liu, Rongrong Lu, Carey Marcinkovich, Ramesh Neelamani, Partha Routh, Bob Sirianni, Jacob Violet, Eric Wildermuth, Bram Willemsen, and Sary Zantout. My particular thanks to Alex Martinez for his practical suggestions on improving my thesis. I also thank the friends and immense support I received in Houston from Alex Edmonds, Jacob Waters, and Brad Waters.

There were a number of others who were instrumental in the writing process of this thesis. I thank Hugh Geiger for his review of both the EAGE abstract (now published - [Consolvo et al., 2017](#)) and my thesis. Without Hugh, I also likely would not have known about the opportunity to work with Gerhard. I also thank the following people for their review and helpful feedback on my thesis: geophysicist Andreas Cordsen, Peter Cary, my uncle (and hydrogeologist) Curtis Consolvo, and my brother (and geotechnical engineer) Samuel Consolvo. I thank my examining committee for helping me to write more clearly for a wider audience: Burns Cheadle, Jason Gerhard, and Robert Shcherbakov. Last but certainly not least, I would like to thank the rest of my family for their continuous support of me during my degree: my father Bill, my mother Becky, and my sister Kelley. What a treasure it was to have had such loving people around me. I eagerly anticipate my career in geophysics.

Table of Contents

Abstract	ii
Statement of Co-Authorship	iii
Acknowledgements	iv
List of Tables	x
List of Figures	xi
List of Appendices	xvii
List of Abbreviations, Symbols, Nomenclature	xviii
1 Introduction	1
1.1 Common midpoint (CMP) seismic reflection method	1
1.1.1 Acquisition of seismic data	2
1.1.2 Conventional velocity model-building and seismic processing	4
1.2 Literature review	5
1.3 Goals of thesis and proposed solutions	6
1.4 Structure of thesis	8
2 Background Theory	10
2.1 3D travelt ime tomography	10
2.1.1 ‘Objective function’ vs. ‘misfit functional’	11
2.1.2 Objective function	11
2.1.3 Inversion algorithm	13
2.2 Full-waveform inversion (FWI)	14
2.2.1 Forward modelling	14
2.2.2 Misfit functional	16
2.2.3 Gradient	17

2.2.4	Scaled-Sobolev preconditioner (SSP)	20
2.2.5	Source inversion	21
2.3	Computational environment	22
3	Firestone 2D-3C Case Study	23
3.1	Survey overview	23
3.1.1	Background geology	25
3.1.2	Rose Reynolds well and Raymond Goddard well	31
3.1.3	Survey parameters	35
3.1.3.1	P- and S-waves	35
3.1.4	Seismic data preprocessing	38
3.2	Velocity model building and validation	40
3.2.1	Applying 3D first-break traveltimes tomography	42
3.2.2	Applying 2D FWI with the SSP	47
3.2.2.1	Multi-scale strategy	47
3.2.2.2	Modelling parameters	47
3.2.2.3	Results	48
3.2.3	Validation of final results	54
3.2.4	Geological interpretation	65
3.3	Reflection processing	65
3.3.1	Workflows	68
3.3.2	Geometry	71
3.3.3	Time Processing	74
3.3.4	Depth Processing	77
3.3.5	Interpretation	81
4	Conclusions and Future Directions	86
	Bibliography	88
	Appendix A Wave Equations	94
A.1	Elastic media	94
A.1.1	Stress	95
A.1.2	Strain	96
A.1.3	Hooke's law and elastic tensor	100
A.1.4	Equations of motion and wave equations	104
A.1.4.1	3D VTI elastic wave equations	105

A.1.4.2	VTI Thomsen parameters	106
A.1.4.3	2D VTI elastic wave equations	107
A.1.4.4	3D isotropic elastic wave equations	108
A.1.4.5	Thomsen parameters simplified with isotropic medium	111
A.1.4.6	2D isotropic elastic wave equations	112
A.2	Acoustic Wave Equation	112
Appendix B	Well Data	116
Curriculum Vitae		127

List of Tables

3.1	3D travelttime tomography strategy	42
3.2	2D FWI strategy	47
A.1	Number of independent parameters for the elastic tensors described with increasing order of symmetry.	104
B.1	Top-of-formation data in a south-to-north fashion are displayed here. Depths have been converted from depth in feet below kelly bushing (KB) to a common depth in metres below a datum of 426.7 m above mean sea level, the same datum used throughout the study. The ‘KELLY_BUSHING_NEW’ row at the top of the table presents the KB values referenced to the new datum. The numbers in brackets (#) indicate that values have been interpolated from surrounding data to build the cross-section. The key formations of interest are highlighted in yellow. Figure 3.5 shows the associated cross-section.	117
B.2	Top-of-formation data in a west-to-east fashion are displayed here. Depths have been converted from depth in feet below kelly bushing (KB) to a common depth in metres below a datum of 426.7 m above mean sea level, the same datum used throughout the study. The ‘KELLY_BUSHING_NEW’ row at the top of the table presents the KB values referenced to the new datum. The numbers in brackets (#) indicate that values have been interpolated from surrounding data to build the cross-section. The key formations of interest are highlighted in yellow. Figure 3.6 shows the associated cross-section.	122

List of Figures

1.1	Common midpoint (CMP) seismic reflection method. Sources are shown as stars and receivers are shown as triangles. Multiple source-receiver pairs image the same point in the subsurface. The solid line is a representation of the Earth's topographic surface, and the dotted line is a representation of a reflection boundary between two subsurface rock layers with velocities v_1 and v_2 . Image from Brenders (2011)	2
1.2	Raw seismic shot gather from Firestone seismic reflection survey with labels. . . .	3
1.3	A typical velocity analysis or 'picking' display for a seismic processor. A processor may pick the velocities on the semblance velocity plot (c) to flatten the CMP gathers (a), advancing through the stacked seismic section (b). Data from TGS. . .	4
2.1	Visual representation of the computation of the gradient of the misfit functional, requiring that the forward-propagated wavefield be multiplied with the back-propagated residual wavefield. The source is represented by a star, and receivers are represented by squares.	20
3.1	Profile of a typical Utica shale well in east central Ohio. Modified from Ohio Division of Geological Survey (2011)	24
3.2	Geologic map and cross-section of Ohio. The Firestone survey area is in Carroll County (red outline). The Berea sandstone can be found at a depth of approximately 0.4 km in the Firestone survey area. Map modified from Ohio Division of Geological Survey (2006)	26
3.3	Map of predominant near-surface (< 0.3 km) lithology in the state of Ohio, USA. The survey covers an area laden with siltstone, and the seismic line appears to run along geologic strike. Map data from Nicholson et al. (2005)	27
3.4	Magnetic anomaly map of Ohio, with data taken from Hildenbrand et al. (1981) . . .	28
3.5	Cross-section S-N, along seismic line. The red box indicates the extent of the FWI velocity model. The location of the cross-section is indicated on Figure 3.10. Data courtesy of ODNR Oil and Gas Resources Management (2016)	29

3.6	Cross-section W-E, perpendicular to seismic line. The location of the cross-section is indicated on Figure 3.10. Data courtesy of ODNR Oil and Gas Resources Management (2016)	30
3.7	Rose Reynolds (RR) digital well data for the entire depth of the log. The right-most column shows top-of-formation depths, based on observed top-of-formation data and referenced to the common datum used in this study. The location of the well is shown on Figure 3.10.	32
3.8	Rose Reynolds (RR) digital well data for the first 0.66 km (primary depth of investigation). The right-most column shows top-of-formation depths, based on top-of-formation data and referenced to the common datum used in this study. The location of the well is shown on Figure 3.10.	33
3.9	Raymond Goddard (RG) digital well data for the entire depth of the log. The right-most column shows top-of-formation depths, based on top-of-formation data and referenced to the common datum used in this study. The location of the well is shown on Figure 3.10.	34
3.10	Detailed map of survey area. Many subsequent plots can be geographically situated on this map. Numerous active and inactive oil and gas wells are displayed as blue dots in the area (ODNR Oil and Gas Resources Management, 2016), some dating back to the early 1900s. Many of the more recently drilled wells 2010 and later have used hydraulic fracturing and horizontal drilling to capture higher quantities of oil and gas from the Utica shale reservoir.	36
3.11	Shot and receiver elevation (negative elevation is above mean sea level). The vertical axis has been stretched significantly to show variation.	37
3.12	(a) Raw shot gather and (b) preprocessed shot gather # 276 at 8.8 km along the line (located on Figure 3.10). Shot gathers have been trace normalized for display purposes. First break picks are in yellow.	38
3.13	Offset percentage error from the projection of 3D to 2D offsets. Data with offset error greater than 3% were discarded.	39
3.14	Two examples of the Fourier transform of the time data used as the input for the FWI code <i>fullwv</i> : (a) 12 Hz observed data and (b) 26 Hz observed data. Most sources had 438 associated receivers. The white gaps represent the areas where data were discarded due to the projection from 3D to 2D, and the regions with no data due to limited offset coverage. Data have been trace normalized for display purposes.	41

3.15	Common first-break pick plot. The vertical axis represents the time of the first-break picks on the shot gathers, and the horizontal axis represents the source-receiver offset distance. The coloration represents the density of first-breaks at a specific time and offset. The initial model for travelttime tomography was built by tracing along common picks.	43
3.16	Starting velocity model for travelttime tomography. The cube has been ‘sliced’ at $x = 3.76$ km, $y = 0.35$ km, and $z = 0.05$ km. The light grey colour represents the air layer with a velocity of 340 m/s, but no rays were permitted to travel in the air during tomography.	44
3.17	In map view after coordinate rotation, the 3D travelttime RMS misfit (in ms) at each shot location along the crooked line before tomography (top), and after tomography (bottom). The x coordinate represents the inline direction, and the y direction represents the crossline direction.	45
3.18	The ray density count shows that the first-break rays reached a maximum depth 0.58 km. The cube has been ‘sliced’ to show the ray count at $x = 3.76$ km, $y = 0.35$ km, and $z = 0.17$ km.	46
3.19	Example offset taper filter used with corners A, B, C, and D.	48
3.20	Gradients for 12-14 Hz: (a) raw gradient at iteration 1, (b) preconditioned (SSP) gradient at iteration 1, (c) raw gradient at iteration 100, (d) preconditioned (SSP) gradient at iteration 100, and (e) conjugate gradient at iteration 100.	49
3.21	Progression of subsurface velocity models through FWI: (a) starting model for FWI after travelttime tomography, (b) after 12-14 Hz (iteration 100), (c) after 15-20 Hz (iteration 200), and (e) final model after 21-26 Hz (iteration 233). The dotted lines indicate the position of the 1D trace that was used for comparison to the sonic log; the thick solid black line indicates the depths where the sonic log has data (below 0.4 km).	51
3.22	Velocity model difference plots: (a) the result of Figure 3.21b - 3.21a, (b) the result of 3.21c - 3.21b, and (c) the result of 3.21d - 3.21c. By keeping a consistent scale bar here across 3 plots, some values go above and below the values listed here. The left portion of the model remains without meaningful updates, due to a lack of data.	52
3.23	Wavenumber plots: (a) the $k_x \times k_z$ plot of Figure 3.22a, (b) the $k_x \times k_z$ plot of 3.22b, (c) the $k_x \times k_z$ plot of 3.22c. Due to using a smaller SSP scale factor in the z direction (μ_z), the k_z wavenumbers are elongated as compared to the k_x wavenumbers.	53
3.24	Misfit functional decreases in all three blocks of FWI by about 47%. The trends are slightly different because at each block, new frequencies were being introduced in the inversion scheme.	54

3.25	Forward modeled shot # 276: (a) preprocessed data, and (b) from traveltome tomography starting model. The source position is 8.8 km along the line (located on Figure 3.10). Shot gathers have been trace normalized for display purposes. First break picks are displayed in yellow.	56
3.26	Forward modelled shot # 276: (a) after 12-14 Hz FWI (iteration 100), and (b) after 15-20 Hz FWI (iteration 200). The source position is 8.8 km along the line (located on Figure 3.10). Shot gathers have been trace normalized for display purposes. First break picks are displayed in yellow.	57
3.27	Shot # 276: (a) Preprocessed field data, and (b) final forward modelled data after 21-26 Hz FWI (iteration 233). A: The far-offset arrivals come in slightly late in the modelled data. B: The modelled data show a refracted arrival package not present in the field data. C: Multiple reflections occur at the very near surface of the velocity model, where it changes rapidly from 1300 m/s to 2400 m/s. D: A good match in phase exists here between modelled and field data. E: The far offsets on the right hand side show an excellent fit. The source position is 8.8 km along the line (located on Figure 3.10). Shot gathers have been trace normalized for display purposes. First break picks are displayed in yellow.	60
3.28	The Rose Reynolds well showing the original sonic log (black line), a lowpass filter (corners 0 - 0 - 3 - 6 Hz) of the sonic log (red dashed line), the starting velocity model (green line), and the final FWI velocity model (blue line). The location of the well is about 1.5 km away from the survey line (indicated on Figure 3.10). . . .	61
3.29	Sensitivity kernels at (a) the minimum frequency of 12 Hz, and (b) the maximum frequency of 26 Hz. The kernels have a source-receiver offset distance of 2.5 km (70% of maximum offset).	62
3.30	Source inversions: (a) from the starting model, (b) after 12-14 Hz (iteration 100), (c) after 15-20 Hz (iteration 200), and (d) after final 21-26 Hz (iteration 233). The source profiles were trace balanced for display purposes. Progressing from (a) to (d), we see multiple events collapsing to more of a front-loaded single event. The multiple events in (a) appear as multiple ‘reflections’ near 0 s, but in (d) appears more often as a single coherent ‘reflector’ near 0 s.	63
3.31	Final FWI velocity model with (a) seismic stack overlaid, and (b) formations Big Injun sand (yellow) and Berea Sandstone (orange) overlaid. Final FWI velocity model with S-N well tops cross-section (from Figure 3.5) overlaid. Well locations are approximate, due to their crooked traverse on top of the straight (projected) traverse.	64

3.32	Two sample processed shot gathers from the output ‘PPDECON’ delivered by Arcis are shown here. The processed data were used as a starting point for migration work in time and depth. The first shot gather (a) has a blue line that shows an approximate velocity of 4663 m/s on a refracted event, and the second shot gather (b) has a blue hyperbola that shows an approximate NMO velocity of 4028 m/s on a reflected event. The maximum offset from source to receiver is 3.5 km. Shot gathers have been trace balanced for display purposes.	67
3.33	Arcis’ P-wave processing workflow for the Firestone 2D seismic dataset. Left: The output ‘GEOMETRY’ was the dataset used for FWI processing, and the output ‘PPDECON’ (see Figure 3.32) was the dataset used for migration work. Right: Arcis’ workflow output ‘PPPROC MIG’ is its final post-stack migration image, a helpful point of comparison for my work.	69
3.34	My processing workflows for time and depth, beginning from the ‘PPDECON’ data from Arcis’ processing (Figure 3.33). The three outputs of my processing are a pre-stack time migration ‘PSTM’ using Arcis’ NMO velocity model, a pre-stack depth migration ‘PSDM’ using a depth (and interval) converted model from Arcis’ NMO model, and a pre-stack depth migration from topography ‘FWI PSDM’ using a combination of my previous near-surface FWI work and the Arcis depth-interval model.	70
3.35	Crooked line geometry setup in ProMAX. (a) The shot and receiver midpoints are displayed in black. The pink line was picked to bin common mid points (CMPs). (b) 1908 CMP bins (blue boxes) cover the shot and receiver midpoints. The red rectangular box is a zoomed in portion and is shown in Figure 3.36.	72
3.36	A zoomed in portion of Figure 3.35b, showing the shot-receiver midpoints (black) and CMP bins (blue boxes).	73
3.37	Fold chart shows the number of traces in each CMP bin.	74
3.38	(a) The data have been sorted into CMPs with previous processing applied by Arcis. (b) The same CMPs after normal move-out (NMO) and migration were applied. The red and green lines are stretch mutes: the data above the lines were muted just prior to stacking. The offsets were limited from the original maximum of 3.5 km to 1.5 km. The previously hyperbolic reflectors now mostly appear as flat, an indicator of a high-quality RMS velocity model.	75
3.39	(a) Arcis’ post-stack time migration result is a well-resolved image showing clear reflectors. (b) My pre-stack time migration result shows more lateral resolution, but some of the clarity of the first 0 - 300 ms was lost. The time axes represent two-way travel time. The 1908 CMP bins comprise the 16 km seismic line.	76

3.40	(a) Interval- and depth-converted RMS velocity model from Arcis. (b) Smoothed version used for migration ‘PSDM’.	78
3.41	(a) A stitched velocity model of the FWI result in the near-surface (< 0.66 km) and the depth-converted Arcis model at greater depths. (b) Smoothed version used for migration ‘FWI PSDM’. The velocities are much slower in the near-surface as compared to the depth-converted Arcis model in Figure 3.40.	79
3.42	(a) CMPs after NMO correction and migration from a datum of 426.7 m above sea level, with statics applied, using the depth-converted Arcis velocity model. (b) CMPs after NMO correction and migration from topography using the stitched FWI-Arcis velocity model. The red lines are stretch mutes, applied only before final stacking.	80
3.43	(a) Stacked image after pre-stack depth migration from a datum of 426.7 m above sea level, using a depth-converted RMS velocity model from Arcis. (b) Stacked image after pre-stack depth migration from topography, using the stitched FWI-Arcis model.	81
3.44	Preliminary interpretation of top-of-formations overlaid on final FWI PSDM image.	84
3.45	The bottom 1.2 - 1.9 km portion of the Rose Reynolds well log with formation tops labeled, located 1.5 km away from the projected survey line. The top-of-formation depths are on the right panel, referenced to the FWI velocity model datum (426.7 m above sea level).	85
A.1	Infinitesimally small cube of dimensions $\delta x \times \delta y \times \delta z$, with all nine stress components labelled. Modified from Yilmaz (2001) .	95
A.2	Stress causes slight deformations (strain), depicted here on the $\delta x \times \delta z$ plane: (a) linear ‘stretching’; (b) shearing only; (c) rotation only; (d) combined shearing and rotation. Adapted from Yilmaz (2001) .	98

List of Appendices

Appendix A Wave Equations	94
Appendix B Well Data	116

List of Abbreviations, Symbols, Nomenclature

Traveltime tomography

N_d	Number of receiver locations
N_m	Number of velocity model parameters
N_l	Number of nodes in finite difference model
Φ	Traveltime tomography objective function
\mathbf{m}	Velocity model parameter vector (dimensions $N_m \times 1$)
w	weighting factor between the average slowness misfit and apparent slowness misfit
\mathbf{s}	Traveltime data vector (dimensions $N_d \times 1$)
$\bar{\mathbf{s}}$	Average slowness data vector (dimensions $N_d \times 1$)
$\bar{\mathbf{L}}$	Predicted average slowness data vector (dimensions $N_d \times 1$)
$\hat{\mathbf{s}}$	Apparent slowness data vector (dimensions $N_d \times 1$)
$\hat{\mathbf{L}}$	Calculated apparent slowness data vector (dimensions $N_d \times 1$)
\mathbf{R}	Spatial derivative operator matrix (dimensions $N_l \times N_l$)
ℓ	Ray length
b	Smoothing trade-off parameter
D_x	Differential operator for traveltime with respect to receiver distance x
C_ℓ	Scaling operator to traveltime with corresponding ray length ℓ
\mathbf{A}	Average-slowness sensitivity matrix (dimensions $N_d \times N_m$)
\mathbf{B}	Apparent-slowness sensitivity matrix (dimensions $N_d \times N_m$)
χ	Damping term

η Empirical parameter (approximately 0.1)

\mathbf{I} Identity matrix (dimensions $N_m \times N_m$)

Full-waveform inversion

N_d Number of receiver locations

N_m Number of velocity model parameters

N_l Number of nodes in finite difference model

x Spatial variable along the inline direction

y Spatial variable in the crossline direction

z Spatial variable depth

ω Real-valued angular frequency ($= 2\pi f$, where f is frequency)

Ω Complex-valued angular frequency

t Time

τ Real-valued decay constant

c Complex-valued primary-wave velocity

i $\sqrt{-1}$

ρ Density

Q Quality factor

\mathbf{S} Wave equation impedance matrix (dimensions $N_l \times N_l$)

\mathbf{u} Predicted discretized wavefield vector (dimensions $N_l \times 1$)

\mathbf{f} Source terms vector (dimensions $N_l \times 1$)

E Misfit functional

\mathbf{d} Observed data vector (dimensions $N_d \times 1$)

$\delta\mathbf{d}$ Data residuals vector (dimensions $N_d \times 1$)

θ_u Phase of the calculated seismic wavefield

θ_d Phase of the observed seismic wavefield

\Im Imaginary component

\mathbf{m} Velocity model parameter vector (dimensions $N_m \times 1$)

α	Step length
\mathbf{F}	Matrix of virtual source terms (dimensions $N_l \times N_l$)
\mathbf{J}	Jacobian: Frechét partial derivatives matrix (dimensions $N_m \times N_l$)
∇	Gradient operator
$\nabla_{\mathbf{m}}E$	Gradient of the misfit functional vector (dimensions $N_m \times 1$)
\mathbf{w}	Weighted data residual vector (dimensions $N_l \times 1$)
\mathbf{v}	Back-propagated residual wavefield vector (dimensions $N_l \times 1$)
$\boldsymbol{\gamma}$	Preconditioned conjugate gradient of the misfit function vector (dimensions $N_m \times 1$)
μ_0, μ_x, μ_z	Scaled-Sobolev scale factors
k_x, k_z	x - and z -wavenumbers
r	Complex-valued source signature scalar
$grid$	Grid size
λ	Wavelength

Appendix A

σ_{ij}	Stress
u	Pressure wavefield
e_{kl}	Strain tensor
e_{xx}, e_{yy}, e_{zz}	Normal strain components
$\theta_{xz}, \theta_{xy}, \theta_{yz}$	Rigid rotational components
c_{ijkl}	Elastic or ‘stiffness’ tensor
$\mathbf{c}^{(\text{TRC})}$	Elastic tensor matrix for triclinic media
$\mathbf{c}^{(\text{MNC})}$	Elastic tensor for monoclinic media
$\mathbf{c}^{(\text{ORT})}$	Elastic tensor matrix for orthorhombic media
$\mathbf{c}^{(\text{VTI})}$	Elastic tensor matrix for verticle transverse isotropic media
$\mathbf{c}^{(\text{HTI})}$	Elastic tensor matrix for horizontal transverse isotropic media
$\mathbf{c}^{(\text{ISO})}$	Elastic tensor matrix for isotropic media
κ	Bulk modulus

μ	Shear modulus
λ	Lamé's modulus of fluid incompressibility
ρ	Density
f	Source term
ω	Real-valued angular frequency ($= 2\pi f$, where f is frequency)
ϵ	Thomsen parameter epsilon
γ	Thomsen parameter gamma
δ	Thomsen parameter delta
v_P	Primary-wave velocity
v_{SV}	Vertical shear-wave velocity
v_{SH}	Horizontal shear-wave velocity
α_0	Thomsen parameter alpha
β_0	Thomsen parameter beta
∇^2	Laplacian operator
Θ	Dilatation (change in volume)
∇	Gradient operator

Appendix B Well Abbreviations

LE	Luce Edward and Carmella and M J 2, API 34019218480000
SB	Schott Bessie I 1, API 34019203020000
ML	Miller 1, API 34019220530000
FW	Fawcett Walter S 1, API 34019201800000
GR	Grunder 6H, API 34019225540000
CC	Carroll County Commissioners 1, API 34019209210000
BC	Brace 1H (Stratigraphic Test), API 34019221320000
RR	Reynolds Rose 1-2, API 34019211900000
SC	Scholes M 4, API 34019216000000
BG	Bowling G and M Unit 1, API 34019211850000

BL Boyle Lloyd and Dorothy 1, API 34019216480000
PR Perry Unit 2S (Stratigraphic Test), API 34019226890000
MD McDaniel Unit 1, API 34019216450000
SF Schmuck Farms 22-14-5 6H, API 340192233330000
HY Harvey 16-14-5 3H, API 34019223010000
ND Neider 10-14-5 8H, API 34019221240000
JO Jones A 33-13-4 10H, API 34019224140000
BN Beadnell A 21-13-4 8H, API 34019223720000

Other Abbreviations

FWI Full-waveform inversion
SSP Scaled-Sobolev preconditioner
3C Three-component
2D Two dimensions
2.5D Two and a half dimensions
3D Three dimensions
S-wave Shear-wave
P-wave Primary- or pressure-wave
NMO Normal move-out
PSDM Pre-stack depth migration
CMP Common midpoint
RMS Root mean square
PSTM Pre-stack time migration
RTM Reverse-time migration
RFWI Reflection full-waveform inversion
LF Laplace-Fourier

Chapter 1

Introduction

Imaging the subsurface of the Earth using controlled-source seismology is an essential tool for oil and gas exploration (eg., [Løseth et al., 2009](#)), civil and geotechnical engineering (eg., [Grandjean, 2006](#)), and crustal-scale investigations (eg., [Operto et al., 2006](#); [Bleibinhaus et al., 2007](#)). The conventional objective of seismic data processing is to create a ‘migrated seismic image’ that can be used to interpret the physical properties and structure of the subsurface. However, the fidelity of the migrated image requires an accurate velocity model that must be determined from the data. In the last two decades, full-waveform inversion (FWI) of seismic data has become accepted as an alternative technique for velocity model building and subsurface imaging ([Virieux and Operto, 2009](#); [Lambaré et al., 2017](#)). One benefit of FWI is that it has the potential to produce an interpretable high-resolution velocity model (image) without a lengthy processing sequence. In this first chapter, I introduce the seismic reflection method, I provide a literature review, I state the problems and aims of this thesis, and I conclude with a brief outline of the material I cover.

1.1 Common midpoint (CMP) seismic reflection method

Controlled-source seismology is a subfield of exploration geophysics in which an artificial energy source is injected into the ground, and the Earth’s response is measured by geophones or ‘receivers’. The ‘common midpoint’ (CMP) seismic reflection method is one of the most reliable methods used for oil and gas exploration without having to drill many (often expensive) holes in the ground. The CMP method can be described pictorially. [Figure 1.1](#) shows the idea behind the CMP method, with many source-receiver pairs collected over a line. The CMP method redundantly samples many subsurface points along reflection boundaries between rock layers. The redundancy over a subsurface point is referred to as “fold.” We may refer to a particular seismic dataset as having “120 fold”, meaning that on average each subsurface point has been sampled 120 times. This redundancy provides i) information on sound wave velocity in the subsurface and ii) multiple

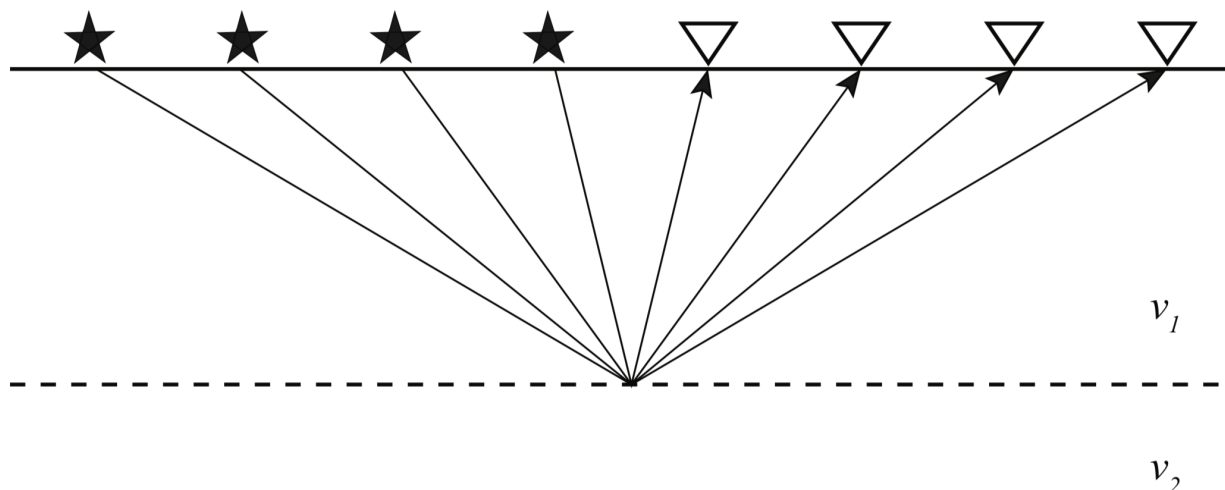


Figure 1.1: Common midpoint (CMP) seismic reflection method. Sources are shown as stars and receivers are shown as triangles. Multiple source-receiver pairs image the same point in the subsurface. The solid line is a representation of the Earth’s topographic surface, and the dotted line is a representation of a reflection boundary between two subsurface rock layers with velocities v_1 and v_2 . Image from [Brenders \(2011\)](#).

inputs for data stacking to improve the signal-to-noise ratio. To reduce what reflection processing may consider “noise” such as ground roll, having high fold typically helps. The problem becomes difficult with multiple reflections from multiple boundaries, and is further complicated by different kinds of sound waves that propagate in the subsurface. The target depth, the surface conditions, and the geological complexity dictate how a survey should be acquired. Two common adjustments to a survey would include changing the source-to-receiver offsets, and changing the spatial sampling density of the sources and the geophones.

Broadly, there are three steps that must be taken to obtain a ‘seismic image’: (1) acquiring seismic data with the CMP method, (2) building a velocity model, and (3) processing the seismic data to produce a final image. Step (3) often involves a process known as ‘migration’, where seismic events are re-located from their recorded (geometrical) position in time to their correct subsurface position in the image. The advantage of FWI over conventional reflection processing is that it offers the potential to skip step (3) entirely, and limit the amount of time spent on (2); this advantage arises as FWI has the potential to produce a high-resolution velocity image directly (requiring only a sufficiently accurate starting velocity model).

1.1.1 Acquisition of seismic data

Seismic data are acquired in the field both on land and in marine environments, using similar principles but somewhat different hardware. Seismic data are widely used for the purpose of hydrocarbon exploration. Here I describe only land acquisition, as my thesis only focuses on land

data. To acquire controlled-source seismic data, an energy point source (such as dynamite or a vibrating truck) is placed on the ground, and a line or array of receivers are placed on the ground to measure the response of the Earth. In order to cover a large area or a long line, the whole array of sources and receivers are moved or “rolled out” continuously, to collect multiple subsurface measurements.

Raw seismic data are collected and displayed in what is called a ‘shot gather’, in which all active receiver time records are depicted as a function of distance from the source (or, ‘offset’). Figure 1.2 shows a sample shot gather from the Ohio survey in this thesis with the source location in the middle of the image, and 218 active receivers on each side of the source location (for a total of 438). The time axis shows the recorded arrivals as a function of time, with increasing source-receiver offset distance. Each successive sound wave has had to travel a longer distance in the subsurface, and thus the event takes longer to be recorded by each geophone with increasing offset. The image has been labeled with a few well-known types of waves that propagate in the subsurface, including P-wave refractions, P-wave reflections, and ground roll.

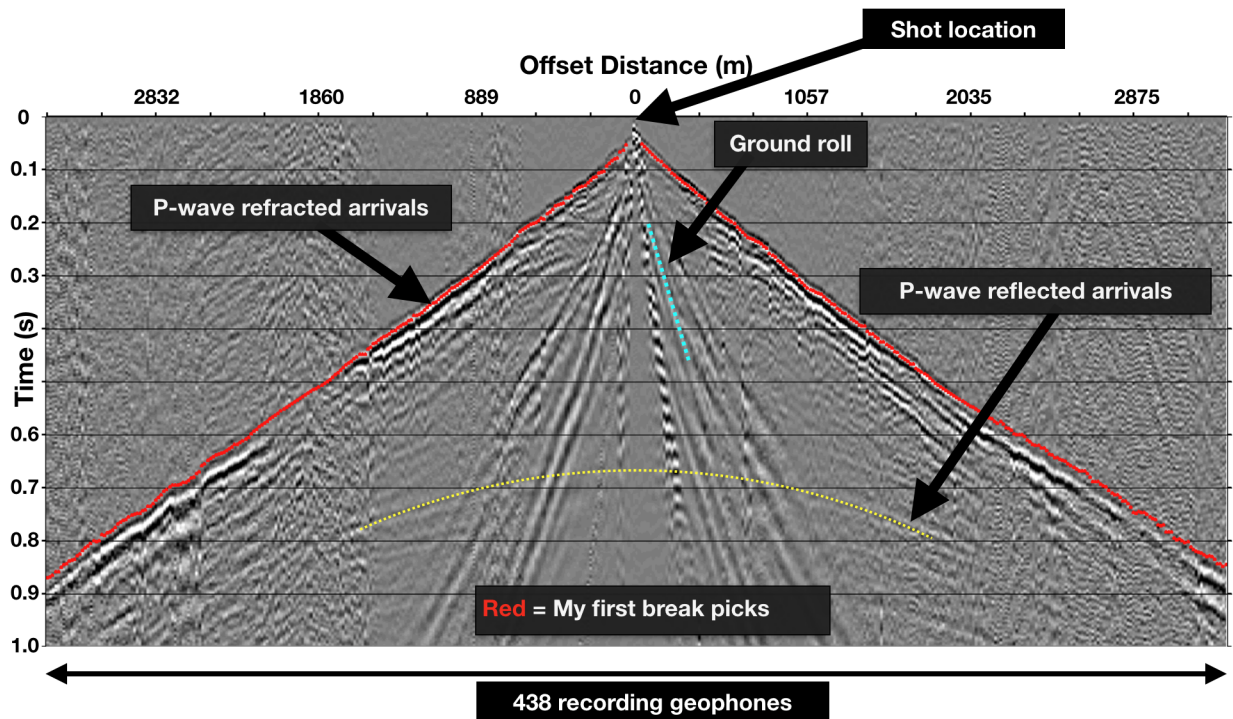
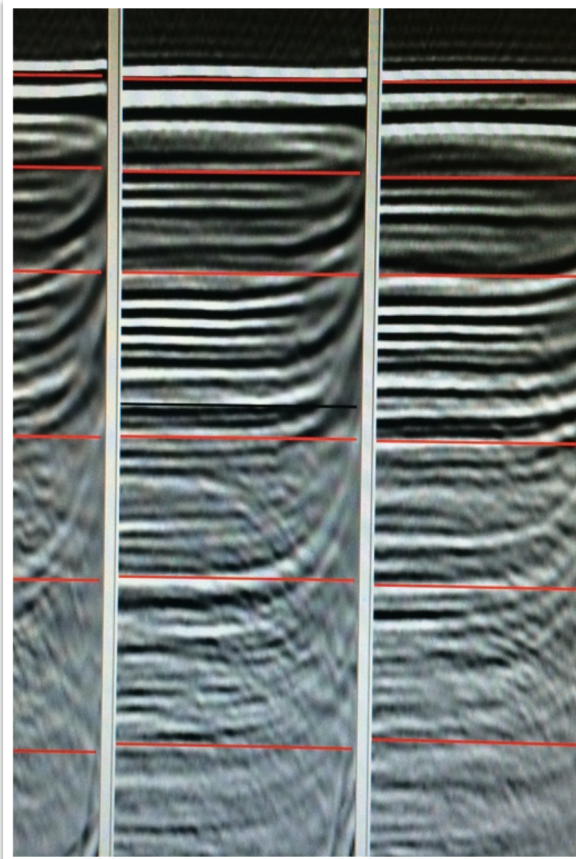
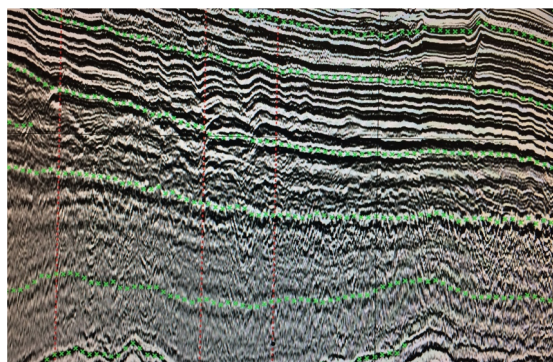


Figure 1.2: Raw seismic shot gather from Firestone seismic reflection survey with labels.

(a) CMP Gathers:



(b) Seismic Stack:



(c) Semblance Velocity Spectra:

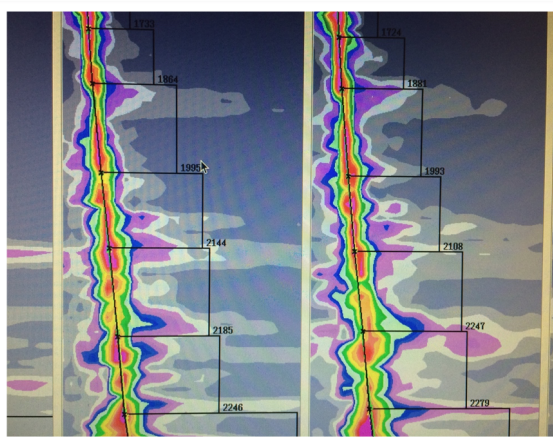


Figure 1.3: A typical velocity analysis or ‘picking’ display for a seismic processor. A processor may pick the velocities on the semblance velocity plot (c) to flatten the CMP gathers (a), advancing through the stacked seismic section (b). Data from TGS.

1.1.2 Conventional velocity model-building and seismic processing

One common technique used to build a velocity model in a typical seismic time processing workflow is to use ‘velocity analysis’ or ‘velocity picking’. The goal in picking velocities is to create a velocity model that effectively flattens the seismic events on a CMP gather, so that the gathers can be ‘stacked’. The end result is a final stacked image with relatively coherent-looking reflectors (Figure 1.3). The result of the process of picking velocities is a final velocity model in time. [Yilmaz \(2001\)](#) describes in greater depth this process of velocity analysis. Velocity picking is a very time-consuming process, usually laden with many iterations. The advantage of an FWI workflow is that no velocity picking must take place; instead, the velocity model is inverted for using an algorithm that uses the raw seismic data directly. Beyond that, in conventional seismic processing, there is a significant amount of human effort to arrive at a final seismic image, usually exceeding the time required for FWI. As previously noted, FWI has the additional potential of resolving such

a high-resolution velocity model that the model itself can be used as an image for interpretation.

1.2 Literature review

FWI is an ill-posed nonlinear problem that requires the starting velocity model to satisfy the ‘half-cycle’ criterion of the true model in order to converge to the global minimum solution (Sirgue and Pratt, 2004). The half-cycle criterion is satisfied when the starting velocity model generates synthetic seismic data that are (on average) only a half of a cycle or less away from the observed data. The use of first-break traveltimes tomography is an important tool to find such an appropriate starting model for FWI. An important observation by Lailly (1983) and Tarantola (1984) was made when they saw that the FWI problem strongly resembled the Kirchhoff migration problem based on the imaging principle of Claerbout (1971; 1976). Lailly and Tarantola cast their FWI problem in the time domain, using the acoustic wave equation. Mora (1987) extended FWI to the elastic wave equation, also in the time domain. Pratt and Worthington (1990), Pratt et al. (1998) and Pratt and Shipp (1999) paved the way for a frequency-domain approach to FWI, using the acoustic wave equation. Virieux and Operto (2009) provided an excellent overview of work completed in FWI, and the ongoing challenges. Significant leaps in computational power have allowed the problem of 3D FWI to become tractable in recent years. 3D acoustic FWI has been successfully implemented on field data in the time domain (eg., Vigh and Starr, 2008; Plessix and Perkins, 2010; Plessix et al., 2012; Lu et al., 2016). Sirgue et al. (2009) recently presented an application of their time and frequency combination approach to 3D FWI. Current developments have also made 3D elastic FWI possible, but it is still an ongoing field of research that has not reached maturity (Castellanos et al., 2011; Lu et al., 2013). Vibroseis seismic data are often acquired for the purpose of generating clear reflected arrivals for depth imaging. Typically both refracted energy and far-offsets are discarded before migration, and valuable velocity information for the near-surface is lost in the process. In comparison, the traveltimes tomography and FWI methods I employ are designed to make use of refracted energy and far-offsets to capture high resolution near-surface velocity models.

There are many successful cases of applying FWI to offshore data (Operto et al., 2006; Prioux et al., 2011; Kamei et al., 2012; Warner et al., 2013; Lewis et al., 2014); however, the application of FWI to onshore data is challenging for several reasons including weathering layers in the near-surface distorting the wavefields, rough topography, line crookedness, and coupling issues between source and receiver pairs (Malinowski and Operto, 2008; Kamei et al., 2015). When FWI is used in onshore settings, it is often completed using data acquired by explosive (dynamite) sources (eg., Malinowski et al., 2011; Mothi et al., 2012), which provide low frequency content. It is still quite uncommon to apply FWI to vibroseis data, usually due to the lack of low frequency content.

There have, however, been a handful of studies that have applied FWI to onshore vibroseis data, including work from [Plessix et al. \(2012\)](#), [Smithyman and Clowes \(2012\)](#), and [Adamczyk et al. \(2014\)](#). Without low frequency content and low-wavenumber information, it is difficult to converge on global minimum solutions ([Bunks et al., 1995](#)). To help mitigate convergence problems, multi-scale approaches are often used, starting with low-frequency, low-wavenumber updates, and working up to high-frequency, high-wavenumber updates (eg., [Mao et al., 2012](#)). However, if low frequencies are unavailable, convergence to a solution corresponding to the global minimum is difficult to achieve. When iterating for a nonlinear problem, a common technique applied is ‘gradient descent’ ([Nocedal and Wright, 1999](#)). The goal in gradient descent is to ‘descend’ into the lowest valley of the objective function, or the global minimum. The largest spatial scale is the easiest to systematically search for a global minimum.

The scaled-Sobolev preconditioner (SSP) technique is a new method proposed by [Zuberi and Pratt \(2017\)](#). The SSP is a gradient preconditioner that allows for smooth background updates but without losing the high-wavenumber information. A wavenumber filtering technique or Gaussian smoother will completely eliminate some of the high-wavenumber information early on, which can cause the sharp reflectors to be placed in the wrong position, never to return to the correct position. The SSP technique represents significant leap forward in preserving high-wavenumbers while converging quickly on a global minimum solution with large background updates.

Reflection FWI (RFWI) is an alternative technique that updates the velocities using reflected data rather than focusing on refracted data. In this thesis, reflections are not ignored (through the use of the SSP), but rather refractions are the primary focus of the updates. In many cases, access to long offset refracted data is unavailable, in which case it would be helpful to use the reflections more for the updates. [Yao and Wu \(2017\)](#) showed a successful result on a synthetic dataset using a combination approach between least-squares reverse-time migration (RTM) and reflection FWI. They modified the gradient of the misfit functional to prefer background (low-wavenumber) updates. One difficulty with RFWI is that the data being used are only recorded with limited aperture. The misfit functional for reflection FWI is more underdetermined than for refraction FWI, making it more challenging to converge on the global minimum solution.

1.3 Goals of thesis and proposed solutions

The two primary goals in this thesis are (1) to recover a high-resolution near-surface (0.66 km) velocity model from a field vibroseis dataset, and (2) to demonstrate the success of using FWI with the SSP. The data used in the study were collected along a crooked line, over rough topography, with short (3.5 km) maximum offsets, and no useable frequency content below 12 Hz, presenting significant challenges for FWI. The absence of data below 12 Hz is a significant restriction to

FWI, as higher frequency data are more prone to a phenomenon known as ‘cycle skipping’ than lower frequency data. Cycle skipping occurs when the predicted and observed data differ by more than a half a cycle. If cycle skipping occurs, then the velocity model falls outside of the half-cycle criterion for the seismic waveform. In order to mitigate cycle skipping, I used 3D first-break traveltimes tomography to obtain a starting model for FWI, which results in a velocity model that satisfies as best as possible this criterion.

I used a Laplace-Fourier (LF) implementation of FWI to mitigate nonlinearity in the misfit functional by restricting the inversion to early arrivals and low frequencies first. Nonlinearity is a problem because it means that there are many possible subsurface models that can satisfy the same seismic dataset. I inverted over three bands of frequencies in increasing order (12-14 Hz, 15-20 Hz, and 21-26 Hz) and over multiple offsets. I also limited the far offsets at the beginning stages of inversion. Another help to mitigate nonlinearity was the use of the SSP to incorporate a multi-scale approach in the model space. The SSP weights low-wavenumbers highly to produce sufficient background updates.

The seismic line was acquired over a crooked line, which can be a difficult problem to handle. A crooked line has coordinates in 3D, but extends only to a limited extent in the crossline (out-of-plane) direction. The original 3D coordinates were kept for traveltimes tomography, but due to the excessive computational costs of 3D FWI, I used 2D FWI. To go from a 3D traveltimes tomography model to 2D for FWI, I projected the crooked line coordinates onto a straight line, which created some errors in traveltimes. To mitigate the errors resulting from the projection, I adopted a strategy similar to [Kamei et al. \(2015\)](#) and discarded data where the projected offset and the original offset percentage difference was greater than 3%. A percentage difference of 3% proved to be optimal in allowing as much data as possible into the inversion without creating very large traveltimes errors. Another option would have been to have completed FWI in 2.5D. The use of a 2.5D method constructs the equivalent 3D source wavefield in the receiver plane, and accounts for a crooked line geometry that is not possible in 2D. [Pratt \(1989\)](#) provided a clever solution in the Fourier domain. He used a Fourier transform in the crossline direction to reduce the 3D wavefield problem to multiple 2D wavefields. However, in the end I chose to remain with 2D FWI, because the final result was robust.

The surface topography was handled by using a true topographic surface during FWI, placing sources and receivers along the topography. The free surface just along the topographic surface was handled by using an air velocity and strong attenuation in the air layer, and mild attenuation in the subsurface ([Roecker et al., 2010](#)). Perfectly matched layers (PMLs) were used on all edges of the model, to avoid creating unphysical reflections. I limited the inversions to a depth of 0.66 km due to the limited offsets available. This is of course a limitation in that the interpretation of a Utica shale layer at ~ 2.2 km is not possible on such a limited depth. However, a high-quality

near-surface velocity model has the potential to greatly enhance image focusing in subsequent processing at greater depths. As an analogy, consider the corrective power of eyeglasses for those who are nearsighted. Nearsightedness is a condition where close objects are clear, but far objects are not clear. In order to correct for the far objects, the light that is being refracted into the eye at a close distance must first be corrected. When the focal length and refracted patterns of light at a close distance are corrected, the far objects are made more clear (B. Smithyman, personal communication, 2016). In a similar way, if we correct the velocities in the near-surface, the velocities (and image) will become more clear at greater depths. Sound waves must first propagate through the near-surface before they propagate through greater depths.

I was successful in the first goal of creating a high-resolution near-surface velocity model. One of the novelties in completing this study is that the structural geology in the first 0.66 km became more clear. It turns out that there were no visible faulted structures in the survey area, but this fact was only uncovered by using FWI. The second goal of applying the SSP to the gradient of the misfit functional to a field dataset is novel in its own right, as this was the first real dataset on which the application of FWI using the SSP had been applied. Using the SSP on the gradient proved to be critical in updating the background velocity in the absence of data frequencies below 12 Hz.

1.4 Structure of thesis

This thesis consists of four chapters. In Chapter 2, I provide a mathematical background for the methods used. The background I cover includes a discussion on 3D traveltome tomography methods developed by [Zhang and Toksöz \(1998\)](#), a 2D phase-only approach to FWI after [Pratt et al. \(1998\)](#), [Bednar et al. \(2007\)](#) and [Kamei et al. \(2014\)](#), and the SSP applied to the gradient of the misfit functional, after [Zuberi and Pratt \(2016\)](#). Appendix A provides some additional background for the elastic wave equations and the acoustic wave equations.

Chapter 3 presents the application of FWI with the SSP to a crooked seismic line in eastern Ohio. The Firestone survey was acquired in 2013 and is located in eastern Ohio in the Appalachian Basin. There are hundreds of wells that have been drilled in the area, but since 2010 advances in horizontal drilling have made hydraulic fracturing for the Utica shale economic and high priority. Appendix B provides additional tabulated data that were used to construct geologic cross-sections. A high-resolution velocity model was recovered to a depth of 0.66 km, using a combination of 3D traveltome tomography followed by 2D FWI with SSP. By combining the information from the velocity models with the information from nearby wells, I was able to identify the trends of two geologic layers, the Big Injun sand, and the Berea sandstone. The last section in Chapter 3 is the time processing completed by Arcis Seismic Solutions (a seismic contractor) as well as my own time and depth processing. I was able to produce comparable results in my time processing as compared

CHAPTER 1. INTRODUCTION

to Arcis. Also, using the FWI results may have improved the depth reflection processing results by pushing reflectors deeper toward the desired position, based on nearby well information. However, without well ties, the reflection processing results are only preliminary. Chapter 4 presents the novelty of my work, conclusions, limitations, and recommendations for future work.

Chapter 2

Background Theory

Chapter 1 contained an introduction to the common midpoint (CMP) reflection method, the challenges with the nonlinear FWI problem, the challenges associated with processing land vibroseis data, and my thesis objectives. In this chapter, I provide a mathematical context by reviewing the relevant theory for 3D first-break traveltome tomography, 2D wave equation forward modelling, and phase-only full-waveform inversion (FWI)¹ with the scaled-Sobolev preconditioner (SSP). I provide some theory on the traveltome tomography implementation based on work by [Zhang and Toksöz \(1998\)](#). The FWI theory I provide is largely based on work by [Pratt et al. \(1998\)](#) and [Kamei et al. \(2014\)](#). The SSP theory is based on [Zuberi and Pratt \(2017\)](#) and [Zuberi and Pratt \(2016\)](#).

2.1 3D traveltome tomography

In order to successfully recover a starting velocity model for FWI, I used an implementation of 3D first-break traveltome tomography developed by [Zhang and Toksöz \(1998\)](#) with a software package called *TomoPlus* by GeoTomo. Zhang and Toksöz developed an iterative shortest path ray-tracing (SPR) method of traveltome tomography. The goal of traveltome tomography in my case was to produce a starting velocity model as an input for FWI. Traveltome tomography compares picked first-break picks to synthetic picks to converge on a velocity model. In forward modelling, Zhang and Toksöz used a finite difference scheme to simulate the eikonal equation. Instead of using absolute traveltome data in their inversion scheme, they used scaled versions of the data, called ‘average slowness’ and ‘apparent slowness’. In order to find a solution to this traveltome tomography problem, the objective function must be defined and minimized.

¹The word ‘full’ in *full-waveform inversion* may be considered a misnomer in that some parts of the waveforms are not inverted due to physical assumptions made in wave propagation. However, due to its practically universal adoption, I continue by using ‘full-waveform inversion’ or ‘FWI’ for short.

2.1.1 ‘Objective function’ vs. ‘misfit functional’

There are two terms sometimes used interchangeably that can be confusing: the ‘objective function’ and the ‘misfit functional’. When I refer to the objective function, I mean a function with both data misfit terms and a regularization term. When I refer to a misfit functional, I mean a function with only data misfit term(s), and *no* regularization term. The traveltime tomography implementation I use includes a regularization term and so it is referred to as an objective function; however, the full-waveform inversion (FWI) implementation I use does *not* include a regularization term and so it is referred to as a misfit functional.

2.1.2 Objective function

The objective function contains three distinct terms: the misfit of the average slowness data, the misfit of the apparent slowness data, and the model roughness (or regularization) term. The model roughness is applied using Tikhonov regularization (Tikhonov and Arsenin, 1977). Following Zhang and Toksöz (1998), the objective function can be written as

$$\Phi(\mathbf{m}) = (1 - w)\|C_\ell(\mathbf{s} - \mathbf{L}(\mathbf{m}))\|^2 + w\|D_x(\mathbf{s} - \mathbf{L}(\mathbf{m}))\|^2 + b\|\mathbf{Rm}\|^2, \quad (2.1)$$

or more compactly as

$$\Phi(\mathbf{m}) = (1 - w)\|\bar{\mathbf{s}} - \bar{\mathbf{L}}(\mathbf{m})\|^2 + w\|\hat{\mathbf{s}} - \hat{\mathbf{L}}(\mathbf{m})\|^2 + b\|\mathbf{Rm}\|^2,$$

where

$$\bar{\mathbf{s}} := \frac{\mathbf{s}}{\ell} \quad (2.2)$$

is the average slowness data (i.e., the traveltimes divided by the ray lengths), and

$$\hat{\mathbf{s}} := \frac{\partial \mathbf{s}}{\partial x} \quad (2.3)$$

is the apparent slowness data (traveltime derivatives with respect to spatial distance). The absolute traveltime data can be written as a vector \mathbf{s} with N_d receiver locations,

$$\mathbf{s} = \begin{bmatrix} s_1 \\ s_2 \\ \vdots \\ s_{N_d} \end{bmatrix}; \quad (2.4)$$

the predicted traveltimes can be written as a vector $\mathbf{L}(\mathbf{m})$ with N_d receiver locations for the current model \mathbf{m} ,

$$\mathbf{L}(\mathbf{m}) = \begin{bmatrix} L_1(\mathbf{m}) \\ L_2(\mathbf{m}) \\ \vdots \\ L_{N_d}(\mathbf{m}) \end{bmatrix}; \quad (2.5)$$

and the current set of N_m velocity model parameters can be written as a vector \mathbf{m} , where

$$\mathbf{m} = \begin{bmatrix} m_1 \\ m_2 \\ \vdots \\ m_{N_m} \end{bmatrix}. \quad (2.6)$$

D_x is a differential operator for traveltimes with respect to distance x , w is a weighting factor and b is a smoothing trade-off term. C_ℓ is a scaling operator to a traveltimes with corresponding ray length ℓ , returning the average slowness \bar{s} . The ray length $\ell(\mathbf{m})$ is dependent on each model parameter and it is updated during tomography at each iteration. The parameter $\bar{\mathbf{L}}(\mathbf{m})$ is the predicted average slowness data, and $\hat{\mathbf{L}}(\mathbf{m})$ is the predicted apparent slowness data. The parameter \mathbf{R} affects the roughness of the model: it is a spatial derivative operator matrix of dimensions $N_l \times N_l$, where N_l is the number of nodes in a finite difference model. I assume that the number of model parameters is equal to the number of nodes, i.e., $N_m = N_l$. A first-order derivative operator \mathbf{R} can be written as

$$\mathbf{R} = \frac{1}{\Delta x} \begin{bmatrix} -1 & 1 & & & \\ & -1 & 1 & & \\ & & \ddots & \ddots & \\ & & & -1 & 1 \end{bmatrix}. \quad (2.7)$$

Zhang and Toksöz (1998) ran tests and in their case found the most stable operators to be of second- and third-order.

2.1.3 Inversion algorithm

A Gauss-Newton (GN) approach is used to linearize the objective function in equation 2.1, followed by a conjugate gradient (CG) technique to solve the inversion at each iteration (Scales, 1987; Zhang and Toksöz, 1998). This approach leads to the equation,

$$((1 - w)\mathbf{A}_k^t \mathbf{A}_k + w\mathbf{B}_k^t \mathbf{B}_k + b\mathbf{R}^t \mathbf{R} + \chi_k \mathbf{I}) \Delta \mathbf{m}_k = (1 - w)\mathbf{A}_k^t (\bar{\mathbf{s}} - \bar{\mathbf{L}}(\mathbf{m}_k)) + w\mathbf{B}_k^t (\hat{\mathbf{s}} - \hat{\mathbf{L}}(\mathbf{m}_k)) - b\mathbf{R}^t \mathbf{R} \mathbf{m}_k, \quad (2.8)$$

where

$$\mathbf{A} := \frac{\partial \bar{\mathbf{L}}}{\partial m_j} = \frac{1}{\ell} \cdot \frac{\partial \mathbf{L}}{\partial m_j}, \quad j = 1, 2, 3, \dots, N_M, \quad (2.9)$$

$$\mathbf{A} = \begin{bmatrix} \frac{\partial \bar{L}_1}{\partial m_1} & \dots & \frac{\partial \bar{L}_1}{\partial m_{N_M}} \\ \vdots & \ddots & \vdots \\ \frac{\partial \bar{L}_{N_d}}{\partial m_1} & \dots & \frac{\partial \bar{L}_{N_d}}{\partial m_{N_M}} \end{bmatrix}, \quad (2.10)$$

$$\mathbf{B} := \frac{\partial \hat{\mathbf{L}}}{\partial m_j} = \frac{\partial^2 \mathbf{L}}{\partial m_j \partial x}, \quad (2.11)$$

$$\mathbf{B} = \begin{bmatrix} \frac{\partial \hat{L}_1}{\partial m_1} & \dots & \frac{\partial \hat{L}_1}{\partial m_{N_M}} \\ \vdots & \ddots & \vdots \\ \frac{\partial \hat{L}_{N_d}}{\partial m_1} & \dots & \frac{\partial \hat{L}_{N_d}}{\partial m_{N_M}} \end{bmatrix}, \quad (2.12)$$

and

$$\mathbf{m}_{k+1} = \mathbf{m}_k + \Delta \mathbf{m}_k, \quad k = 1, 2, 3, \dots, N. \quad (2.13)$$

The subscript j is the number of model parameters and the subscript k is the iteration number. The parameter $\Delta \mathbf{m}$ is the velocity model update. The superscript t denotes the matrix transpose. The parameter \mathbf{A} is the average-slowness sensitivity matrix. Each of the non-zero terms in \mathbf{A} is the local ray length across a cell, divided by the entire ray length. \mathbf{B} is the apparent-slowness sensitivity matrix. The non-zero terms in \mathbf{B} are the ray length differences across a cell, divided by the receiver spacing. The derivatives in \mathbf{B} are calculated using the locations of two adjacent receivers. From equation 2.8, we solve for $\Delta \mathbf{m}_k$ at each iteration k by using the GN and CG techniques previously mentioned. One advantage of using these techniques is that neither require storing the sensitivity matrices, but rather the results of the multiplication of a matrix by a vector are required.

The $\chi_k \mathbf{I}$ is a damping term that helps guide the convergence of the objective function (with \mathbf{I}

as the identity matrix with dimensions $N_m \times N_m$). Specifically, $\chi_k = \eta \times rhs$, where $\eta \approx 0.1$ is an empirical parameter, and rhs is the RMS misfit norm of the right-hand side of equation 2.8. If the objective function does not minimize well, a strong (large χ) damping is applied, and no significant model updates occur. If the objective function minimizes well, a smaller damping is applied, and convergence rates increase (Zhang and Toksöz, 1998).

Additional information on wavefront ray-tracing methods can be found in (1) Hole and Zelt (1995) on solving for 3D seismic reflection traveltimes using finite-differences, (2) Vinje et al. (1993) on applying wavefront construction to ray tracing, and (3) Moser (1991) on using graph theory to find the shortest traveltime path. The result of first-break traveltime tomography provides a suitable starting model to help satisfy the half-cycle criterion of full-waveform inversion (FWI). The benefit of traveltime tomography is that it can produce low-wavenumber updates, provided there is significant ray coverage. Though traveltime tomography can suffer from local minima in the objective function, it has been used to provide suitable starting models for FWI (eg., Smithyman and Clowes, 2013; Kamei et al., 2015).

2.2 Full-waveform inversion (FWI)

2.2.1 Forward modelling

For the FWI forward problem, I work in the Laplace-Fourier (LF) domain. Some of the advantages over the time domain include being able to solve the wave equation for multiple sources at a minimal cost, using accurate attenuation modelling, focusing on early-arriving transmitted (low-wavenumber) events, and being able to use a frequency-selection strategy (Pratt and Worthington, 1990; Umpleby et al., 2010). Following Shin and Cha (2009), and Kamei and Pratt (2013), the Laplace-Fourier transform of the time-domain seismic wavefield can be written as

$$u(x, z; \omega, \tau) = \int_0^{\infty} u(t) e^{-(t/\tau)} e^{-i\omega t} dt, \quad (2.14)$$

where x and z are the two spatial variables in 2D, $u(t)$ is a time-domain wavefield, τ is a real-valued decay constant, ω is real-valued angular frequency ($= 2\pi f$, where f is frequency), and i is $\sqrt{-1}$. The $e^{-(t/\tau)}$ term is used to implement damping of later arrivals in the wavefield. Smaller values of τ places more weight on early seismic arrivals, and less weight on later arrivals (Sirgue, 2003; Brenders and Pratt, 2007). This is particularly useful in that the transmitted (refracted) arrivals arrive early and contain low-wavenumber information. Using time-damping thus helps mitigate the ill-posed FWI problem by focusing on (low-wavenumber) background updates and reaching the global minimum solution more quickly (Kamei et al., 2013). Equation 2.14 can be written

more compactly as

$$u(x, z; \Omega) = \int_0^{\infty} u(t)e^{-\Omega t} dt, \quad (2.15)$$

where $\Omega = i\omega + (1/\tau)$ is the complex-valued angular frequency.

In the methods used in this thesis, wave propagation is assumed to be isotropic, acoustic, and 2D. The assumption of isotropic wave propagation means that we assume the wave to have the same properties in all directions. This is an unphysical limitation especially in the presence of strong anisotropy, as waves propagate faster in one direction over another depending on the orientation of the rocks (see Appendix A). The acoustic assumption discards elastic effects including S-waves and PS converted waves. This also can be unrealistic, as S-waves and mode conversions do sometimes play a strong role in subsurface wave propagation. The 2D assumption discards all out-of-plane effects. Although there have been recent developments in the computation an inversion of anisotropic (eg., [Hadden and Pratt, 2017](#)), visco-elastic (eg., [Brossier, 2011](#)), and 3D (eg., [Butzer et al., 2013](#)) wavefields, the computational costs involved are significant. Beyond that, a robust parameterization for anisotropy and elastic constants remains an unresolved (yet highly debated) challenge ([Virieux and Operto, 2009](#)).

The 2D isotropic visco-acoustic wave equation can be written as

$$\nabla \left(\frac{1}{\rho(x, z)} \nabla u(x, z; \Omega) \right) + \frac{\Omega^2}{c^2(x, z; \omega) \rho(x, z)} u(x, z; \Omega) = -f(x, z; \Omega), \quad (2.16)$$

where $\rho(x, z)$ is density, $c(x, z; \omega)$ is the complex-valued velocity, $u(x, z; \Omega)$ is the wavefield defined by equation 2.14, and $f(x, z; \Omega)$ is the source term. Appendix A gives more mathematical background on this wave equation and the physical assumptions made by not including elastic and anisotropy parameters. By allowing the velocity c to be complex, the effects of wave attenuation can be implemented, such that (dropping the x and z dependencies)

$$c(\omega) = c_R(\omega) + ic_I(\omega), \quad (2.17)$$

where $c_R(\omega)$ is the real component of the (frequency-dependent) velocity, and

$$c_I(\omega) = -\frac{2c_R(\omega)}{Q} \quad (2.18)$$

is the imaginary component of the velocity. Q is a dimensionless parameter referred to as the ‘Quality’ factor, where $1/Q$ quantifies the attenuation of seismic waves. In this thesis, Q is considered

to be independent of frequency. Given the limited bandwidth of the data, a frequency-independent Q is a reasonable assumption.

The forward problem is solved using finite differences on a regular grid (Jo et al., 1996; Brenders and Pratt, 2007). To locate sources and receivers arbitrarily (possibly in between grid positions), Kaiser windowed sinc functions are used, after Hicks (2002). Perfectly matched layers (PMLs) are used at all edges of the model (Berenger, 1994). A succinct matrix formalism is provided in Pratt et al. (1998) for the discretized forward problem. Using their notation, equation 2.16 can be discretely approximated in the Laplace-Fourier domain as

$$\mathbf{S}(\mathbf{m}; \Omega)\mathbf{u}(\Omega) = \mathbf{f}(\Omega) \implies \mathbf{u}(\Omega) = \mathbf{S}^{-1}(\mathbf{m}; \Omega)\mathbf{f}(\Omega), \quad (2.19)$$

where \mathbf{S} is an impedance matrix that approximates the physics of the wave equation with dimensions $N_l \times N_l$ (N_l is the number of nodes in finite difference model), \mathbf{u} is the complex-valued, discretized vector wavefield at N_l grid points, \mathbf{f} is a vector of source terms at N_l grid points, and \mathbf{m} is a set of N_m model parameters. The wavefield and the source terms represent Laplace-Fourier components at each grid point of the pressure and source wavefields for a particular choice of frequency ω and damping parameter τ . The use of the inverse impedance matrix \mathbf{S}^{-1} is symbolic, as we do not actually invert the matrix \mathbf{S} : it represents the solution of (approximated) partial differential equations of the wavefield, and also implicitly includes the boundary conditions. Equation 2.19 is solved for \mathbf{u} by applying nested dissection (George and Lui, 1981) followed by a lower-triangular upper-triangular (LU) decomposition of \mathbf{S} .

2.2.2 Misfit functional

As in many inverse problems, the goal in FWI is to minimize the misfit between the observed data and calculated data. The misfit functional using an L_2 norm can be written as the real-valued sum of squared residuals,

$$E = \frac{1}{2} \delta \mathbf{d}^t \delta \mathbf{d}^*. \quad (2.20)$$

The residual error, $\delta \mathbf{d}$, is a vector defined at N_d receiver locations. The superscript t designates the transpose, and superscript $*$ designates the complex conjugate.

The misfit functional is often constructed to include both amplitude and phase information. However, as Kamei et al. (2014) note, amplitude components are more vulnerable than phase components to source-receiver coupling errors. Also, the observed amplitudes in a 3D visco-elastic subsurface can vary a great deal from those modelled with a 2D visco-acoustic wave equation. In

this thesis, I use only the phase of the data and use the ‘logarithmic phase-only residual’ (equation 18 in [Kamei et al., 2014](#)). It can be written as

$$\delta d_i = \Im \left[\ln \left(\frac{u_i}{d_i} \right) \right] = \theta_{u_i} - \theta_{d_i}, \quad (2.21)$$

where \Im is imaginary, u_i is the calculated seismic wavefield at receiver i , and d_i is the observed seismic wavefield at receiver i . The corresponding parameters θ_{u_i} and θ_{d_i} are the phase of the calculated wavefield and the phase of the observed seismic wavefield, respectively.

2.2.3 Gradient

I assume now that the only unknowns in the model are the velocities and can be represented by N_m model parameters. Also, these velocities are assumed to be defined at N_l grid points, or $N_m = N_l$. The density parameters ρ from equation 2.16 are recovered by Gardner’s relation from the velocities ([Gardner et al., 1974](#)).

To reduce the misfit functional, *fullwv* uses a local conjugate gradient method (see [Mora, 1987](#)) to update a set of N_m velocity model parameters \mathbf{m} , according to

$$\mathbf{m}_{k+1} = \mathbf{m}_k - \alpha_k \boldsymbol{\gamma}_k, \quad (2.22)$$

where k is an arbitrary iteration number, α is the step length in the opposite direction of the gradient, and $\boldsymbol{\gamma}$ is the preconditioned conjugate gradient vector of the misfit functional E for the model \mathbf{m} . The conjugate gradient is constructed by a linear combination of current and past model gradients ([Polak and Ribière, 1969](#)).

The gradient of the misfit functional, $\nabla_{\mathbf{m}} E$, is calculated using the ‘adjoint-state’ method, which avoids the direct computation of Frechét derivatives, an idea originally introduced by [Chavent \(1974\)](#). A modern review of the adjoint-state method can be found in [Plessix \(2006\)](#). Assuming symmetry of \mathbf{S} , and following the concise notation of [Pratt \(1999\)](#) and [Bednar et al. \(2007\)](#), the adjoint-state gradient of the *phase-only* misfit vector (dimensions $N_m \times 1$) can be written as

$$\nabla_{\mathbf{m}} E = \Im \left[\mathbf{F}' \mathbf{S}^{-1} \mathbf{w}^* \right], \quad (2.23)$$

where \mathbf{F} is an $N_l \times N_l$ matrix of virtual source terms, superscript t is the transpose, and superscript $*$ is the complex conjugate. The q -th column of \mathbf{F} is an $N_l \times 1$ vector and can be written as

$$\mathbf{F}_q = -\frac{\partial \mathbf{S}}{\partial m_q} \mathbf{u}. \quad (2.24)$$

The parameter \mathbf{w} is the weighted residual vector. For the logarithmic phase-only misfit functional, the weighted residual at receiver i can be written as

$$w_i = \frac{1}{u_i} \delta d_i. \quad (2.25)$$

In order to make use of \mathbf{w} in the calculation of the gradient from equation 2.23, the associated matrix and vector dimensions must be all be multipliable. We augment the \mathbf{w} vector with $(N_l - N_d)$ 0's, so that its new length is N_l ,

$$\mathbf{w} = \begin{bmatrix} w_1 \\ w_2 \\ \vdots \\ w_{N_d} \\ 0 \\ \vdots \\ 0_{N_l} \end{bmatrix}. \quad (2.26)$$

Equation 2.23 can then be restated in terms of dimensions,

$$\nabla_{\mathbf{m}} E = \mathfrak{J} [\mathbf{F}' \mathbf{S}^{-1} \mathbf{w}^*], \quad (2.27)$$

$$[N_m \times 1] = \mathfrak{J} [[N_l \times N_l]' [N_l \times N_l]^{-1} [N_l \times 1]^*]. \quad (2.28)$$

The end result is that both sides have agreeing matrix dimensions of $N_m \times 1$, keeping in mind the assumption of $N_m = N_l$. The partial derivative term $\partial/\partial m_q$ in equation 2.24 is the operator that represents perturbations in the model \mathbf{m} (Pratt et al., 1998).

The ‘virtual source method’ is a clever (and fast) way to generate what is called the Frechét partial derivatives matrix (Pratt, 1999). The Frechét matrix is normally defined as

$$\mathbf{J} = \frac{\partial \mathbf{u}}{\partial m_j}, \quad j = 1, 2, \dots, N_m, \quad (2.29)$$

where m_j is the j -th model parameter. Solving the Jacobian defined in equation 2.29 would mean for every perturbation of model parameter solving a forward problem \mathbf{u} . The virtual source method is fast because the Frechét matrix does not have to be calculated explicitly. It is useful to note that the computation of the Frechét matrix depends on how the wave equation is discretized (Pratt, 1999).

Substituting equation 2.24 into equation 2.23, the q -th component of the gradient vector becomes

$$\nabla_{m_q} E = \mathfrak{J} \left[\mathbf{u} \left(\frac{\partial \mathbf{S}}{\partial m_q} \right)^t \mathbf{v} \right], \quad (2.30)$$

where

$$\mathbf{v} = \mathbf{S}^{-1} \mathbf{w}^* \quad (2.31)$$

is the back-propagated residual wavefield. Figure 2.1 provides a visual representation action of a single source-receiver pair in the gradient (equation 2.30). The gradient contains a weighted linear combination of multiplications of the forward propagated wavefield and the backpropagated residual wavefield.

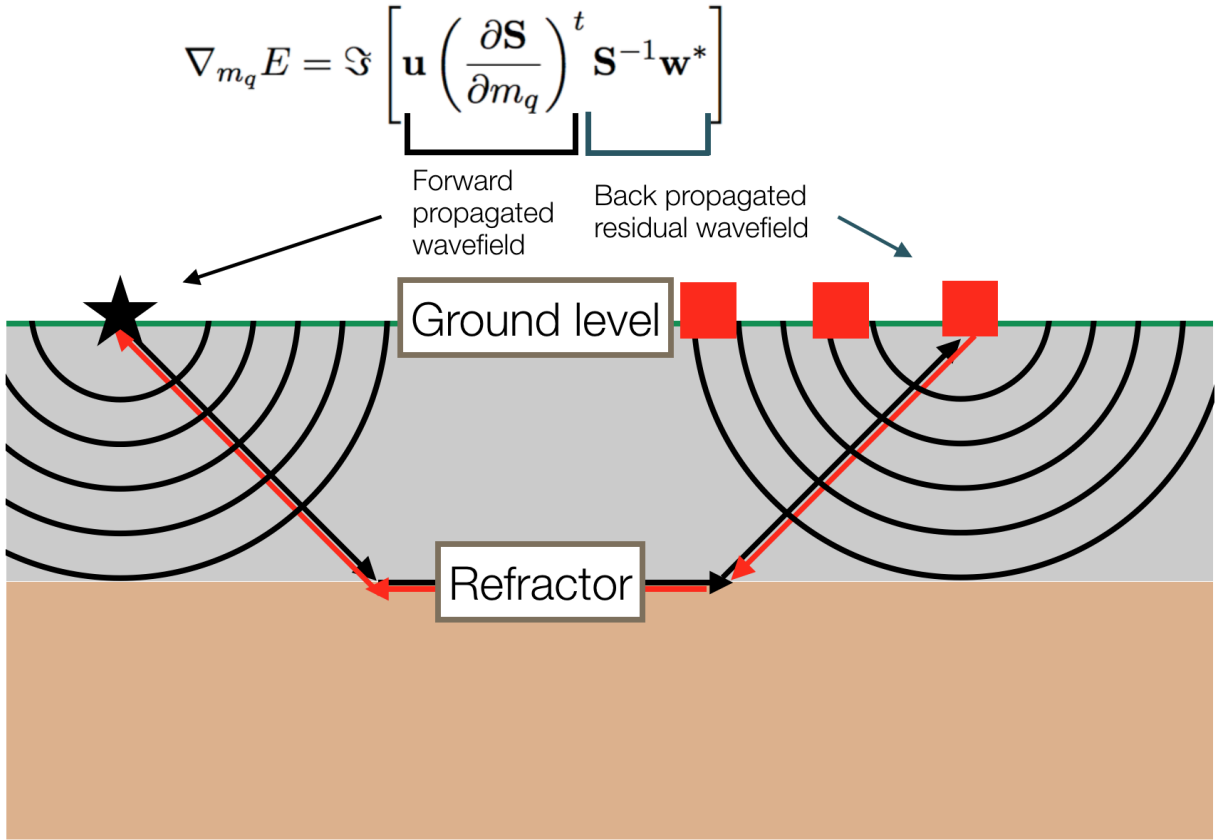


Figure 2.1: Visual representation of the computation of the gradient of the misfit functional, requiring that the forward-propagated wavefield be multiplied with the back-propagated residual wavefield. The source is represented by a star, and receivers are represented by squares.

Finally, the step length α in equation 2.22 can be calculated by using a Brent line search (Brent, 1973). For each iteration, an average of 8 forward solutions were required in order to update the velocity model \mathbf{m} . The Brent line search took on average around six forward modelling steps to arrive at the appropriate step length α , one for the forward-modelled wavefield \mathbf{F}' , and one for the back-propagated residual wavefield \mathbf{v} . One of the advantages of using a Brent line search is that it guarantees the misfit functional will decrease at every FWI iteration, whereas a simple linear estimate may for some iterations increase the misfit functional.

2.2.4 Scaled-Sobolev preconditioner (SSP)

One challenge of FWI, especially with limited frequency content, is that higher wavenumber features tend to dominate the inversion before the background has been updated. One solution is to employ wavenumber filtering to regularize (Brenders and Pratt, 2007), but this solution is challenging to implement, because the user(s) must decide which wavenumbers to filter out. Equation 2.22

included γ , which was defined as the *preconditioned* conjugate gradient. The preconditioner I applied to the gradient is called the ‘scaled-Sobolev preconditioner’ (SSP), developed by Zuberi and Pratt (2017, 2016). The preconditioner is applied by multiplication with the gradient (cf. equation 2.30), expressed as

$$\gamma = \left(\mu_0^2 - \mu_x^2 \left[\frac{\partial^2}{\partial x^2} \right] - \mu_z^2 \left[\frac{\partial^2}{\partial z^2} \right] \right)^{-1} (\nabla_{m_q} E), \quad (2.32)$$

where μ_0 , μ_x , and μ_z are the SSP scale-factors. In the wavenumber domain,

$$FT(\gamma) = \left(\mu_0^2 + \mu_x^2 [k_x^2] + \mu_z^2 [k_z^2] \right)^{-1} (\nabla_{m_q} E), \quad (2.33)$$

where FT is the Fourier transform, subscript m_q is the q -th model parameter, k_x is the x -wavenumber and k_z is the z -wavenumber. Equation 2.33 has an inverse exponent outside of all of the terms, which means that low wavenumbers can be weighted more highly than high wavenumbers. To summarize, the SSP applies a constrained smoothing to the gradient in which high wavenumbers are progressively enhanced. The strength of the high wavenumbers following the smoothing may be controlled by picking appropriate SSP scale factors. These scale factors in practice work as weighting parameters. The larger the scale factor, the smoother the update. But it is important to point out that even with a very large (smooth) scale factor, high wavenumbers are not completely absent from the SSP-conditioned gradient. One practical strategy on picking these parameters is to initially set these equal to the length of the model dimensions to create smooth updates, and then to relax the parameters later in the inversion scheme once the background is better resolved.

2.2.5 Source inversion

The source signature used in acquisition of seismic data is usually unknown and must be estimated. Solving the forward problem in equation 2.19 involves knowing a source wavelet. Assuming the subsurface velocity model is correct, Pratt (1999) showed that the source signature can be accounted for by solving for a complex-valued scalar r in

$$\mathbf{Su} = r\mathbf{f}. \quad (2.34)$$

We can use an L_2 norm objective function (as in equation 2.20) to solve for the complex-valued scalar r . The minimum misfit is achieved when

$$r = \frac{\mathbf{u}^t \mathbf{d}^*}{\mathbf{u}^t \mathbf{u}^*}, \quad (2.35)$$

where \mathbf{u} is the forward modelled wavefield vector and \mathbf{d} is the observed wavefield vector. The superscript t designates the transpose, and superscript $*$ designates the complex conjugate. The numerator is the LF domain expression of the cross-correlation of the predicted time data and observed time data, and the denominator is the LF expression of the autocorrelation of predicted time data.

2.3 Computational environment

The most resource-intensive program used in this thesis was the 2D full-waveform inversion code *fullwv*, written in Fortran by Pratt (1989; 1999). All of the heavy inversion work was completed on an Intel(R) Xeon(R) CPU E5-2650 0 @ 2.00GHz Linux machine with 16 CPU cores at the University of Western Ontario. The *fullwv* code is parallelized over frequencies, which saves considerable time in testing. The total number of iterations was 233, and the total CPU time taken for all velocity model updates was 7 days, 21 hours and 37 minutes. On average, each iteration took around 49 minutes. If FWI were not run in parallel, the same tasks would have taken more than one month, ie., parallelization over frequencies made the total run-time almost 5 times as fast as compared to without running in parallel.

Chapter 3

Firestone 2D-3C Case Study

In Chapter 1, I gave an introduction to full-waveform inversion (FWI), including the challenges of applying it to land data, and my aim of uncovering a high-resolution near-surface (0.66 km) velocity model in eastern Ohio. In Chapter 2, I gave a mathematical framework for traveltome tomography and FWI, and I introduced a new gradient preconditioner (developed by [Zuberi and Pratt, 2017](#)), referred to as the ‘scaled-Sobolev preconditioner’ (SSP). This chapter presents the application of FWI with SSP to an Ohio land dataset, including the background geology, a presentation and discussion of the results, and some of the limitations of my study.

3.1 Survey overview

In 2012, the U.S. Geological Survey published an assessment that, for the units of the Utica and Point Pleasant black shale within the Appalachian basin, gave an estimate of total recoverable, unconventional oil and gas resources of 940 million barrels of oil (MMBO), 38.2 trillion cubic feet of gas (TCFG), and 208 million barrels of natural gas liquids (MMBNGL) ([Kirschbaum et al., 2012](#)). Following this assessment, in February of 2013, Tidelands Geophysical Company acquired a crooked land seismic data set in the Carroll County of Ohio, USA. The survey, Firestone 2D-3C, was performed on behalf of TGS-NOPEC Geophysical Company (‘TGS’) to further investigate the Utica shale hydrocarbon play, located within the Appalachian basin that covers approximately 596, 000 km² of the northeastern United States ([Kirschbaum et al., 2012](#)). This specific 2D line was shot as a test line for a big 3D survey in the area. A typical Utica shale well with east central Ohio lithology is shown in Figure 3.1.

The FWI results presented herein only penetrate to 0.66 km, but the Utica shale is found between 2.2 km to 2.5 km in the area (see Appendix B). This presents a problem, because the Utica shale remains unresolved in my final images. However, the purpose of my study was not to resolve the Utica shale layer, but rather to resolve only the near-surface. Why is it useful then? In the

oil and gas industry, FWI is most often being applied in the near-surface of geologically complex environments that have not been resolvable using other approaches. Using FWI in the near-surface often results in the proper focus and placement of deeper reflectors, or other important features. To my knowledge, a detailed FWI study of the potential geologic complexities of the near-surface in eastern Ohio has not been completed until this study. The FWI results indicate that significant small scale faulting is not present within the near-surface. Without this study, the finer structural elements would be left to mystery.

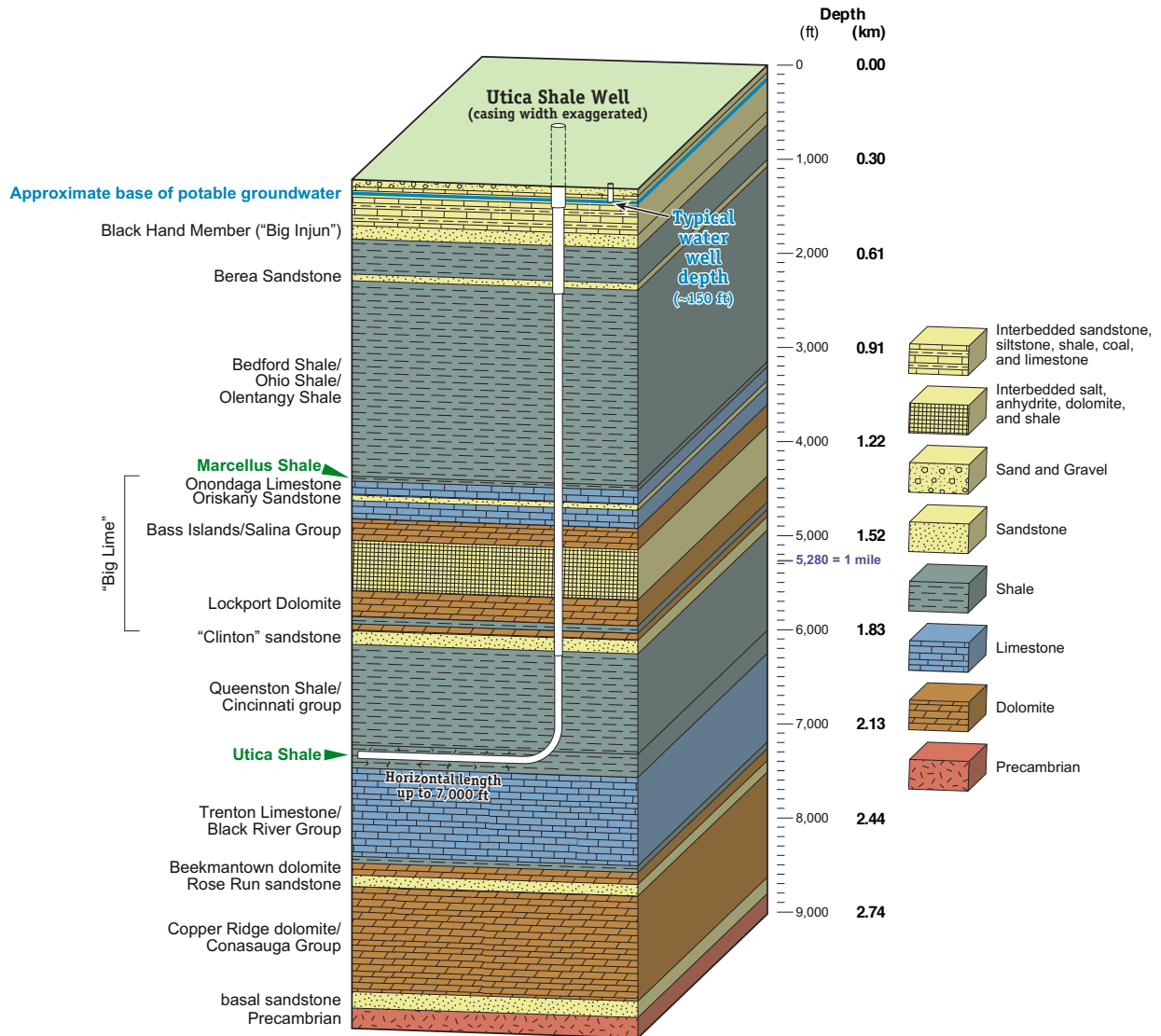


Figure 3.1: Profile of a typical Utica shale well in east central Ohio. Modified from [Ohio Division of Geological Survey \(2011\)](#).

3.1.1 Background geology

Figure 3.2 depicts a geologic map and cross-section of Ohio ([Ohio Division of Geological Survey, 2006](#)). The near surface (< 0.3 km) of the Firestone survey area is part of the Pennsylvanian system. Figure 3.3 depicts the predominant lithology of Ohio and highlights the survey line location. The line runs along an area with thick siltstone beds in the first 0.3 km. Figure 3.4 presents a magnetic anomaly map of Ohio, showing a southwest-northeast trending magnetic anomaly, parallel to the survey. Magnetic surveys typically indicate the variation in magnetic susceptibility of the basement rock, in this case below the survey depth. However, the map is still useful for seeing the larger magnetic trends of the area. The [ODNR Oil and Gas Resources Management \(2016\)](#) has made some well data publicly available, including geographic coordinates and top-of-formation data. Digitized data such as gamma ray and sonic logs are, however, not publicly available in general.

Two top-of-formation cross-sections are presented: the first along the path of the seismic line from south to north (Figure 3.5), and the second perpendicular to the path of the seismic line from west to east (Figure 3.6). Appendix B presents the extended top-of-formation data in tabular form (tables B.1 and B.2), upon which these cross-sections are based. The cross-sections give a general idea of rock composition, layer thickness, and general trends. Given the number of wells and data points in the area, I have confidence in the cross-sections, but I also recognize that the top-of-formation data do sometimes contain mistakes—I am thus careful not to place full certainty in these images. The beds generally dip to the southeast, with Figures 3.5 and 3.6 respectively indicating south and east components of dip. Drill lines (Figure 3.10) follow a pattern generally up and down dip, roughly perpendicular to strike. The reasoning behind the direction of the drill lines has to do with the orientation of stress in the rocks: because hydraulic fractures will naturally open in the direction of least principal stress and propagate perpendicular to these directions, the borehole trajectories are normally chosen to promote this natural fracturing orientation. ([Nolen-Hoeksema, 2015](#)).

A near-surface velocity model can be vital to the proper positioning of deeper reflectors in a seismic image. In this area, the Utica shale can be found at ~ 2.2 km. The required maximum source-receiver offsets that would be required to build an FWI velocity model to the Utica using only refracted waves would be approximately 9 km, but the maximum offsets were only 3.5 km. For the depth of my investigation, 0.66 km, the two most cited top-of-formations were the Big Injun sand, and the Berea sandstone. Both of these formations are consistently identified in Ohio geology literature (eg., [Southworth et al., 1992](#)). The thicknesses of the units (Appendix B) range from 32 m to 76 m for the Big Injun sand, 14 m to 35 m for the Berea sandstone, and 40 to 55 m for the Utica shale.

GEOLOGIC MAP AND CROSS SECTION OF OHIO

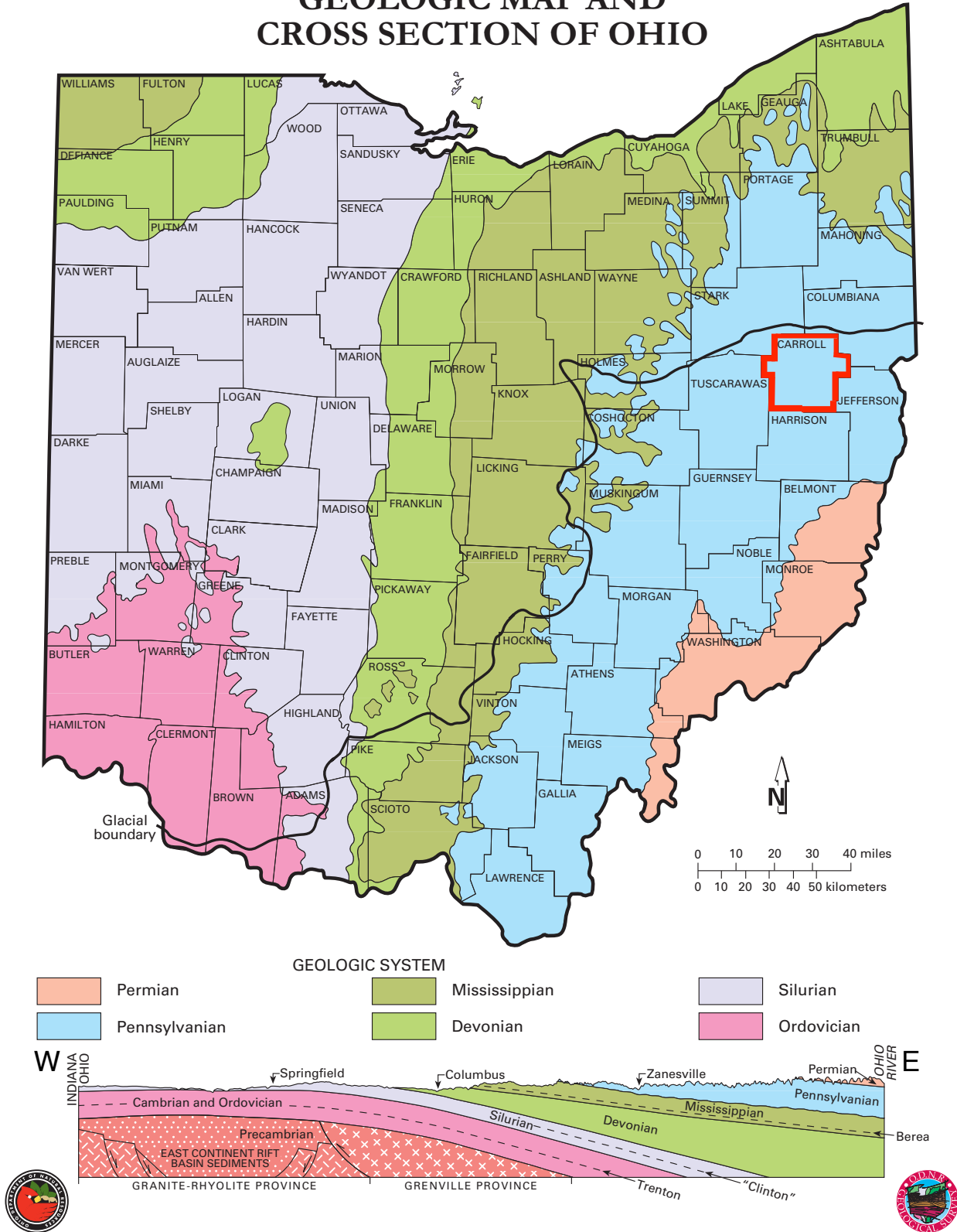


Figure 3.2: Geologic map and cross-section of Ohio. The Firestone survey area is in Carroll County (red outline). The Berea sandstone can be found at a depth of approximately 0.4 km in the Firestone survey area. Map modified from [Ohio Division of Geological Survey \(2006\)](#).

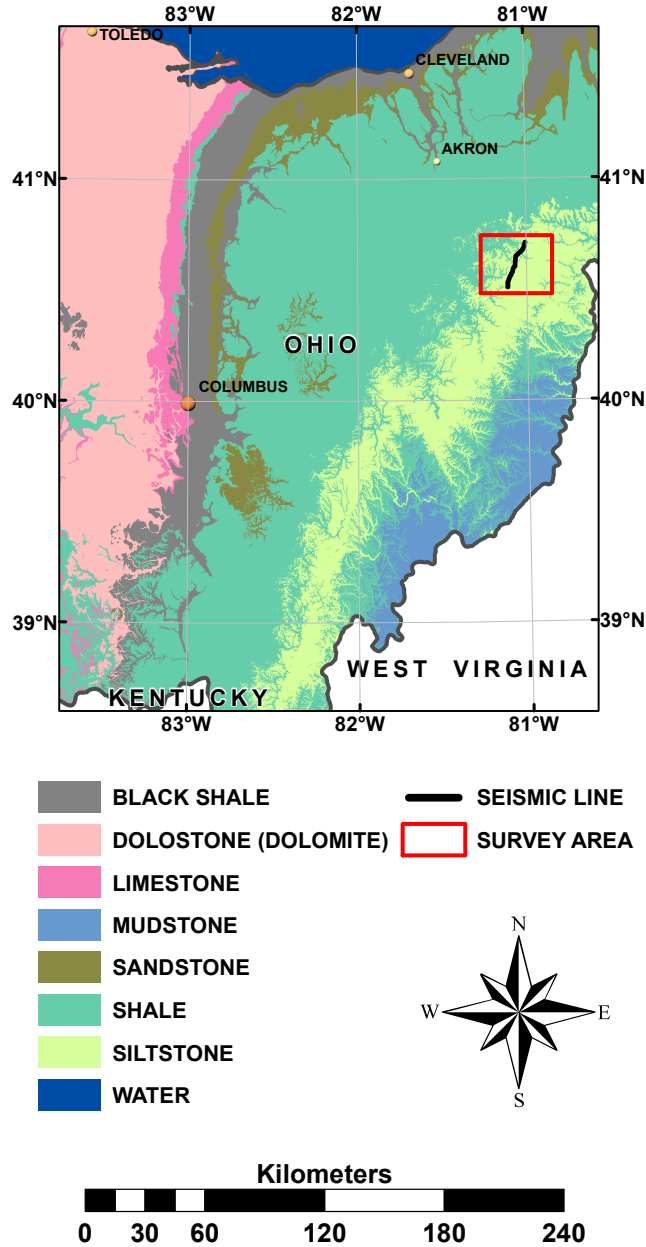


Figure 3.3: Map of predominant near-surface (< 0.3 km) lithology in the state of Ohio, USA. The survey covers an area laden with siltstone, and the seismic line appears to run along geologic strike. Map data from [Nicholson et al. \(2005\)](#).

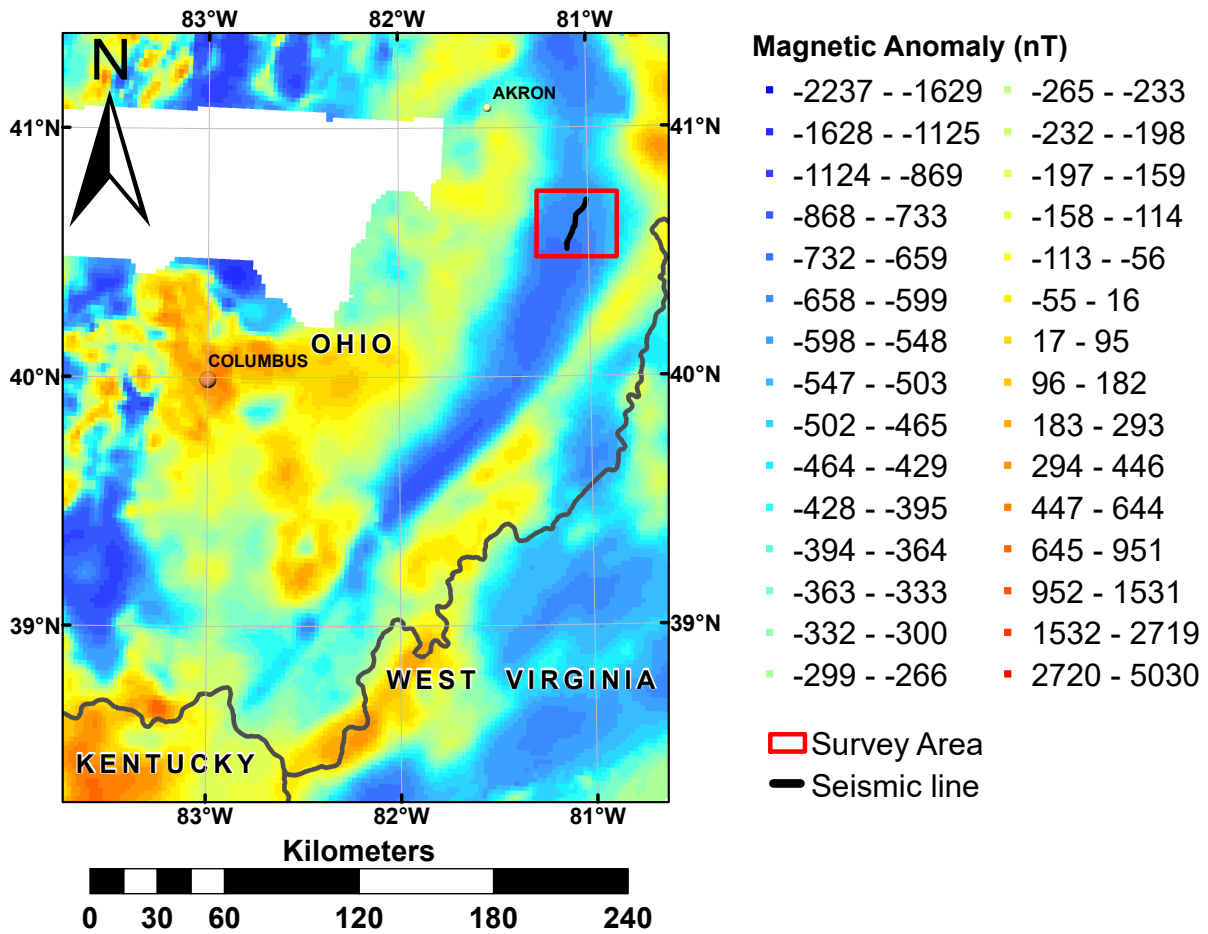


Figure 3.4: Magnetic anomaly map of Ohio, with data taken from [Hildenbrand et al. \(1981\)](#).

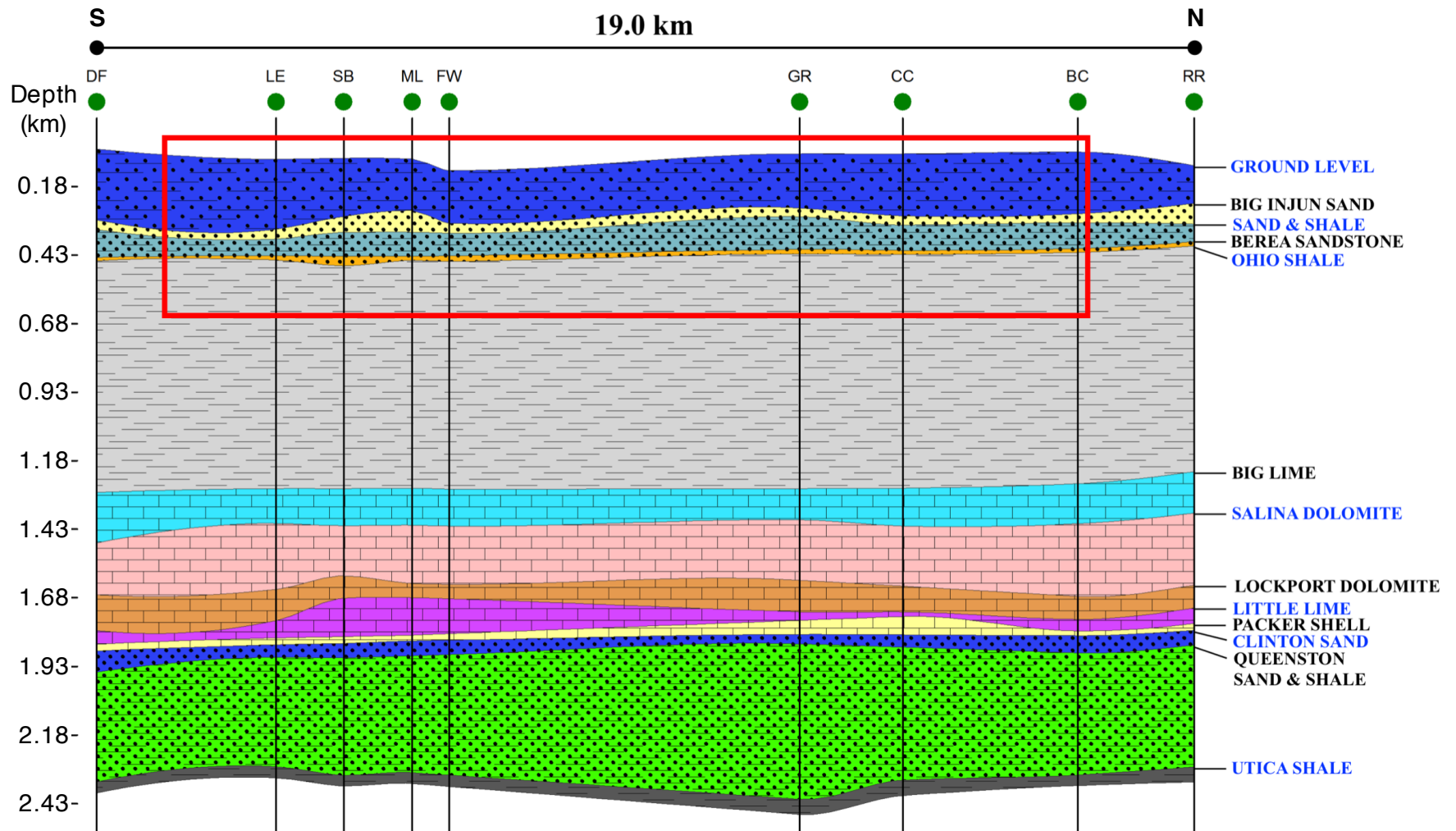


Figure 3.5: Cross-section S-N, along seismic line. The red box indicates the extent of the FWI velocity model. The location of the cross-section is indicated on Figure 3.10. Data courtesy of [ODNR Oil and Gas Resources Management \(2016\)](#).

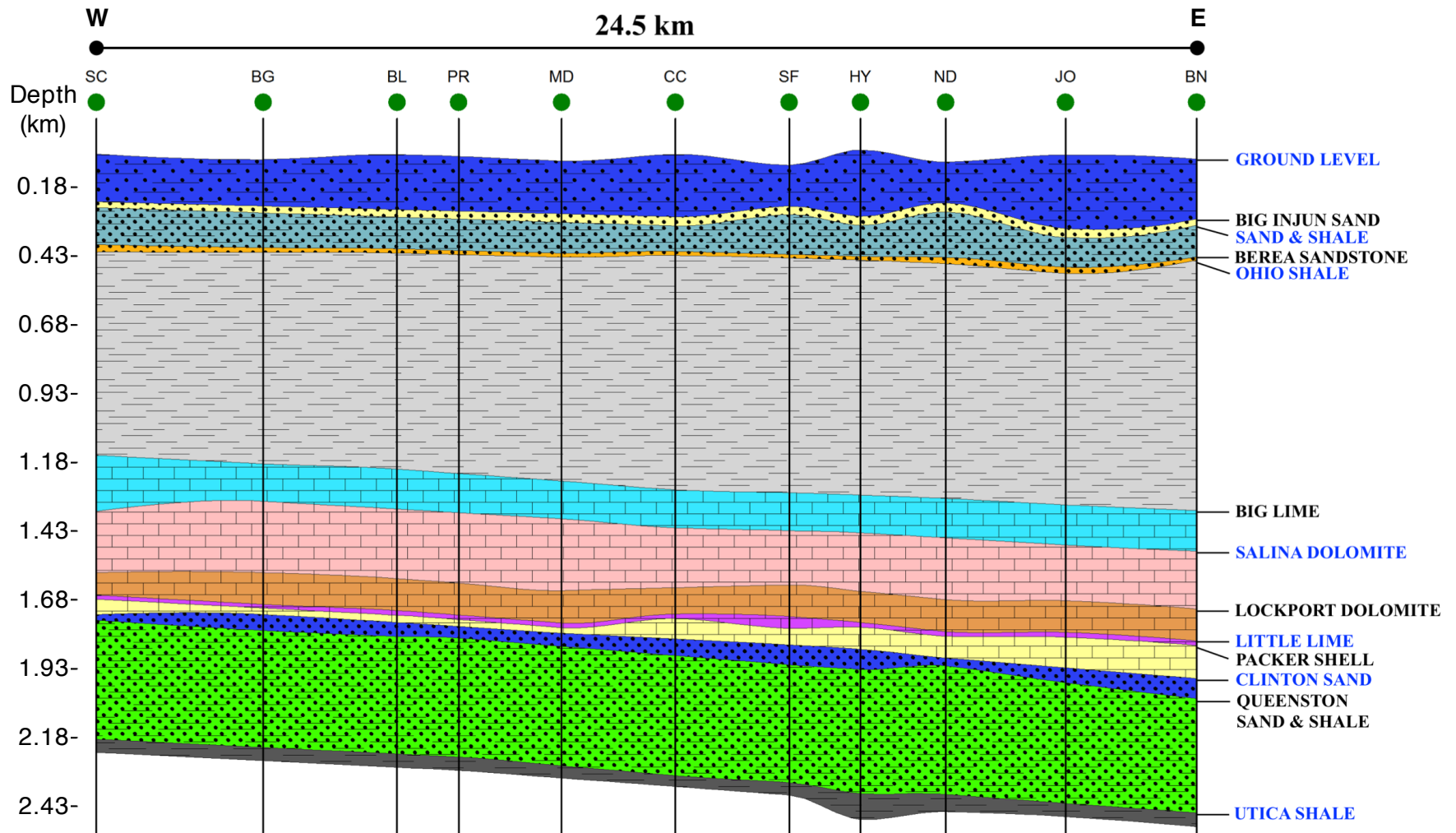


Figure 3.6: Cross-section W-E, perpendicular to seismic line. The location of the cross-section is indicated on Figure 3.10. Data courtesy of ODNR Oil and Gas Resources Management (2016).

3.1.2 Rose Reynolds well and Raymond Goddard well

Two digital well data (.LAS) files were purchased from TGS: the Rose Reynolds (RR) well and the Raymond Goddard (RG) well. The wells were originally recorded in feet below each respective kelly bushing (KB). To be consistent with my derived velocity models and geologic cross-sections, I referenced the tops to a common datum of 426.7 m above sea level. The datum of 426.7 m was selected to be consistent with the processing completed by Arcis Seismic Solutions, the contractor responsible for the original processing of the data. The RR well was drilled on June 6th of 1978 in the Carroll County of Ohio by Schlumberger, just 1.5 km north of the projected seismic line (Figure 3.10). It was chosen because it contained a sonic log for comparison with the FWI results at depths of 0.40 km to 0.66 km, and was available for purchase from TGS. Figure 3.7 shows the data for the RR well to 1.76 km (depth of well). Figure 3.8 is expanded to show the first 0.66 km, the depth extent of the FWI results. The Big Injun sand thickness at this well location is approximately 76 m, and the Berea sandstone thickness is approximately 15 m. Figure 3.9 shows the data from the RG well to a depth of 1.97 km (depth of well). The top-of-formation depths appear to correlate closely with the digital data. For example, the identified shales correlate with high gamma ray values, and the identified sands correlate with low gamma ray values.

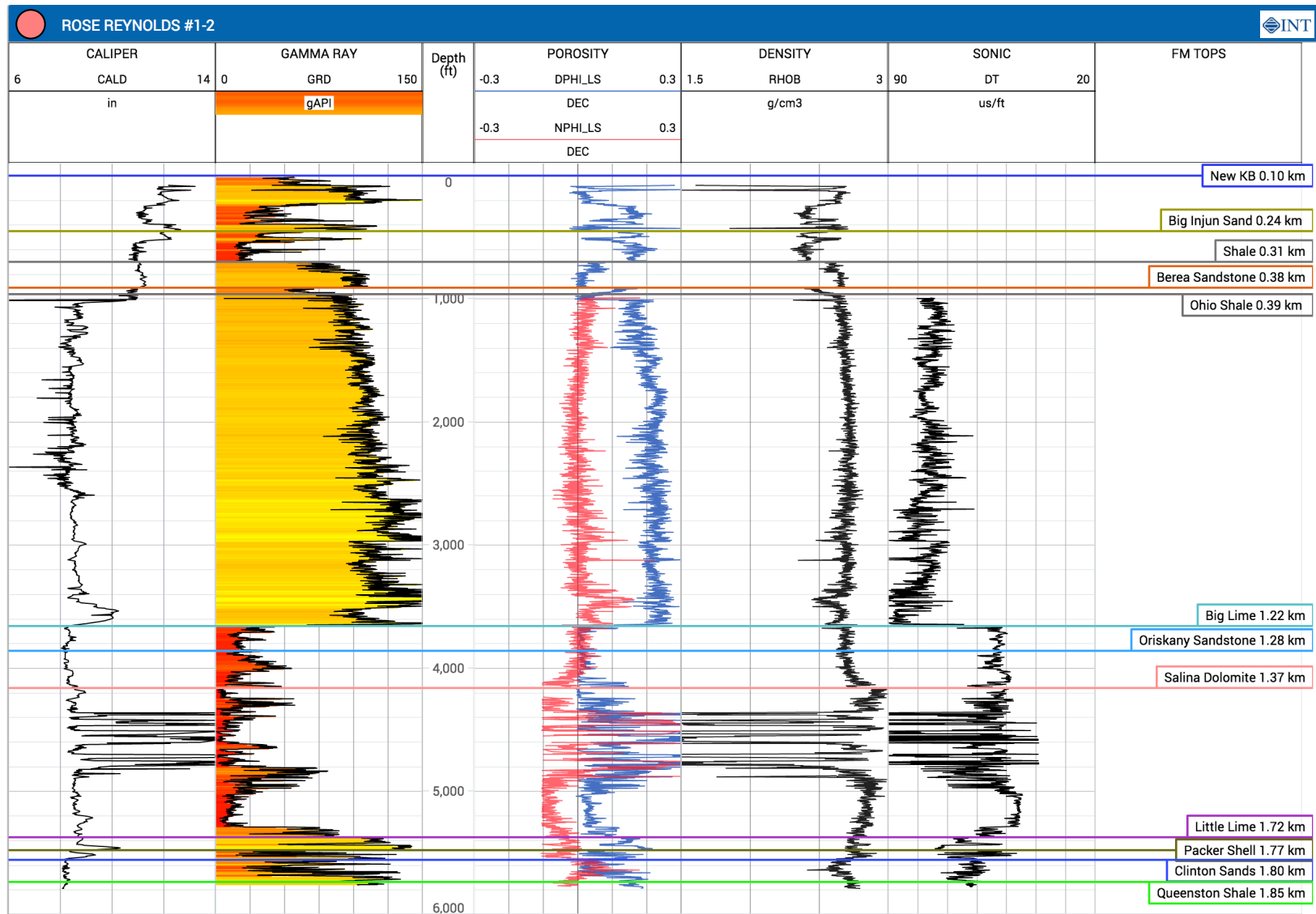


Figure 3.7: Rose Reynolds (RR) digital well data for the entire depth of the log. The right-most column shows top-of-formation depths, based on observed top-of-formation data and referenced to the common datum used in this study. The location of the well is shown on Figure 3.10.

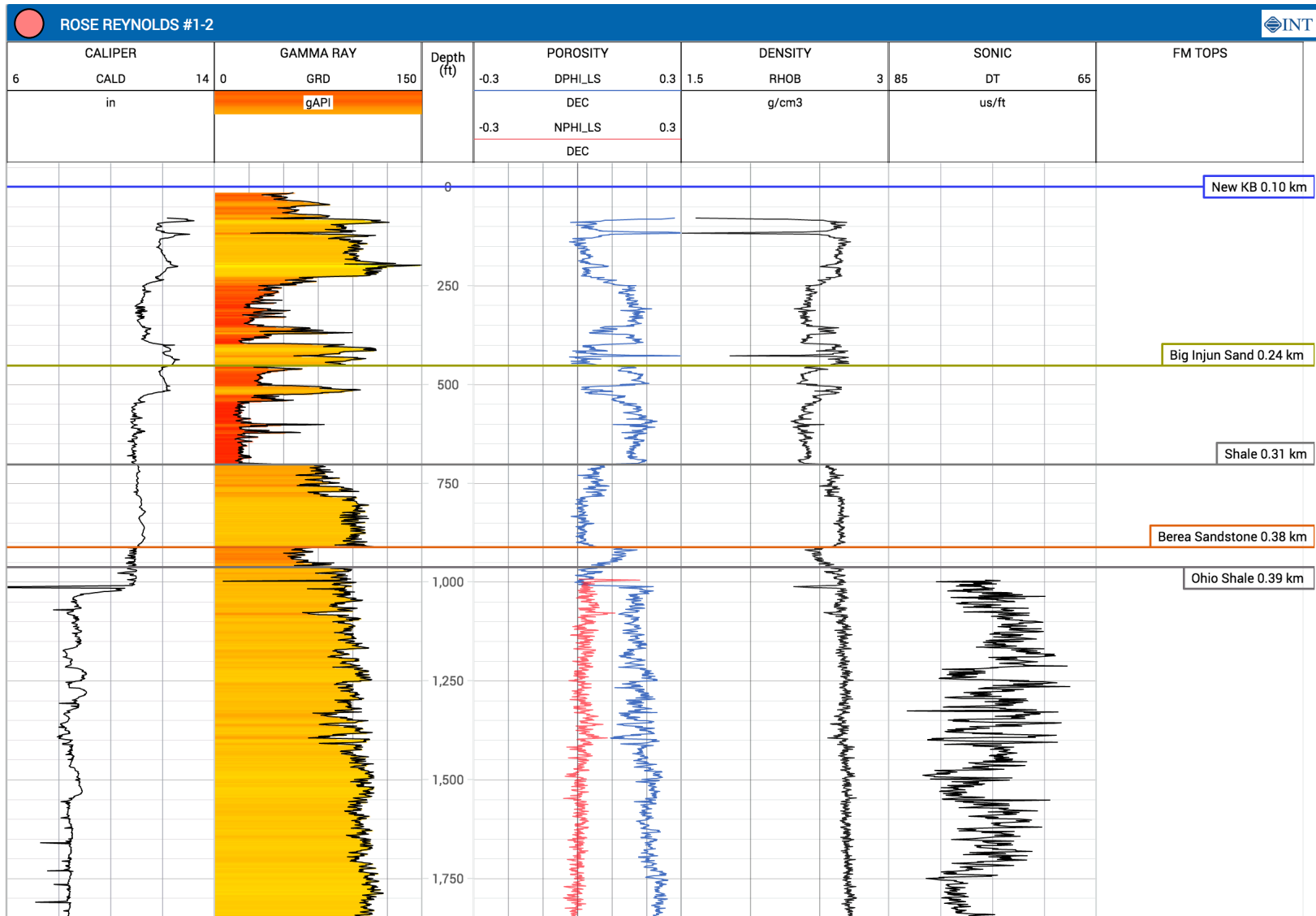


Figure 3.8: Rose Reynolds (RR) digital well data for the first 0.66 km (primary depth of investigation). The right-most column shows top-of-formation depths, based on top-of-formation data and referenced to the common datum used in this study. The location of the well is shown on Figure 3.10.

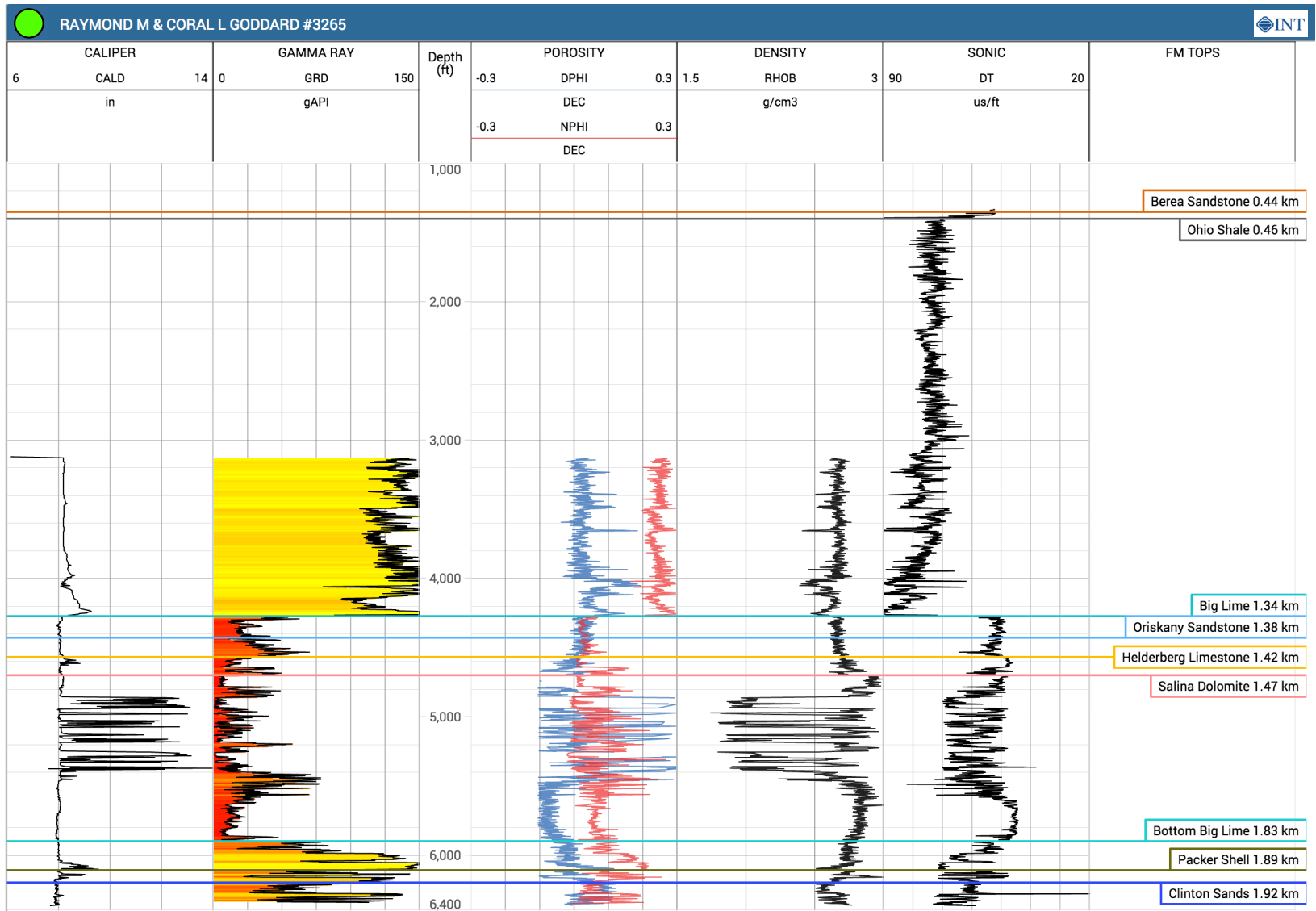


Figure 3.9: Raymond Goddard (RG) digital well data for the entire depth of the log. The right-most column shows top-of-formation depths, based on top-of-formation data and referenced to the common datum used in this study. The location of the well is shown on Figure 3.10.

3.1.3 Survey parameters

The seismic line was acquired by a mix of vibroseis and dynamite sources and was 26.8 km in length (Figure 3.10). Use in this thesis was limited to a southern portion (15.9 km) of the line in order to reduce modelling time, and to provide minimal projection errors going from a crooked geometry to a straight geometry. The selected 15.9 km line contains 501 unique source positions and 995 unique receiver positions. The survey follows a rough topography, with a maximum of about 100 m in elevation change (Figure 3.11). The data were acquired in a split-spread configuration with standard offsets for the purpose of reflection seismic processing. A typical shot had 219 active receivers to the South and 219 active receivers to the North, with a maximum offset of 3.5 km. The source point spacing was 34 m and the receiver group spacing was 17 m resulting in approximately 115 fold data. The data were correlated vibroseis records stacking two sweeps (24 m apart) of 6 to 120 Hz over a record length of 8 s.

3.1.3.1 P- and S-waves

Three directional components of the seismic data were collected, but I made use of the vertical component only in this thesis. The two horizontal components were discarded because the P-wave vertical component solution was deemed to be robust, and *fullwv* does not account for S-waves. Several challenges arise when including elastic effects such as S-waves and PS converted waves (Castellanos et al., 2011; Lu et al., 2013). One of the largest challenges problems is an increase in the non-uniqueness and the non-linearity of the inverse problem. By including S-waves, more unknown parameters must be solved. If, for example, the fully 3D anisotropic elastic wave equation is used, 21 independent elastic constants must be solved (see Appendix A). The problem of a correct parameterization of such a problem remains an issue and one that will perhaps be better solved using a data science technique known as ‘machine learning’, in which computer algorithms are taught without being explicitly programmed. The second perhaps equally challenging problem by increasing the number of parameters is the increase in computational cost. Currently, the research of elastic FWI (especially in 3D) is limited to the most expensive high-performance computing (HPC) systems in the world. The problems, however, associated with not including the effects of S-waves can also be severe, especially in complex geological environments. However, in the cases where incorporating the effects of S-waves may only add computational cost and not additional geological information, it is not necessarily important to incorporate these effects.

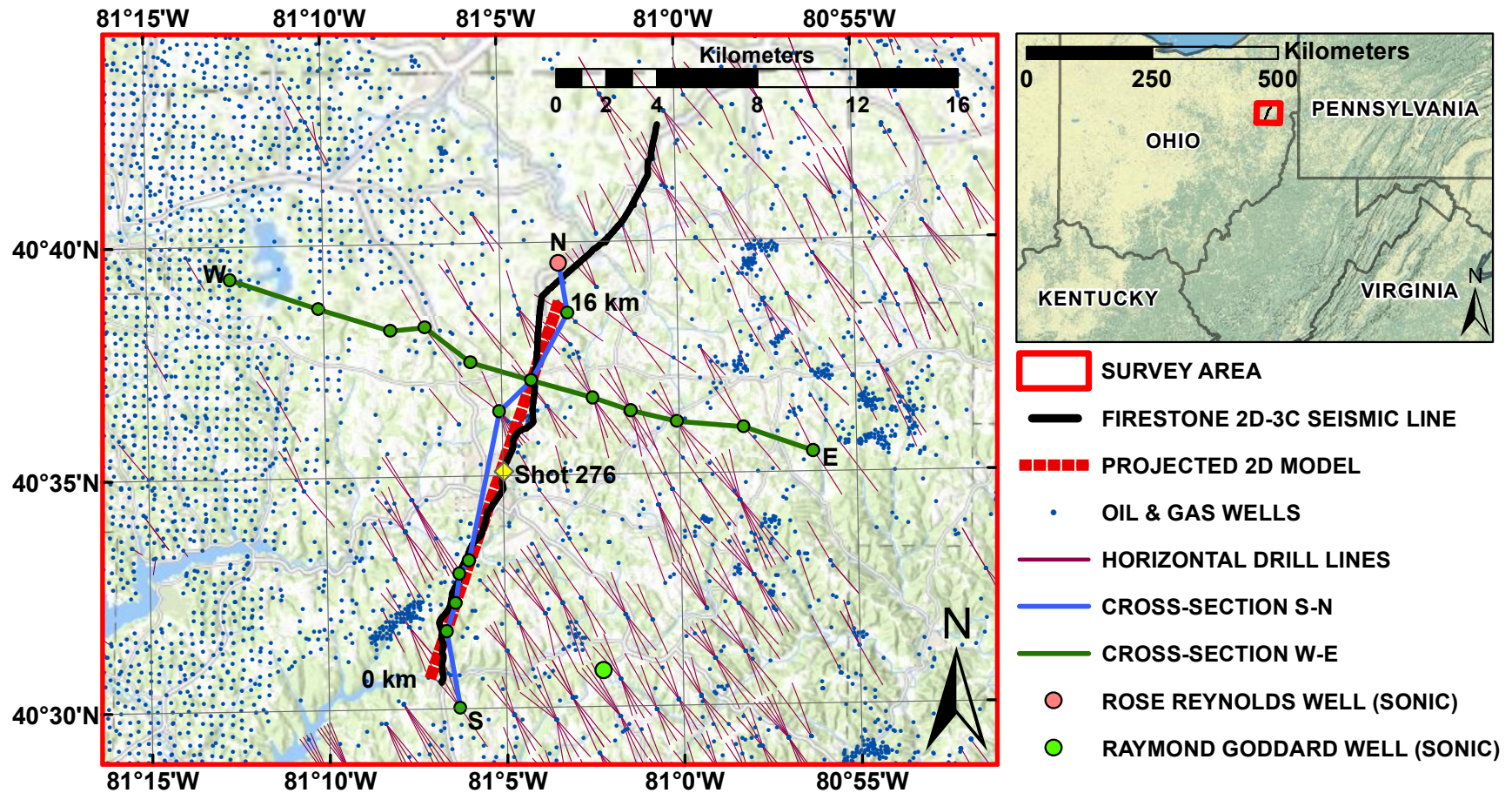


Figure 3.10: Detailed map of survey area. Many subsequent plots can be geographically situated on this map. Numerous active and inactive oil and gas wells are displayed as blue dots in the area (ODNR Oil and Gas Resources Management, 2016), some dating back to the early 1900s. Many of the more recently drilled wells 2010 and later have used hydraulic fracturing and horizontal drilling to capture higher quantities of oil and gas from the Utica shale reservoir.

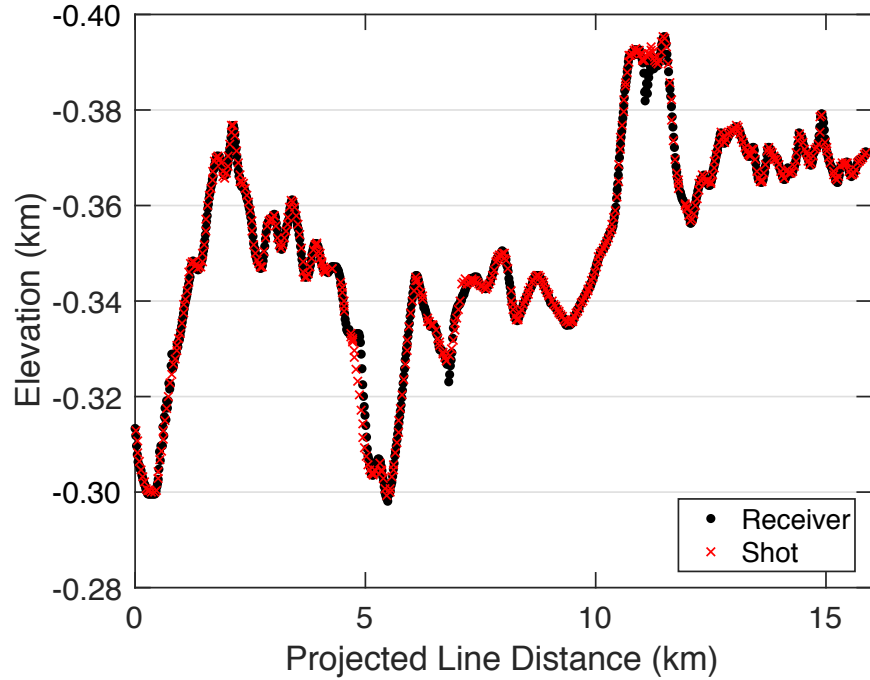


Figure 3.11: Shot and receiver elevation (negative elevation is above mean sea level). The vertical axis has been stretched significantly to show variation.

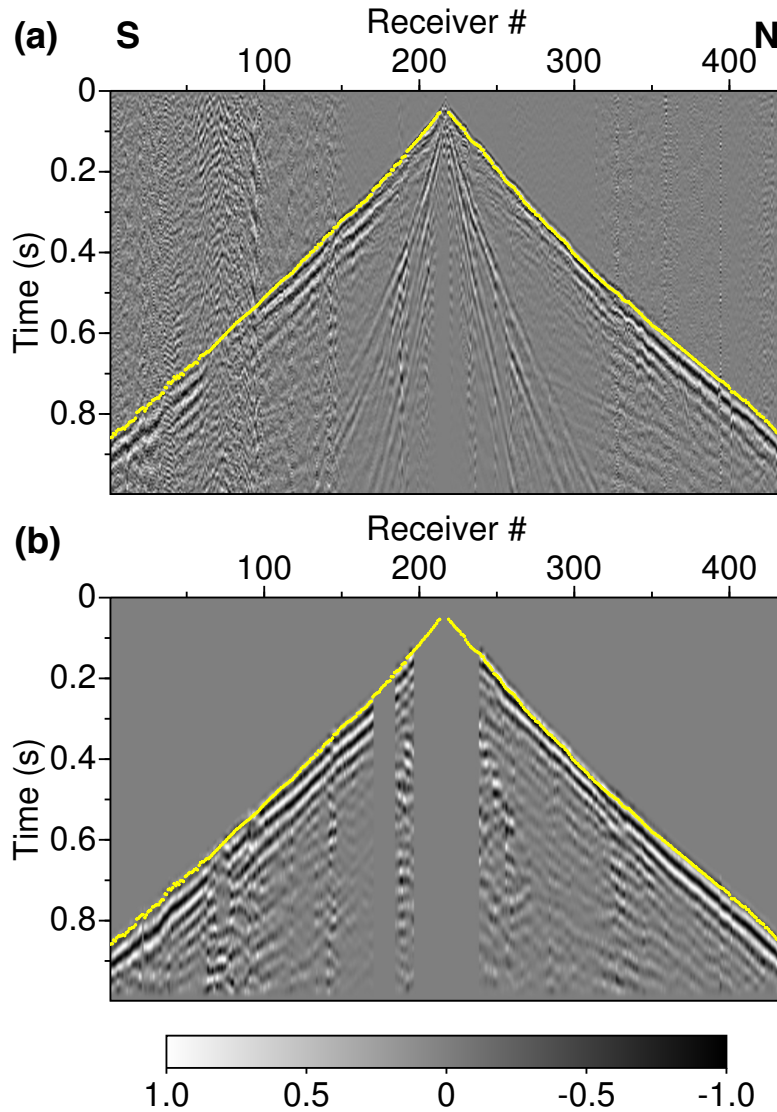


Figure 3.12: (a) Raw shot gather and (b) preprocessed shot gather # 276 at 8.8 km along the line (located on Figure 3.10). Shot gathers have been trace normalized for display purposes. First break picks are in yellow.

3.1.4 Seismic data preprocessing

Seismic data for FWI were received from Arcis in 2015. The only preprocessing they carried out on the raw data we received for FWI was a minimum phase conversion (from zero-phase). I completed additional preprocessing on the data in order to ensure that the data were fit for FWI. I handpicked first-break times on 501 shot records, or on a total of 193,940 traces. Figure 3.12 shows a raw shot gather with my first-break picks. For all unusable (noisy) traces, first breaks were not picked, and these traces were not used in FWI. The first breaks were later used as input data to building the first velocity model through travelttime tomography.

In preparation for 2D FWI, the original (x, y, z) coordinates were projected onto an (x, z) plane,

where x is the inline coordinate, y is the crossline coordinate, and z is depth. A line of best fit was assigned for the receiver (x, y) positions, followed by a coordinate rotation of the both the shot and receiver positions to the $y = 0$ plane (also rotating the line of best fit). After rotation, the crooked coordinates were projected onto the best-fit line. Time errors on the predicted arrival times resulted from the projection. So, to mitigate these errors, the offsets were calculated in 3D (before projection) and in 2D (after projection), and the percentage difference between these values was used to discard data where the difference between the projected 2D offsets and 3D offsets was greater than 3%. Figure 3.13 depicts the percentage error in a plot of source number vs. receiver number. The plot reveals regions of discarded data where the projection error percentage is greater than 3%. The discarding of data was one solution that mitigated areas where traveltimes errors in the new projected coordinates would create errors in the velocity model. Discarding seismic data implies, unfortunately, that there are certain regions that would not inform the velocity model during FWI updates. However, because there were still so many useable data, there was little impact on the final FWI result.

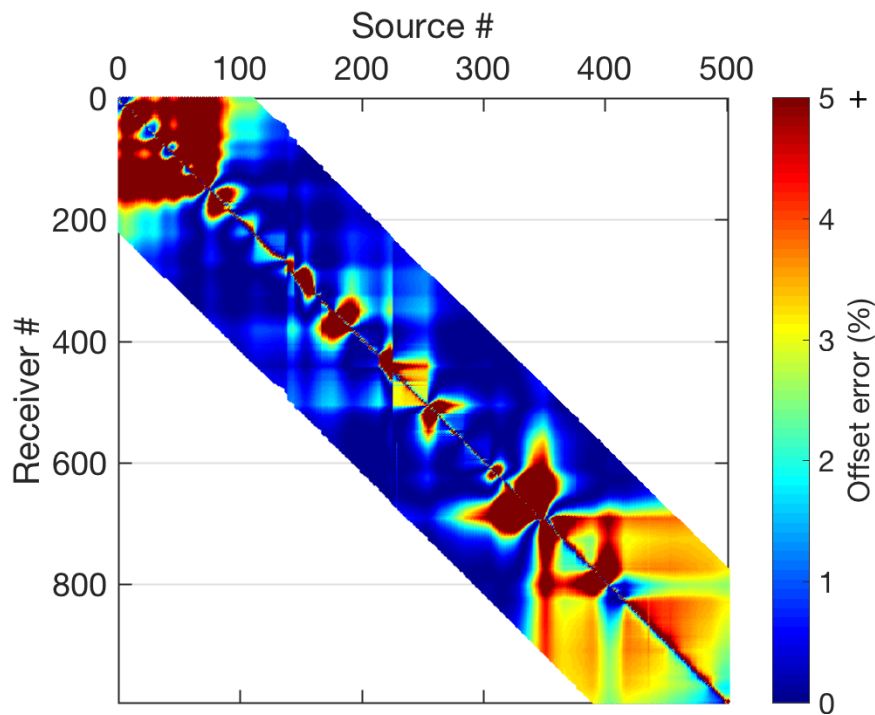


Figure 3.13: Offset percentage error from the projection of 3D to 2D offsets. Data with offset error greater than 3% were discarded.

The data preprocessing also included

- (1) applying an f - k filter to suppress the effects of ground roll,
- (2) applying a zero-phase Butterworth filter with corner frequencies 0-0-20-40 Hz,
- (3) killing traces with i) no first-break picks or ii) absolute offsets less than 350 m,

- (4) muting 30 ms before first-break picks,
- (5) applying a linear moveout (LMO) of 4500 m/s,
- (6) padding every shot with zero traces to full offset coverage for use in *fullwv*, and
- (7) applying a Laplace-Fourier transform to the time data.

The bandpass filter in step (2) was applied to the data to ensure that the observed data matched in bandwidth the FWI forward modelled data. Concerning step (3), there were certain traces that did not warrant picking a first-break, due to the noise present. If the trace was too noisy to pick a first-break, it was also considered too noisy to use in FWI. The near-offset data less than 350 m were eliminated to further suppress the effects of ground roll. In step (4), the mute applied was to ensure that no noise before the recorded waveform arrivals was an input to FWI. Applying LMO in step (5) was helpful in compressing the data to 1 s while keeping later arrivals. This compression is helpful specifically because when taking the LF transform, less interval frequencies are required with a shorter total time in the trace. Step (6) of shot padding was necessary only because the code *fullwv* expects that every shot has a full-survey offset range. Figure 3.12 shows shot 276 before and after all preprocessed steps except for (5)–LMO.

A Laplace-Fourier (LF) transform was taken of the time-domain preprocessed data in preparation for a LF domain FWI. The advantage of using the *Laplace*-Fourier transform over just the Fourier domain is that special weight can be placed on early transmitted arrivals (see equation 2.14). These arrivals have much of the low-wavenumber content needed for background updates in FWI. Fourier (or frequency) data for the minimum (12 Hz) and maximum (26 Hz) frequencies are displayed in Figure 3.14. These two panels are the Fourier transform of the time data, and serve as two of the data inputs to *fullwv*. A filter to exclude data based on their offsets is included in *fullwv*; therefore, it was not necessary to exclude all offsets in preprocessing.

3.2 Velocity model building and validation

In conventional reflection processing, the velocity model used during migration is often very smooth (Yilmaz, 2001). However, in FWI, the goal is to build an interpretable velocity model image with resolution similar to a final migration image. The resolution in a migration image often shows the distinction of strong impedance contrasts (sharp features) and some structural geological features. The goal in using FWI is to imitate or improve upon this kind of resolution, but without as many steps as are required to reach a final migration image. To obtain a starting velocity model that satisfies the half-cycle criterion for FWI, I used 3D first-break traveltimes tomography, a velocity model building tool. Traveltimes tomography achieves a much lower resolution than FWI and is therefore not typically suitable for final interpretation.

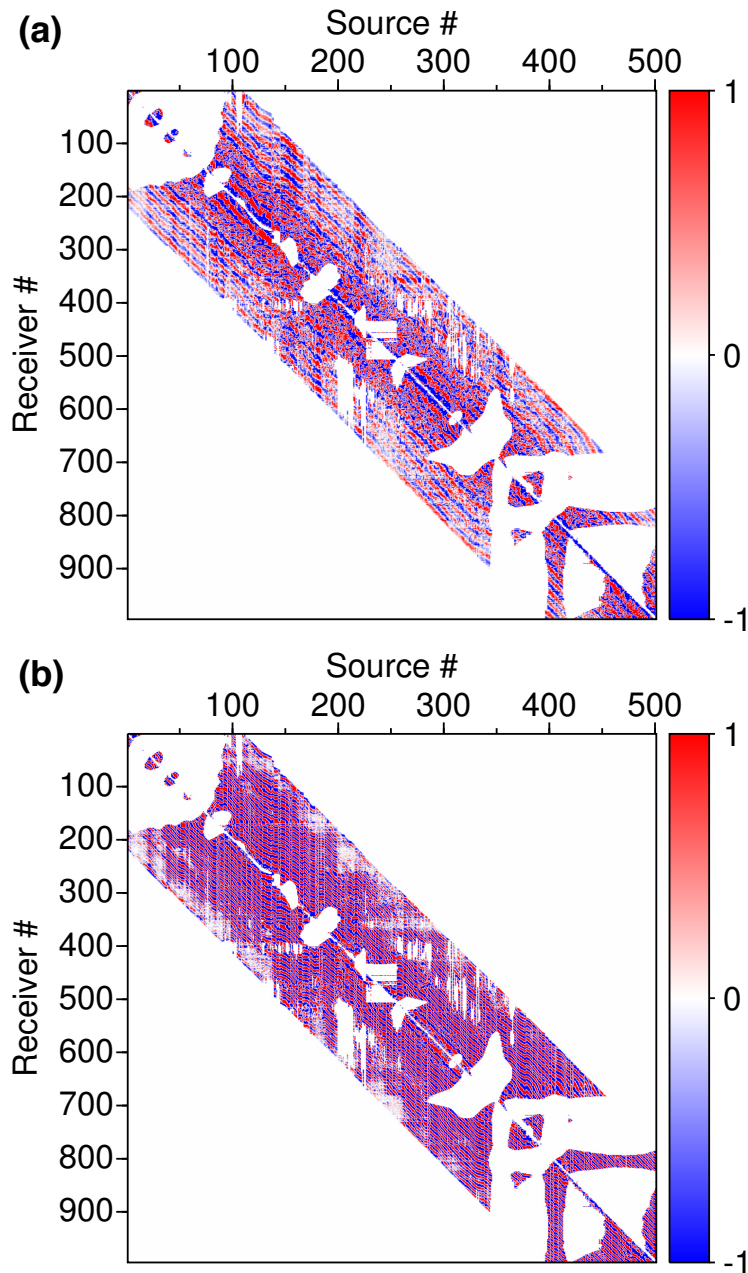


Figure 3.14: Two examples of the Fourier transform of the time data used as the input for the FWI code *fullwv*: (a) 12 Hz observed data and (b) 26 Hz observed data. Most sources had 438 associated receivers. The white gaps represent the areas where data were discarded due to the projection from 3D to 2D, and the regions with no data due to limited offset coverage. Data have been trace normalized for display purposes.

3.2.1 Applying 3D first-break traveltimes tomography

The seismic line was acquired along a crooked path, extending about 1 km in the crossline direction. Tomography in 3D properly preserves the original crooked (3D) geometry, avoiding the need for any projection. The initial grid-based model for traveltimes tomography was built by picking along common first break slopes (Figure 3.15). During this process, anomalous picks were eliminated that were far outside the normal bounds. Before beginning traveltimes tomography, the model was smoothed so that rays would not get trapped along sharp boundaries between velocity layers. The initial model produced by this building process is shown in Figure 3.16. To start tomography, a coarse grid was used at first, and later a finer grid. Table 3.1 summarizes the strategy used in the decrease of grid spacing.

Table 3.1: 3D traveltimes tomography strategy

Block	Grid spacing (x, y, z) in m	Iteration #
1	40, 40, 10	1-6
2	40, 40, 10	7-10
3	8.5, 8.5, 8.5	11-13

One of the validation techniques in traveltimes tomography is to see a decrease in the misfit of the objective function (equation 2.1). Such a decrease in misfit occurred between hand-picked first-break traveltimes and simulated first-break traveltimes. Figure 3.17 depicts this decrease by showing the root mean square (RMS) misfit at each shot location. The RMS misfit decreased from approximately 14 ms to 6 ms, a sign that the tomography was converging. For each block, ray tracing was completed through the velocity model. Figure 3.18 displays a ray density plot through the initial model. The depth of penetration of rays reached a maximum of around 0.58 km. Very few rays penetrate deeper than 0.43 km, however, and not much of an update occurs below that point. However, the depth of penetration of the waveforms during FWI are consistently much deeper (0.66 km), as the waveforms are sensitive to broad-band “wavepaths,” which are more broad than rays (Woodward, 1992).

In order to make use of the 3D traveltimes tomography updates in a 2D FWI scheme, a 2D slice had to be taken out of the final 3D traveltimes tomography model. Stated another way, a 3D model cannot serve as an input to a 2D algorithm without some manipulation. To ensure that the updates from traveltimes tomography were used, a slice of the model was taken along the receiver path. The model was then smoothed before FWI.

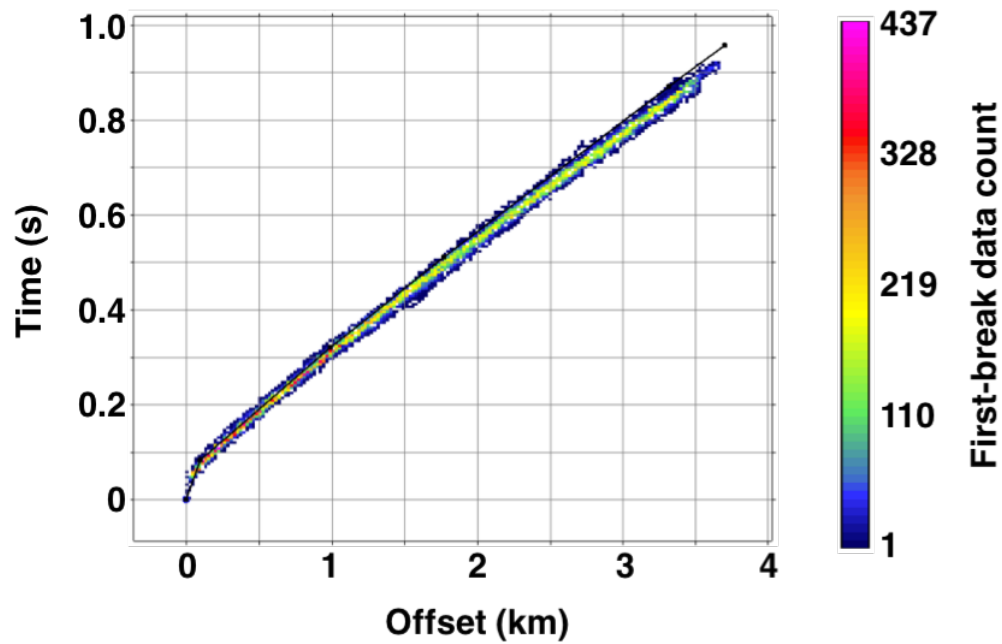


Figure 3.15: Common first-break pick plot. The vertical axis represents the time of the first-break picks on the shot gathers, and the horizontal axis represents the source-receiver offset distance. The coloration represents the density of first-breaks at a specific time and offset. The initial model for traveltome tomography was built by tracing along common picks.

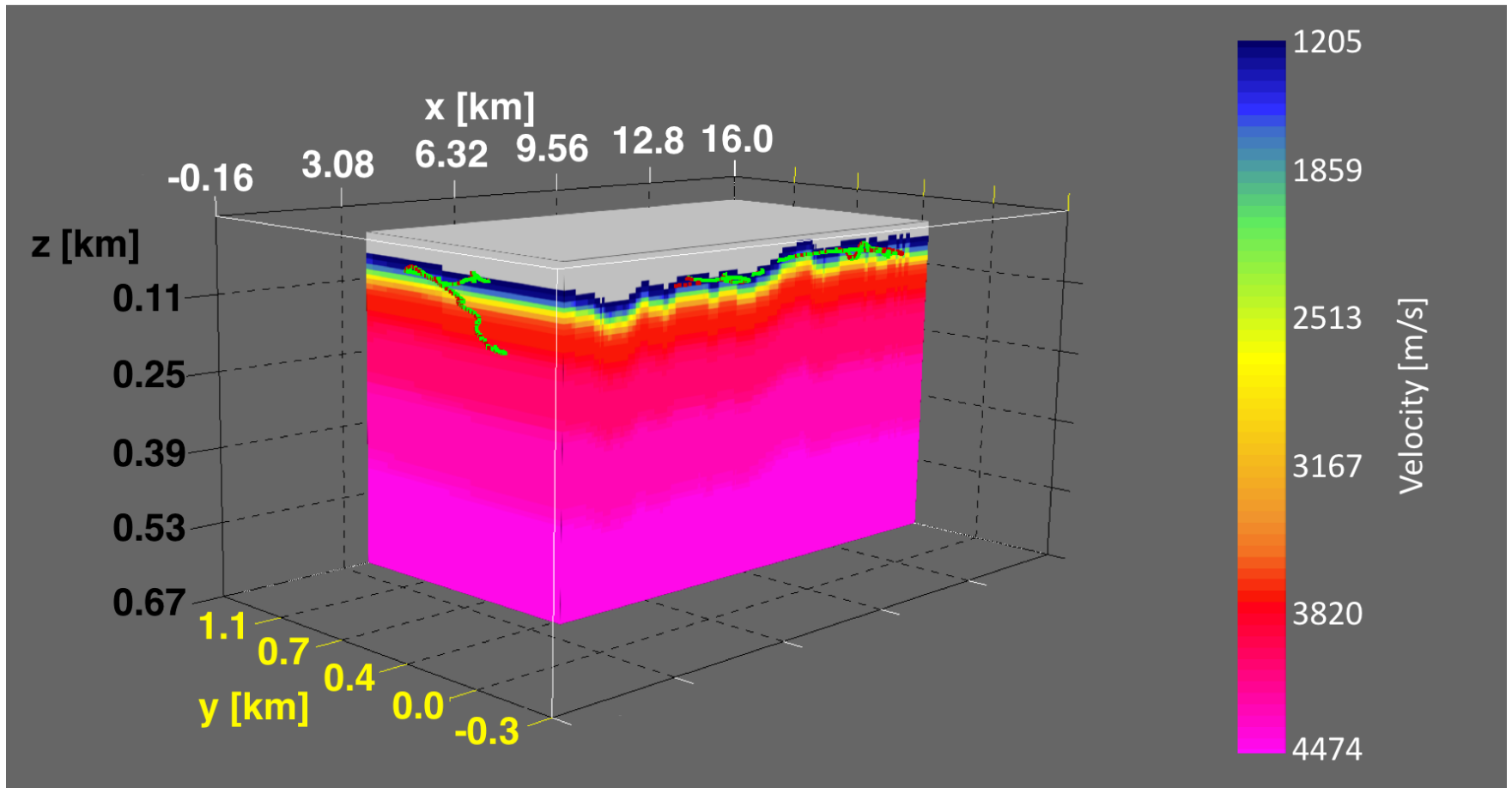


Figure 3.16: Starting velocity model for traveltime tomography. The cube has been ‘sliced’ at $x = 3.76$ km, $y = 0.35$ km, and $z = 0.05$ km. The light grey colour represents the air layer with a velocity of 340 m/s, but no rays were permitted to travel in the air during tomography.

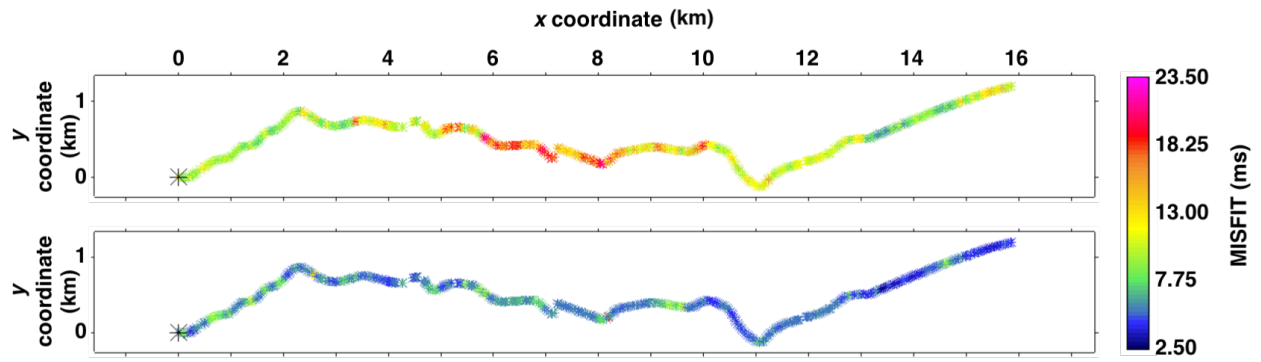


Figure 3.17: In map view after coordinate rotation, the 3D traveltime RMS misfit (in ms) at each shot location along the crooked line before tomography (top), and after tomography (bottom). The x coordinate represents the inline direction, and the y direction represents the crossline direction.

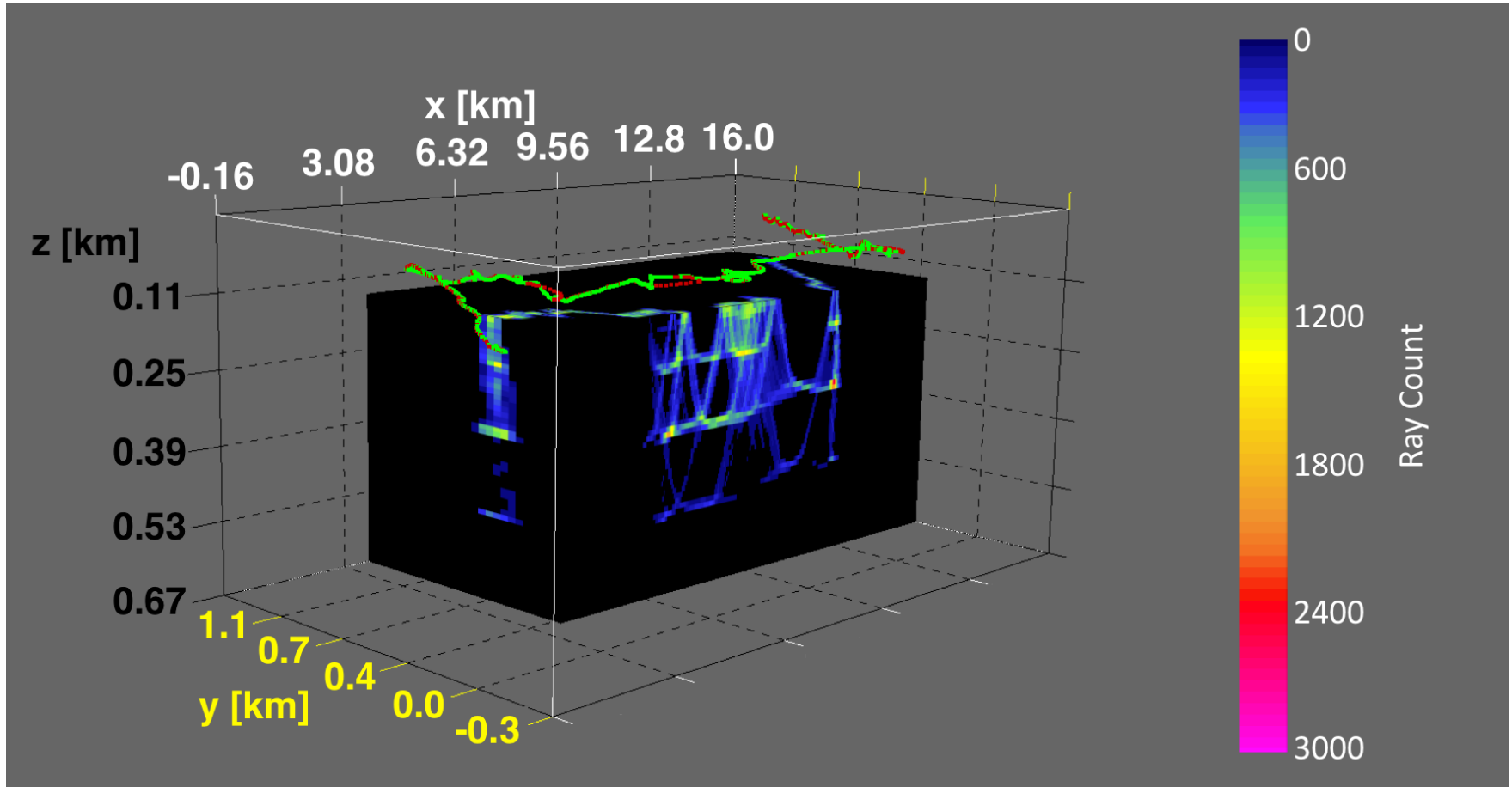


Figure 3.18: The ray density count shows that the first-break rays reached a maximum depth 0.58 km. The cube has been ‘sliced’ to show the ray count at $x = 3.76$ km, $y = 0.35$ km, and $z = 0.17$ km.

3.2.2 Applying 2D FWI with the SSP

3.2.2.1 Multi-scale strategy

In the early stages of FWI, the primary goal was to continue to update the background velocity. In order to do that, the lowest possible frequencies with the longest wavelengths were used. Longer wavelength or low-wavenumber content produce very broad updates. Using lower frequencies also helps to avoid converging on local minima in the misfit functional. The data below 12 Hz had very poor signal-to-noise ratio and were not able to provide adequate information for FWI updates. The FWI strategy is displayed in Table 3.2. In frequency block 1, a synthetic delta-function wavelet was used; but in blocks 2 and 3, inverted sources were used. A multi-scale approach was used for FWI, beginning with the lowest available frequencies of 12 to 14 Hz, and ending with frequencies of 21 to 26 Hz. I stopped the inversions at 26 Hz, as no more meaningful updates resulted by going higher in frequency. Noise began to dominate the velocity model after 26 Hz, no longer resembling geologic strata.

Table 3.2: 2D FWI strategy

Block	Frequency (Hz)	Iteration #	μ_x	μ_z	Offset coverage (km)
1	12, 13, 14	1-100	16	0.72	$0.45 \leq \text{offset} \leq 2.50$
2	15, 16, 17, 18, 19, 20	101-200	16	0.72	$0.45 \leq \text{offset} \leq 2.50$
3	21, 22, 23, 24, 25, 26	201-233	2.8	0.13	$0.45 \leq \text{offset}$

3.2.2.2 Modelling parameters

All velocity models were referenced to a depth of 0 m at a datum of 426.7 m above mean sea level. The topographic surface at the boundary between the air layer and the subsurface served as a free-surface boundary to simulate reflections akin to a ground surface. A strong attenuation of $Q = 1$ in the air was used to further suppress wave propagation, and a weaker $Q = 400$ was used for the subsurface to allow for adequate wave propagation (see equation 2.18). A grid size of $grid_x = grid_z = 5$ m was used throughout all stages of FWI, small enough to avoid numerical dispersion, but large enough to keep computational costs down. The grid size should be less than or equal to a quarter of the minimum wavelength, written

$$grid \leq \frac{\lambda_{min}}{4}, \quad (3.1)$$

as in Jo et al. (1996). The minimum quarter wavelength for my model is approximately 11 m (at 1200 m/s and 26 Hz), which meets this criterion. 15 additional grid points were added to the velocity model on the left, bottom, and right hand side for the purpose of using perfectly

matched layers (PMLs). The PML region was used to absorb seismic waves, so that no artificial reflections were generated at model boundaries (Roecker et al., 2010). In the true subsurface, wave propagation is not limited by a ‘box’ of a model; rather, propagation should only create reflections at the topographic surface and at any reflectors and other geologic structure.

Within the forward modelling code, a tau-damping parameter of $\tau = 0.35$ s was used to emphasize early arrivals and suppress later arrivals (see equation 2.14). Variations on the damping factor were tested, but did not yield additional information for the inversion, and thus were not used. Some offsets were filtered using a cosine taper function. Figure 3.19 shows an example of such a taper with corners A, B, C, and D. Near-offsets were not included due to the potential interference of ground roll. Far offsets are more prone to cycle skipping, and in the presence of significant anisotropy have the potential to skew velocity updates. The corners of the offset taper for blocks 1 and 2 were 0.35, 0.45, 2.5, and 3.5 km. The corners of the offset taper for block 3 were 0.35, 0.45, 5.0, and 5.0 km (allowing all far offsets). Allowing far offsets in the last block added new information to the inversion. The idea is that some of the more significant background updates would have already taken place by the last (higher) block of frequencies. Table 3.2 summarizes my offset tapering strategy.

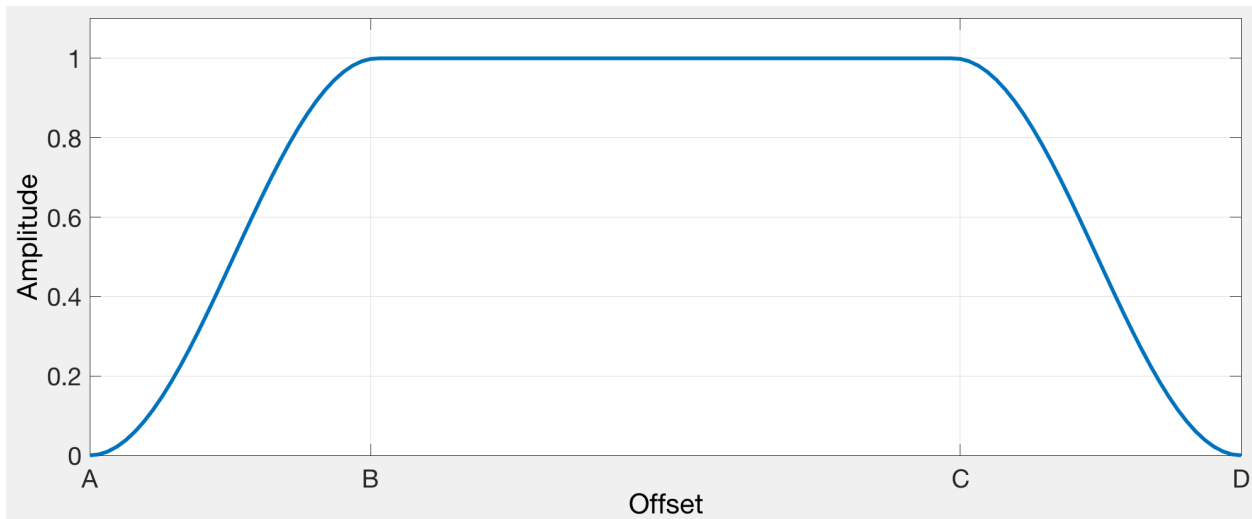


Figure 3.19: Example offset taper filter used with corners A, B, C, and D.

3.2.2.3 Results

The raw gradient (equation 2.30) and the gradient with the SSP (equation 2.32) for the first iteration of 12-14 Hz are displayed in Figure 3.20. The raw gradient (a) has noticeable migration ‘smiles’ that are undesirable, but also contains excellent low-wavenumber content extracted using SSP (b). The low-wavenumber content can be seen as very smooth white coloration (b). Applying the SSP to the raw gradient results in a large spatial scale, which is helpful in early iterations. The use of the

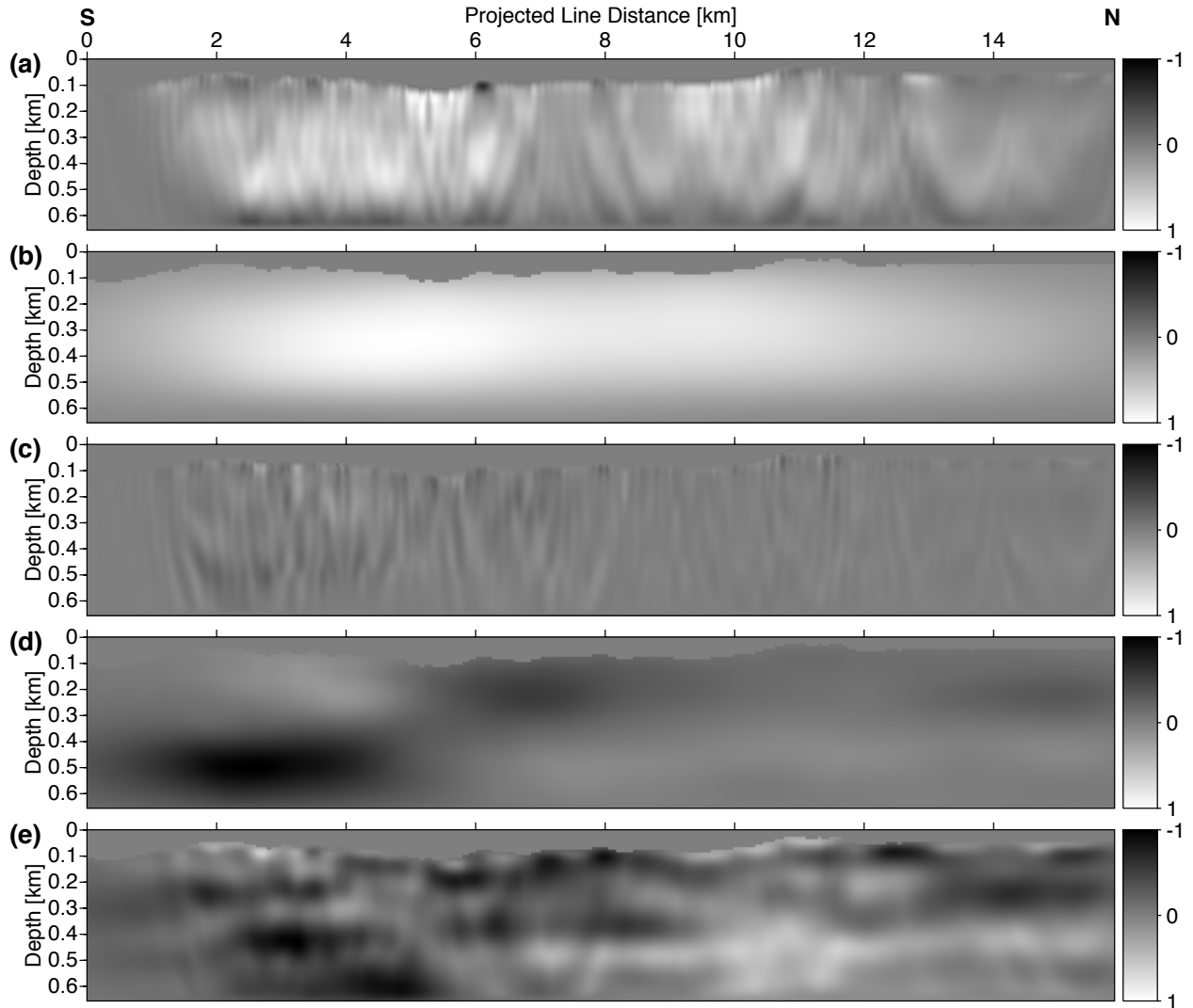


Figure 3.20: Gradients for 12-14 Hz: (a) raw gradient at iteration 1, (b) preconditioned (SSP) gradient at iteration 1, (c) raw gradient at iteration 100, (d) preconditioned (SSP) gradient at iteration 100, and (e) conjugate gradient at iteration 100.

SSP allowed high-wavenumber perturbations to constrain the low-wavenumber updates and enter the model as iterations continued. When the background updates are already accounted for at later iterations, the gradient allows more high-wavenumber updates to occur (d). The high-wavenumber content can be seen by the sharp contrasts between black and white in the gradient, likely geologic layering. The raw gradient (c), preconditioned gradient (d), and the conjugate gradient (e) for the last (100th) iteration of 12-14 Hz are also shown in Figure 3.20. The conjugate gradient is an aggregate of the current SSP gradient and previous gradients (see Polak and Ribière, 1969; Mora, 1987). FWI with SSP allows low-wavenumber perturbations throughout the iteration schedule, including the later iterations when high-wavenumber content is explicit. The progression from low to high frequencies allowed a progression of finer-scaled features to appear in the velocity model.

Figure 3.21 shows the progression of velocity models from starting to final. Figure 3.22 depicts the differences between the velocity models. The difference plots are helpful to see what has changed as a result of adding each new frequency band. A progression from the lower frequencies in Figure 3.22 (a) to higher frequencies in (c) shows an increasing number of bands of red and blue (updates), signifying an increasing amount of higher-wavenumber content. There is also more vertical and close-to-vertical structure appearing in (c) not present in (a).

The SSP scale factors were chosen to match the dimensions of the model (equation 2.32 and table 3.2). A smaller μ_z than μ_x in the model domain translates to a larger (elongated) k_z than k_x filter in the wavenumber domain. Wavenumber plots of the difference between velocity models are shown in Figure 3.23. The effects of the anisotropic filter by choosing different SSP scale factors are evident: each plot shows an elongated k_z compared to k_x . These plots further support the fact that new wavenumber content is distributed over the inversion frequency blocks. The warmer colors (green, yellow, red) in each plot show up in different places, which indicates that new content is being added with each frequency block.

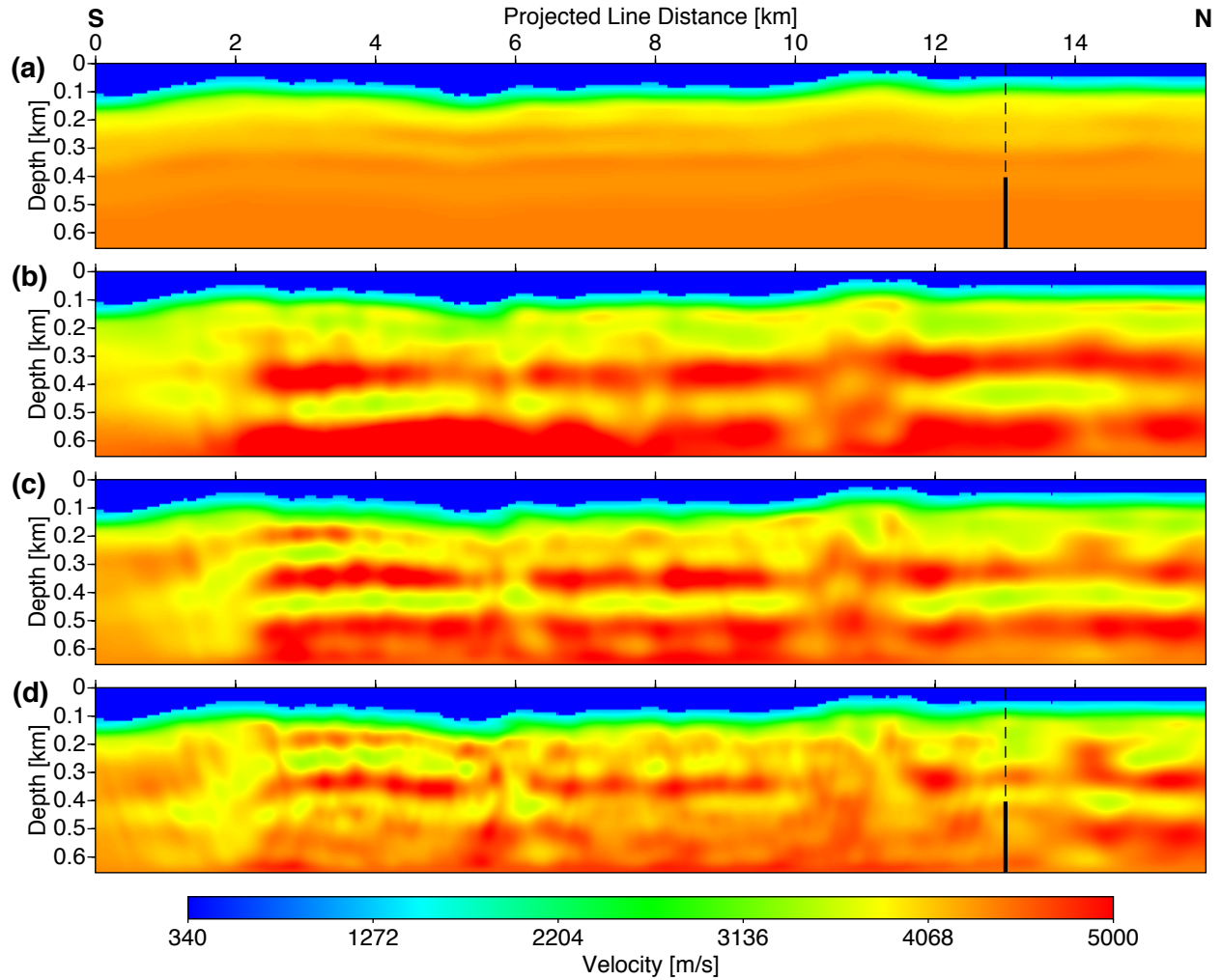


Figure 3.21: Progression of subsurface velocity models through FWI: (a) starting model for FWI after traveltome tomography, (b) after 12-14 Hz (iteration 100), (c) after 15-20 Hz (iteration 200), and (e) final model after 21-26 Hz (iteration 233). The dotted lines indicate the position of the 1D trace that was used for comparison to the sonic log; the thick solid black line indicates the depths where the sonic log has data (below 0.4 km).

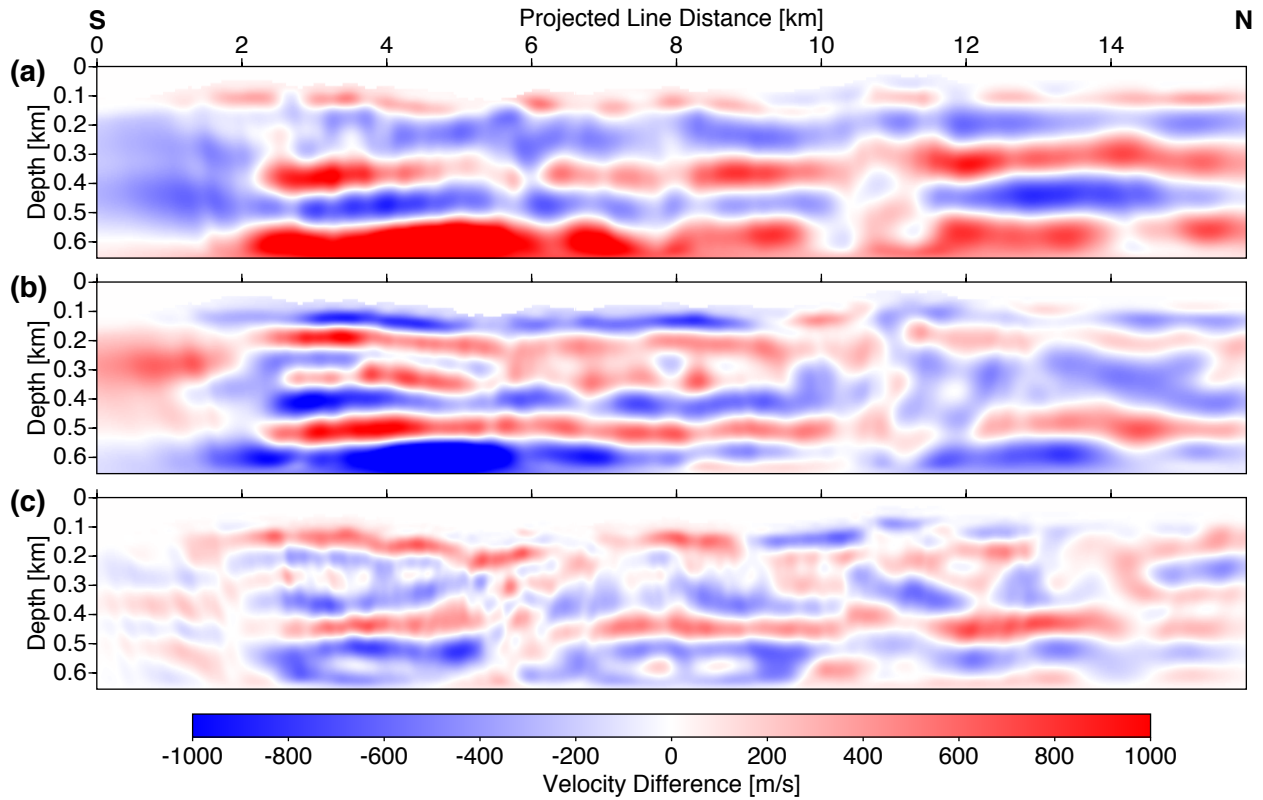


Figure 3.22: Velocity model difference plots: (a) the result of Figure 3.21b - 3.21a, (b) the result of 3.21c - 3.21b, and (c) the result of 3.21d - 3.21c. By keeping a consistent scale bar here across 3 plots, some values go above and below the values listed here. The left portion of the model remains without meaningful updates, due to a lack of data.

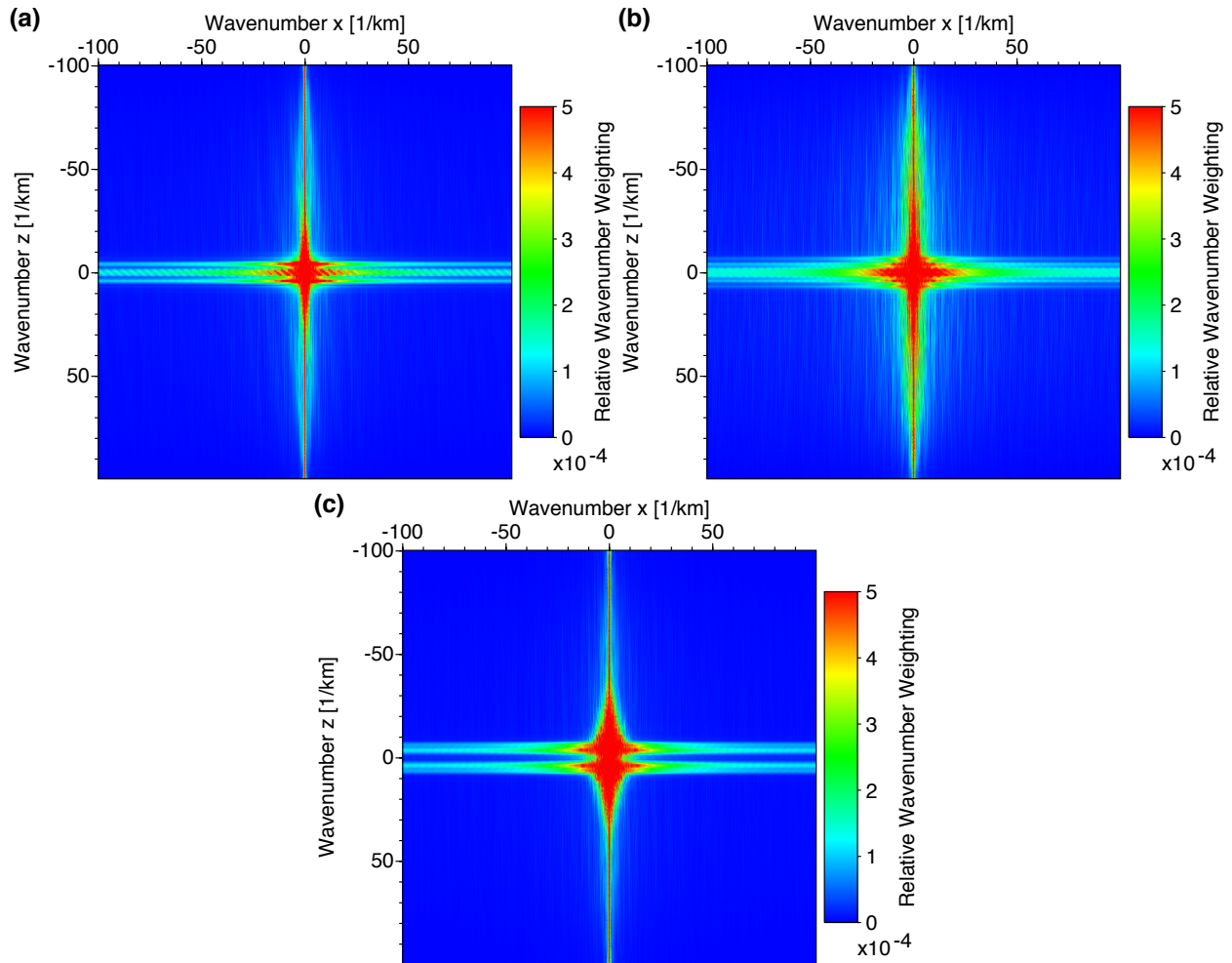


Figure 3.23: Wavenumber plots: (a) the $k_x \times k_z$ plot of Figure 3.22a, (b) the $k_x \times k_z$ plot of 3.22b, (c) the $k_x \times k_z$ plot of 3.22c. Due to using a smaller SSP scale factor in the z direction (μ_z), the k_z wavenumbers are elongated as compared to the k_x wavenumbers.

3.2.3 Validation of final results

An extensive set of tests were used to confirm that the updated velocity models in Figure 3.21 were of high quality. These included:

- (1) the significant reduction in the misfit functional,
- (2) a comparison of the forward modelled data to field data,
- (3) a comparison of the final velocity model to a nearby sonic log,
- (4) a scrutiny of the coherency of inverted source signatures after each frequency block,
- (5) an overlay of a seismic migrated section on top of the final velocity model, and
- (6) an overlay of geologic layers from the geologic cross-section.

Figure 3.24 shows the progress of the misfit functional for each of the 3 blocks of FWI. The Brent line search that was used guarantees a reduction at every iteration. I chose to stop iterating for each frequency block based primarily on (1) a decrease in the misfit functional by approximately 47 %, but also (2) a qualitative assessment of data fit, and (3) the limit of coherent geologic structure (as opposed to noise). The significant reduction in the misfit functional is one indicator of a successful inversion scheme. Often it is difficult to obtain a convergence of more than 10% for field data (M. Zuberi, personal communication, 2017).

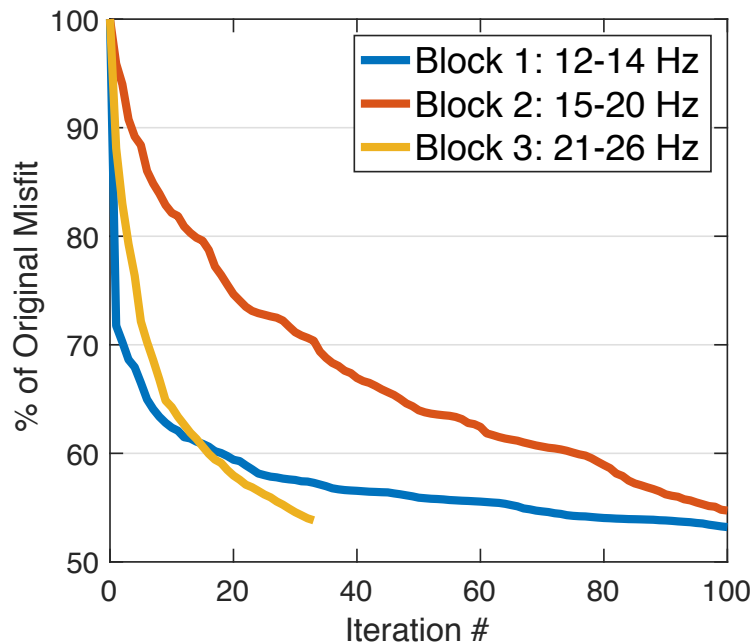


Figure 3.24: Misfit functional decreases in all three blocks of FWI by about 47%. The trends are slightly different because at each block, new frequencies were being introduced in the inversion scheme.

For each velocity model in Figure 3.21, data were forward modelled for frequencies 1 - 38 Hz and converted to the time domain. Figures 3.25 and 3.26 show these data. The data modelled from

the 2D-projected (and smoothed) traveltimes tomography result show a close match in first-break arrival times to the field data; however, there are packets of refracted wave energy that do not match in phase. There are some improvements in data fit after each block. Figure 3.27 shows the final forwarded modelled data and the preprocessed field data with labels A, B, C, D, and E overlaid. The far offset (around 3.2 km) arrivals on the left side (A) come in later in the final modelled data than the preprocessed field data. However, the right hand side of the shot shows a better fit for far-offset arrivals (E). At location B, the modelled data follows the small shift in arrivals, but also adds another (black) arrival that is not present in the field data. Many of the near-offsets located around D show a good match of phase between modelled and observed refracted arrivals. There are some reflected arrivals present in the modelled data (C) with a normal move-out velocity of 2400 m/s that are not present in the field data. A careful look at the final velocity model in Figure 3.21 reveals a strong contrast in velocity from the very near-surface layer of 1300 m/s (teal colour) to a jump to 2400 m/s (green). A sudden jump in velocity like this would almost certainly create a reflection. However, because these arrivals are mostly contained within the muted offset zone and tau-damped zone, they do not play a significant role in model updates.

Sonic measurements from the nearby Rose Reynolds well did not begin until a depth of 404 m. However, the sonic data that are available help to validate the FWI results at the bottom of the model. The sonic measurements were converted from measured units of microseconds per foot ($\mu\text{s}/\text{ft}$), to meters per second (m/s) to compare with velocity models. The log was padded with zero values up to the same datum of 426.7 m as the velocity model for comparison. A lowpass filter was applied with corner frequencies 0 - 0 - 3 - 6 Hz to bring the wavenumber scale of the log to a scale similar to the final velocity model. Upscaling the sonic in this way is only a rough approximation, and is therefore treated as such when making comparisons.

Figure 3.28 shows a plot of the original sonic log, the lowpass filtered sonic log, the starting velocity model, and the final velocity model. The location of the vertical profile from the velocity model (at 13.0 km) was picked as close as possible to the log. On the rightmost (north) side of the model (Figure 3.21), there were less seismic data informing the FWI updates. The absence of data in this particular region was due to the fact that the data were acquired over a crooked portion of the line, and thus had more offset projection errors going from 3D to 2D. As a result, the location of the 1D sonic log as placed on the model was not only informed by its vicinity to the model, but also an area of the model that had updates from seismic data. Beyond that, the edges of the model (including the rightmost edge) are least resolved because of fewer data with no sources or receivers beyond the model extents. The plots in Figure 3.14 explicitly reveal the regions of the model with no updates (white). A very strong match between the filtered sonic and the final velocity model to a depth of 0.5 km is present.

A mismatch exists between the FWI result and the sonic log below 0.5 km, and this could be due

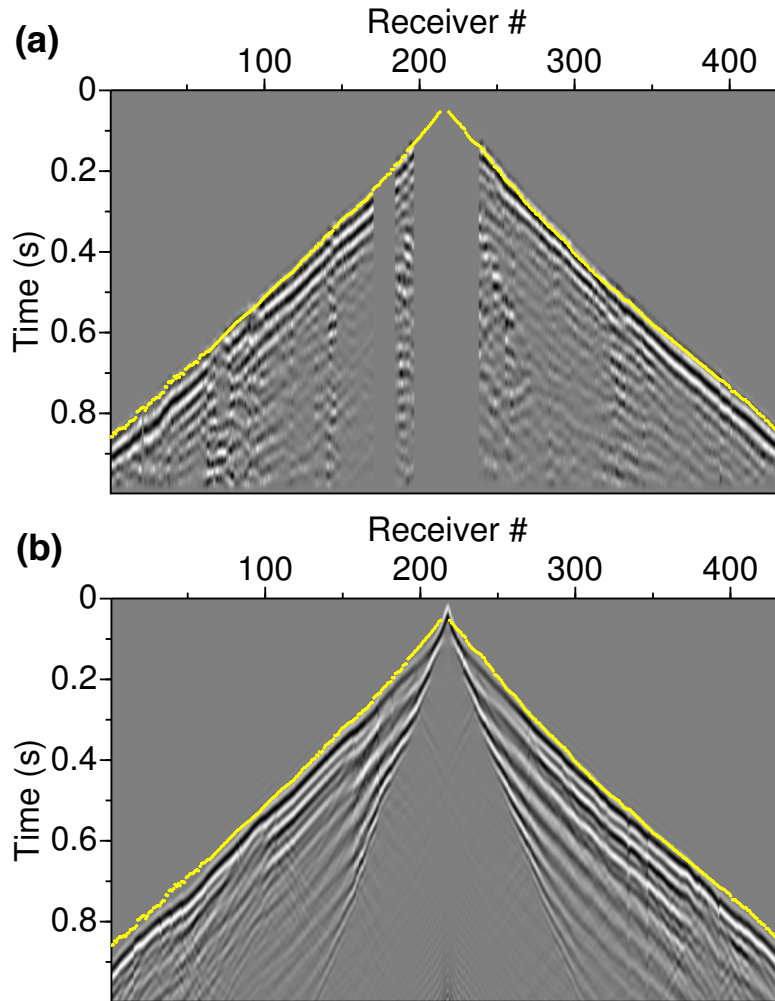


Figure 3.25: Forward modeled shot # 276: (a) preprocessed data, and (b) from traveltime tomography starting model. The source position is 8.8 km along the line (located on Figure 3.10). Shot gathers have been trace normalized for display purposes. First break picks are displayed in yellow.

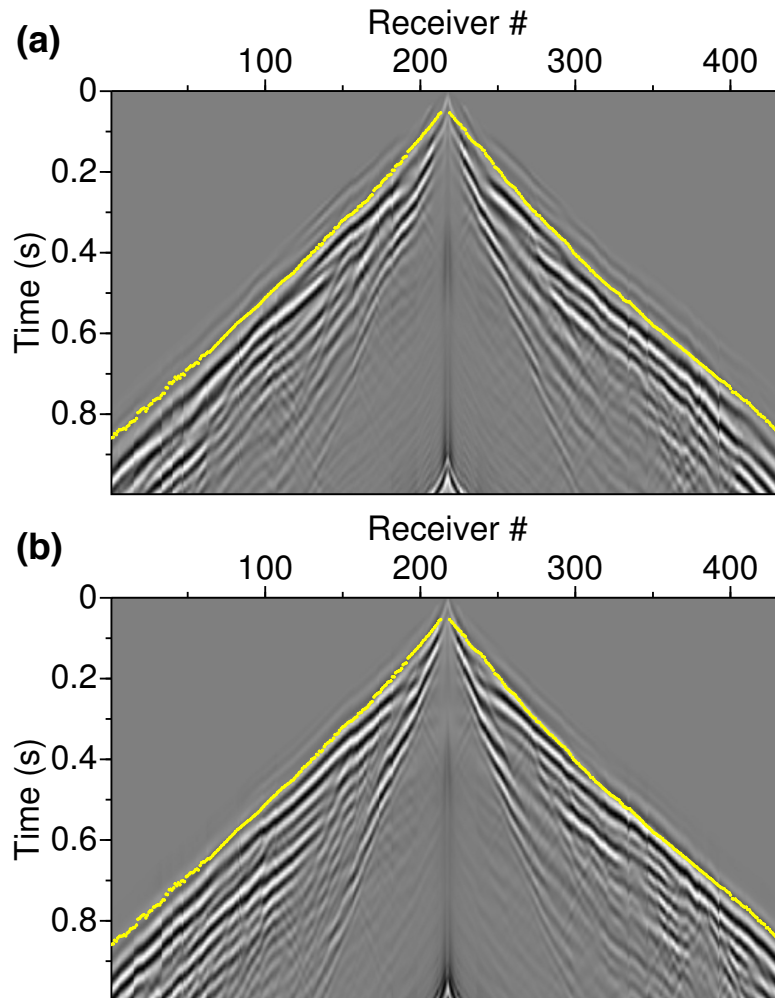


Figure 3.26: Forward modelled shot # 276: (a) after 12-14 Hz FWI (iteration 100), and (b) after 15-20 Hz FWI (iteration 200). The source position is 8.8 km along the line (located on Figure 3.10). Shot gathers have been trace normalized for display purposes. First break picks are displayed in yellow.

to a number of factors. One such factor is that the penetration depth of the majority of transmitted waves may have been above 0.5 km throughout most of the inversion, because of my limiting of the offsets. The mismatch could also be due to not accounting for out-of-plane effects, and S-wave effects. Another challenge not accounted for was anisotropy. The sonic measured in this borehole is a vertical measurement of velocity, whereas the updated FWI model is primarily a measurement of horizontal velocity. At farther offsets, the seismic wave has traveled more horizontally than vertically, and in layered media is more susceptible to the effects of anisotropy (Thomsen, 1986). A likely scenario in a flat-laying stratigraphic environment is vertical transverse isotropy (VTI). More details of the elastic tensor in VTI media and associated wave equations can be found in Appendix A. There are two primary ways of handling velocities in the presence of strong anisotropy in the oil and gas industry for the purpose of tying wells to seismic data: the first is to incorporate the effects of anisotropy (such as VTI) into the FWI forward modelling algorithm to match the well data, and the second method is to ignore anisotropy completely in the FWI forward modelling algorithm, but rather account for anisotropy at the well itself (eg., Birdus et al., 2015; Hornby et al., 2003). The portion where such a procedure may have been fruitful in this study is at the very deepest (below 0.5 km) portion of the FWI model, but because this is the portion where I have some of the least confidence, I did not make the effort of including the effects of anisotropy.

In discussing the depth extent of the FWI result, it is helpful to understand where the velocity model is sensitive to waveforms. Figure 3.29 presents the ‘sensitivity kernels’ or ‘wavepaths’ (Woodward, 1992) computed for single source-receiver pairs with an offset distance of 2.5 km. In Chapter 2, Figure 2.1 showed a visual representation of the action of the gradient for a single source-receiver pair, or a ‘sensitivity kernel’. These kernels are shown using the lowest and highest frequencies in the inversion, 12 Hz and 26 Hz. Both kernels present a deeper penetration than traveltimes tomography (Figure 3.18), but also much thicker. Instead of only using ‘thin’ rays in traveltimes tomography, FWI uses the ‘thick’ wavepaths to update the model. Velocities resolved using FWI are most often resolved on the order of the size of the wavelength, but the depth extent of the sensitivity kernel indicates the depth penetration expected in the FWI result. It is worth noting that the portion below 0.5 km in the sonic and model comparison that did not perform well matches closely with the depth extent of these sensitivity kernels. For the first 2 blocks of FWI, 2.5 km was the maximum offset allowed (Table 3.2), so these sensitivity kernels to some extent represent the maximum depth of penetration for the majority of the inversion work. The whole left portion of the velocity model was not updated significantly (see Figure 3.22), due to the absence of data in the region.

An initial set of source inversions was completed after traveltimes tomography, and also after every block of FWI, in order to measure of the quality of the FWI results, and to use as sources for blocks 2 and 3. Figure 3.30 shows the inverted source signatures from the corresponding

models presented in Figure 3.21. The sources were inverted over all modelling frequencies (1 - 38 Hz), and subsequently band-passed to show only the frequencies used in the FWI scheme (12-26 Hz). Stepping through the recovered source signatures from top to bottom reveals significant improvement in collapsing multiple events to a single front-loaded wavelet, giving me confidence in my results.

A final root mean square (RMS) velocity model and a post-stack time migration image were received from Arcis at the same time as the raw seismic data were delivered. The post-stack time migration was converted to depth using a smoothed version of the Arcis RMS (picked) velocity model, and was overlaid on the final FWI velocity model (Figure 3.31). A good tie exists between the reflectors and the general shape of the structures in the model. The image resolution offered in the FWI velocity model comes close but does not reach the level of resolution of migration, as migration used higher frequency data and impedance contrasts.

The discussion of a velocity models may lead to the question: how does the FWI model compare to the more conventional RMS velocity models extracted using velocity analysis of the reflector moveouts? On one level, this question may be irrelevant: if the goal in FWI were to obtain a stand-alone interpretable image, there is no need to migrate the final FWI velocity model, and no need for an RMS velocity model. One may interpret directly on the final FWI velocity model. A lot of processing time could potentially be saved by avoiding picking RMS velocities, and avoiding the rest of seismic processing necessary for migration. On another level, the question may be appropriate: if the goal in FWI were to obtain a more accurate near-surface model than that achieved through RMS velocity analysis, for the purpose of migration, then FWI again could be worthwhile. The result of getting more accurate velocities in the near-surface using FWI should help correctly position the reflectors at greater depths. An inaccurate or less-resolved RMS model in the near-surface may not correctly position the deeper reflectors. In the oil and gas industry, FWI is most often being applied in the near-surface of geologically complex environments that have not been resolvable using a conventional RMS velocity analysis approach, resulting in the proper focus and placement of deeper reflectors, or other important features such as salt bodies, faults, and even oil-water contact points.

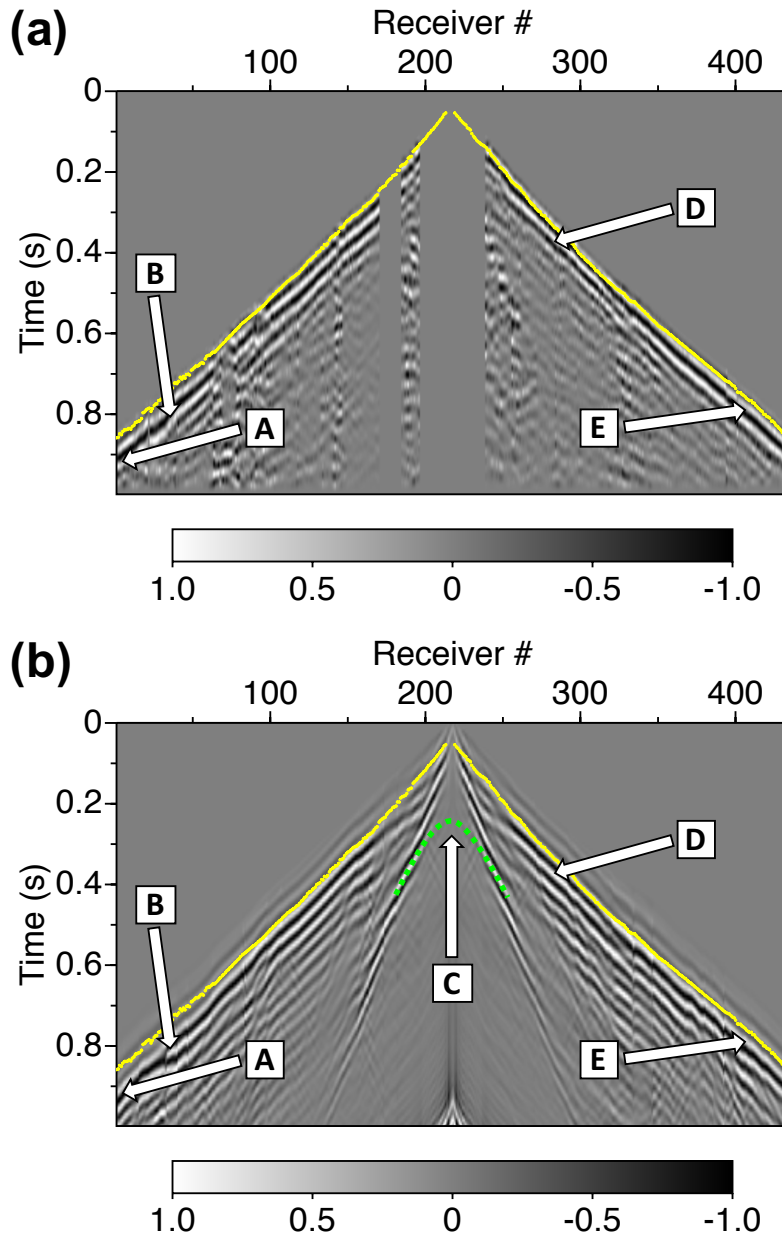


Figure 3.27: Shot # 276: (a) Preprocessed field data, and (b) final forward modelled data after 21-26 Hz FWI (iteration 233). A: The far-offset arrivals come in slightly late in the modelled data. B: The modelled data show a refracted arrival package not present in the field data. C: Multiple reflections occur at the very near surface of the velocity model, where it changes rapidly from 1300 m/s to 2400 m/s. D: A good match in phase exists here between modelled and field data. E: The far offsets on the right hand side show an excellent fit. The source position is 8.8 km along the line (located on Figure 3.10). Shot gathers have been trace normalized for display purposes. First break picks are displayed in yellow.

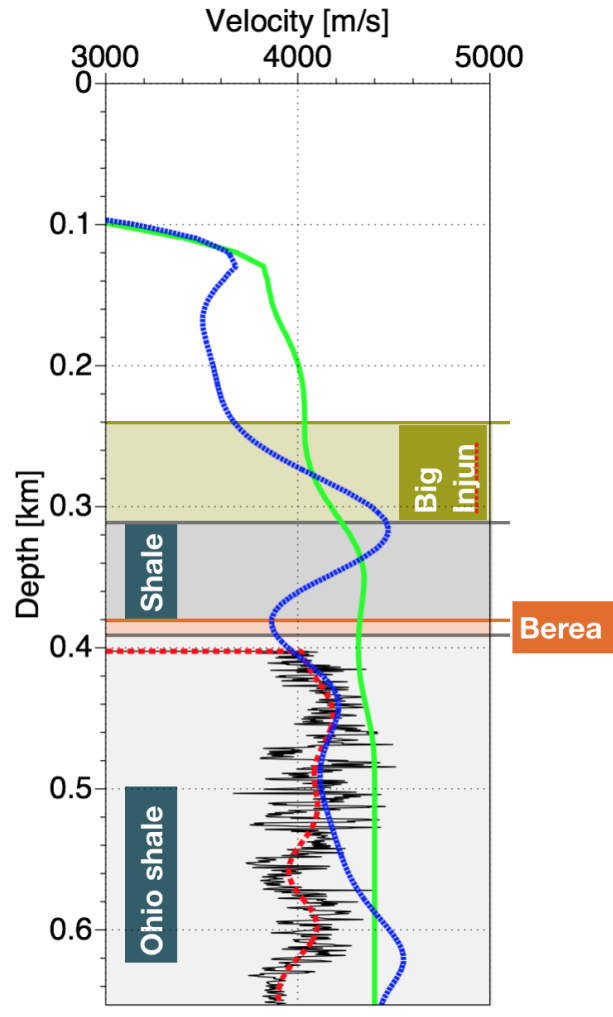


Figure 3.28: The Rose Reynolds well showing the original sonic log (black line), a lowpass filter (corners 0 - 0 - 3 - 6 Hz) of the sonic log (red dashed line), the starting velocity model (green line), and the final FWI velocity model (blue line). The location of the well is about 1.5 km away from the survey line (indicated on Figure 3.10).

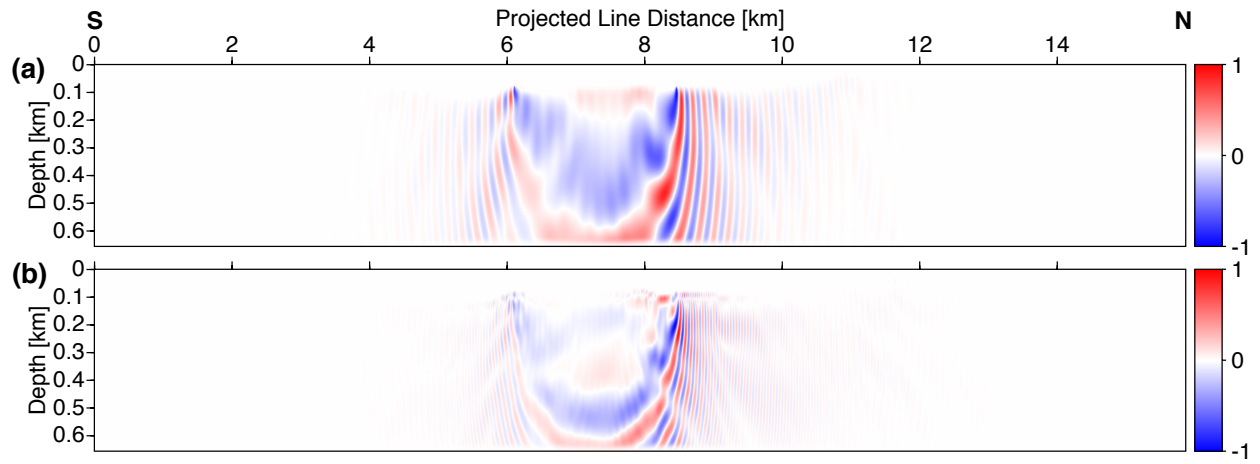


Figure 3.29: Sensitivity kernels at (a) the minimum frequency of 12 Hz, and (b) the maximum frequency of 26 Hz. The kernels have a source-receiver offset distance of 2.5 km (70% of maximum offset).

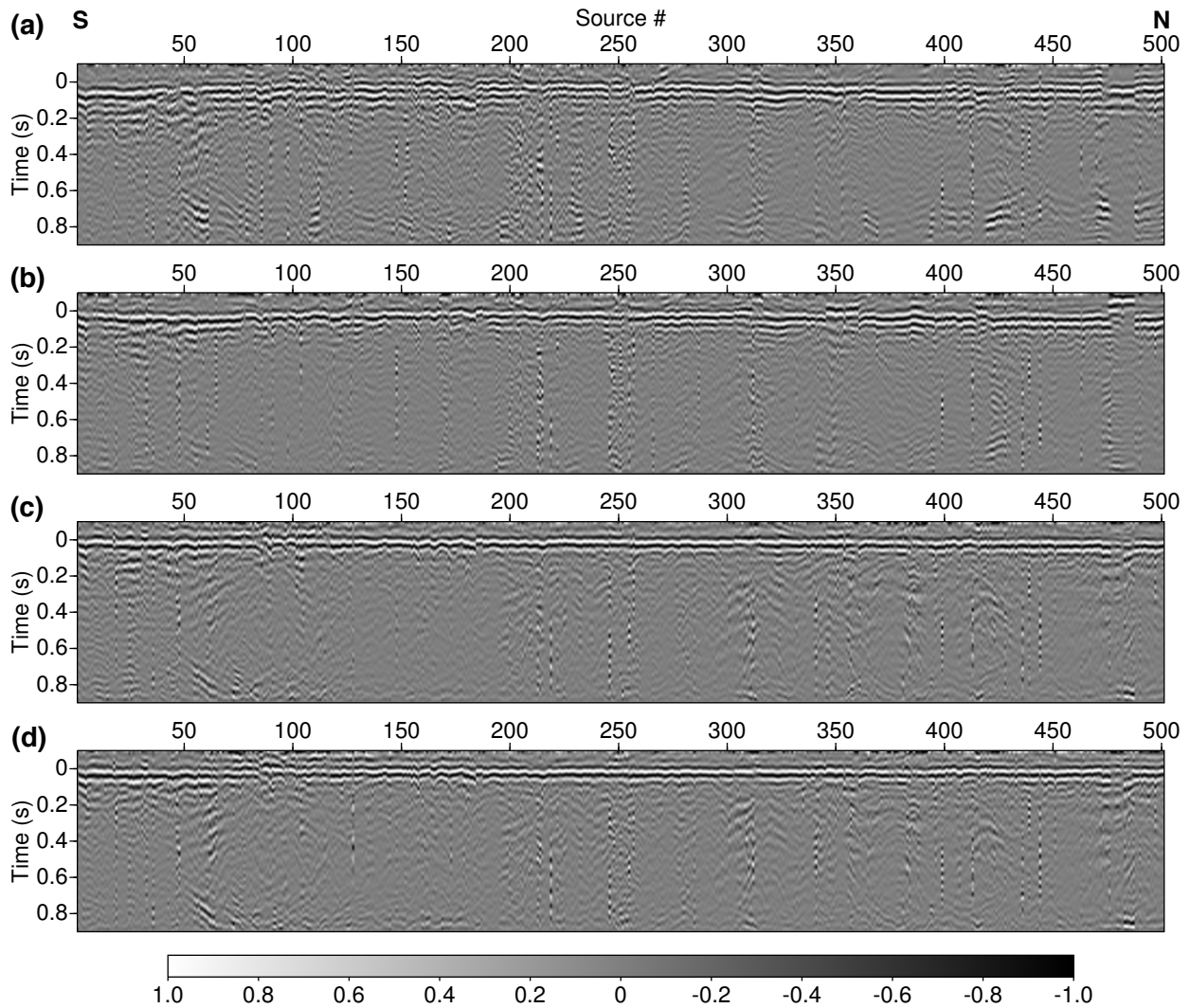


Figure 3.30: Source inversions: (a) from the starting model, (b) after 12-14 Hz (iteration 100), (c) after 15-20 Hz (iteration 200), and (d) after final 21-26 Hz (iteration 233). The source profiles were trace balanced for display purposes. Progressing from (a) to (d), we see multiple events collapsing to more of a front-loaded single event. The multiple events in (a) appear as multiple ‘reflections’ near 0 s, but in (d) appears more often as a single coherent ‘reflector’ near 0 s.

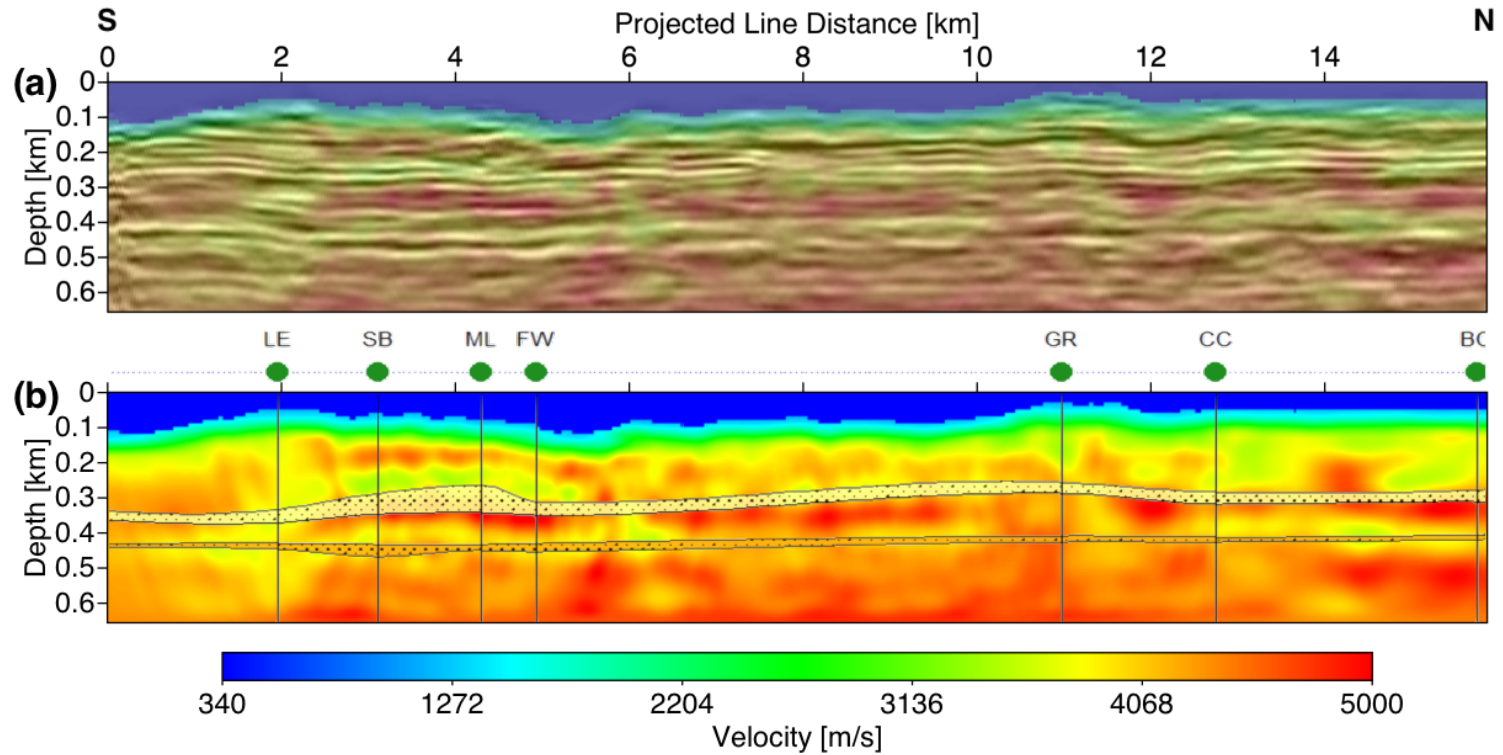


Figure 3.31: Final FWI velocity model with (a) seismic stack overlaid, and (b) formations Big Injun sand (yellow) and Berea Sandstone (orange) overlaid. Final FWI velocity model with S-N well tops cross-section (from Figure 3.5) overlaid. Well locations are approximate, due to their crooked traverse on top of the straight (projected) traverse.

3.2.4 Geological interpretation

Current oil and gas resources in economic quantities are predominantly found in the Utica shale (Southworth et al., 1992), which are at greater depths than the velocity model that was derived here. However, a high-resolution near-surface velocity model can enhance image focusing at greater depths. The reprocessing of the seismic data and preliminary pre-stack depth migration results show slight improvements at depths greater than 2 km as a result of FWI in the first 0.66 km, and these can be found in Section 3.3, Reflection processing, though these results are still preliminary.

Figure 3.31 shows the final updated velocity model after 21-26 Hz FWI with the previously derived south-to-north cross-section overlaid. The beige layer from the well tops is representative of the top and bottom of the Big Injun sand. The trends in the velocity model follow the formation trends from the cross-section. The area between well FW and well GR moves slightly above the velocity model structure (top of the red), likely due to a lack of well control in that area. It is important to note that the well top locations are projected onto the velocity model (Figure 3.10) and do not represent a perfect fit. McCord and Eckard (1963) reported on a sonic log measurement taken from the W.B. Wright Well 2338 in Ritchie County, West Virginia that included the Big Injun sand. The velocities recorded in that sonic log for the Big Injun ranged from approximately 3858 m/s to 4762 m/s. These velocities are in the range of the final FWI velocities of approximately 4300 to 4800 m/s.

The orange layer in Figure 3.31 is representative of the top and bottom of the Berea sandstone. The updates from FWI captured a low velocity layer of approximately 4150 m/s at approximately 0.42 km depth, which I interpret as a velocity associated with Berea sandstone and surrounding shales. The shape of the Berea sandstone updates from FWI also match the slight dip to the South observed in the S-N cross-section.

3.3 Reflection processing

In the previous sections, the goal has been to use FWI on primarily refracted events to invert the Firestone seismic data to obtain a high-resolution near-surface (< 0.66 km) velocity model, but without ignoring some of the high-wavenumber content present in reflectors. The goal of my reflection processing is to focus efforts completely on the reflectors present in the data. My specific goal in reflection processing is to properly image the Utica shale reflector between 2.2 km and 2.5 km (see Appendix B). In this section, I present the results from a post-stack time migration by Arcis Seismic Solutions, my pre-stack time migration (PSTM) results, and my pre-stack depth migration (PSDM) results. I show that the PSDM result of using the FWI model obtained for the near-surface provides benefit in determining stratigraphy over only using interval- and depth-

converted velocities from Arcis' time model. For this dataset, I also show that using FWI has the potential benefit of replacing some of the statics calculations.

The attempt in this section is not to exhaustively detail the methods used in seismic processing, but rather to present and discuss results. [Yilmaz \(2001\)](#) takes care of complete descriptions of modern seismic data processing techniques complete with many field examples. I completed my processing work partly in Madagascar and VISTA Seismic Processing, but mainly in SeisSpace ProMAX Seismic Processing Software. VISTA contains a very simple way to build and execute processing workflows. The advantage of SeisSpace ProMAX is its time migration and depth migration workflows, which can use a velocity model from outside of the software. Running on 16 parallel cores, each 2D migration computed in time or depth took less than 5 minutes, an almost negligible run time. [Figure 3.32](#) shows two shot gathers from the middle of the Firestone line that have had processing applied by Arcis. An approximate refraction velocity is shown as 4663 m/s and a reflection normal move-out (NMO) velocity is shown as 4028 m/s.

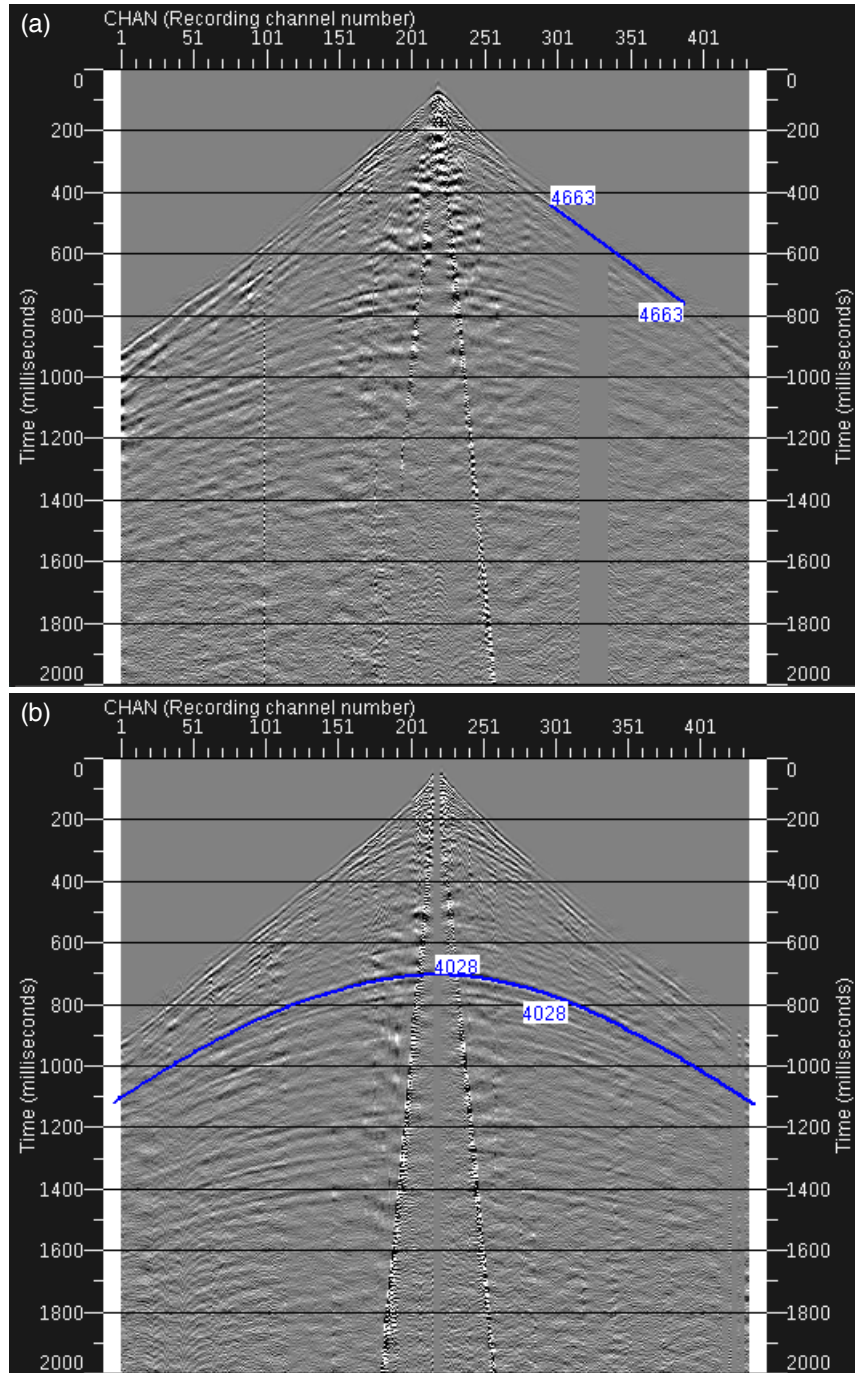


Figure 3.32: Two sample processed shot gathers from the output ‘PPDECON’ delivered by Arcis are shown here. The processed data were used as a starting point for migration work in time and depth. The first shot gather (a) has a blue line that shows an approximate velocity of 4663 m/s on a refracted event, and the second shot gather (b) has a blue hyperbola that shows an approximate NMO velocity of 4028 m/s on a reflected event. The maximum offset from source to receiver is 3.5 km. Shot gathers have been trace balanced for display purposes.

3.3.1 Workflows

Substantial effort and time goes into processing seismic data. Often companies will spend many months working on the same dataset to ensure quality representations of the subsurface are produced. Kelly Beaglehole, Regional Geoscience Manager of Australia/Asia of DownUnder GeoSolutions, noted in a recent conversation that the expected minimum processing time for a small project is 3 months. I have only spent 1 month in processing due to time constraints; however, I can show some uplift by (a) creating a depth image, and (b) demonstrating some benefit of using my FWI results in migration. My results are preliminary only, and as a result should not be given as much weight as previous FWI validations previously discussed. The FWI velocity model can be used directly in depth migration, but would need to a conversion from depth to time for use in time migration. Rather than make that conversion, I use Arcis' NMO velocity model for time migration.

A diagram of the processing workflow that was completed by Arcis on the Firestone 2D-3C seismic line is presented in Figure 3.33. My work stands on the shoulders of the work already completed by Arcis, as I began my time and depth processing from one of their outputs, 'PPDE-CON'. Figure 3.34 presents my workflows for processing in both time and in depth. At the outset of my processing work, I converted all units from feet to meters to be consistent with the other work completed.

The process of static corrections in my FWI PSDM (depth imaging) workflow was abandoned. When seismic data are acquired onshore, there are a variety of subsurface velocity inhomogeneities that can 'distort' the wavefield. Here I use 'distortion' to describe primarily phase delays that later processing steps will not be able to handle effectively. In effect, the aim of statics is to create an artificially 'aligned' wavefield that has removed phase delays at various length scales (trace to trace, groups of adjacent traces, and longer spatial wavenumber variations of a spread length or more). Once that is done, we no longer require an accurate velocity model of the subsurface (e.g., based on first break traveltimes tomography and FWI) because we have already distorted the wavefield. Instead, we create a replacement pseudo velocity model of the subsurface. However, some of the statics calculations should not necessarily be abandoned, even if an FWI model is used in the near-surface (H. Geiger, personal communication, 2017). Unfortunately, I did not have access to the different stages of statics calculations, and so the choices I had were to either discard all statics, or keep all statics. With additional time and resources, I could also have completed my own FWI-oriented statics calculations, but a complete suite of migration images was not the primary goal of my thesis. Instead, I describe below the output of my reflection processing work carried out without static corrections, but it should be understood that my workflow for depth imaging is not optimal.

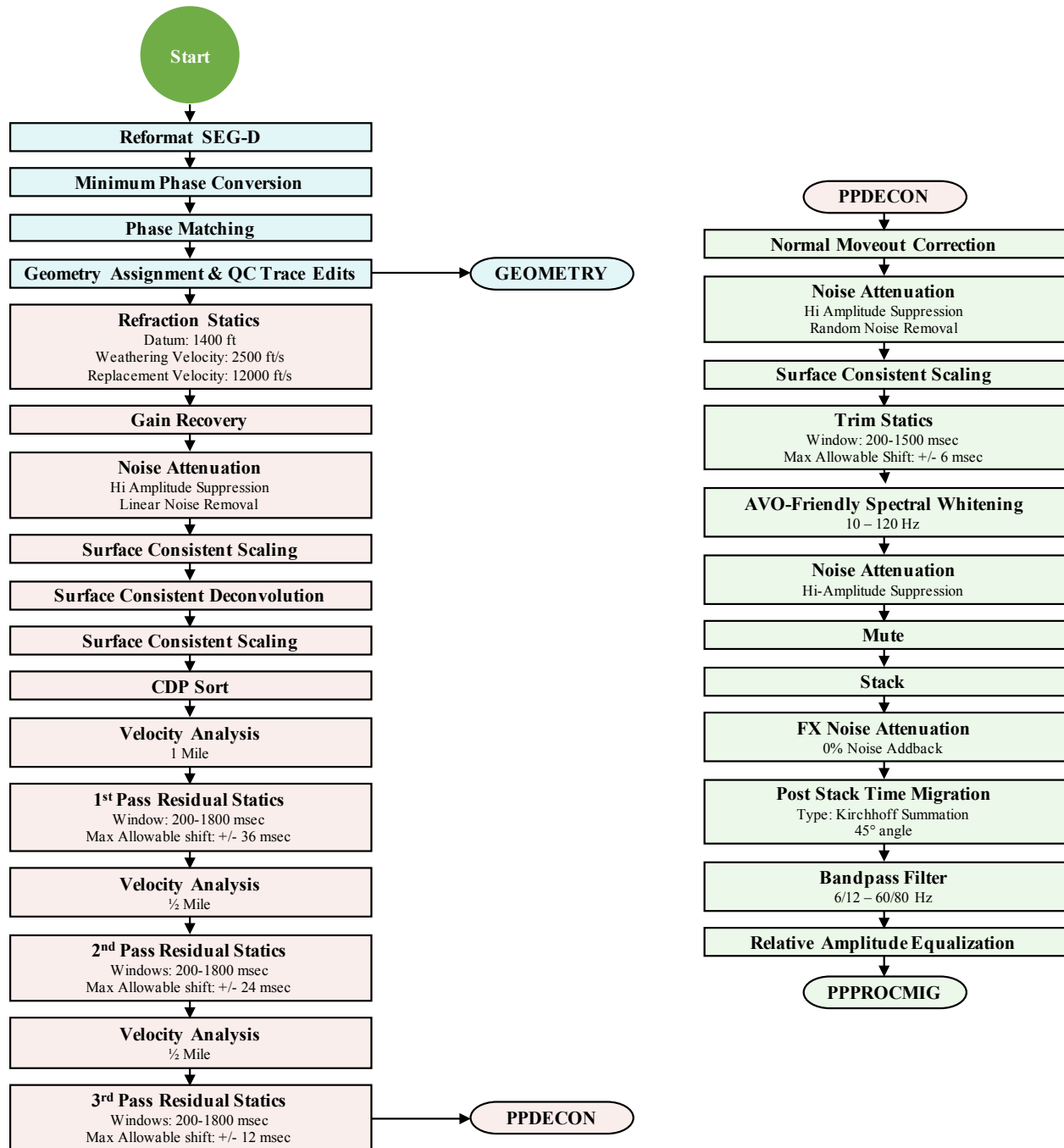


Figure 3.33: Arcis’ P-wave processing workflow for the Firestone 2D seismic dataset. Left: The output ‘GEOMETRY’ was the dataset used for FWI processing, and the output ‘PPDECON’ (see Figure 3.32) was the dataset used for migration work. Right: Arcis’ workflow output ‘PPPROC MIG’ is its final post-stack migration image, a helpful point of comparison for my work.

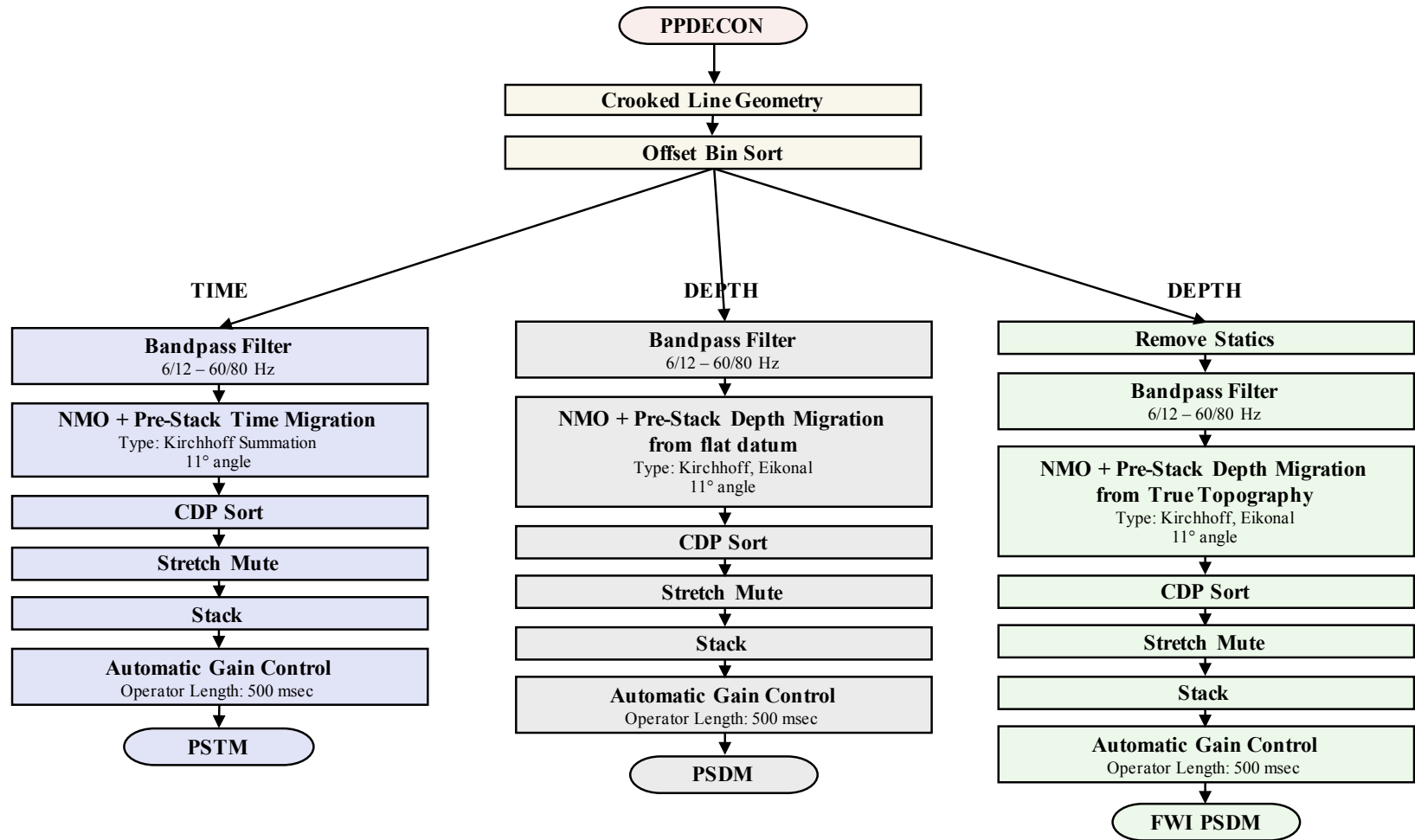


Figure 3.34: My processing workflows for time and depth, beginning from the ‘PPDECON’ data from Arcis’ processing (Figure 3.33). The three outputs of my processing are a pre-stack time migration ‘PSTM’ using Arcis’ NMO velocity model, a pre-stack depth migration ‘PSDM’ using a depth (and interval) converted model from Arcis’ NMO model, and a pre-stack depth migration from topography ‘FWI PSDM’ using a combination of my previous near-surface FWI work and the Arcis depth-interval model.

3.3.2 Geometry

One of the first steps in any seismic processing sequence is to assign the correct geometry to the data. I chose to assign a crooked line geometry for accuracy purposes and to replicate the geometry assigned in Arcis' processing as closely as possible. Figures 3.35 and 3.36 show the shot and receiver midpoints and the assigned 1908 common midpoint (CMP) bins. The fold of traces per CMP bin is about 115 (Figure 3.37).

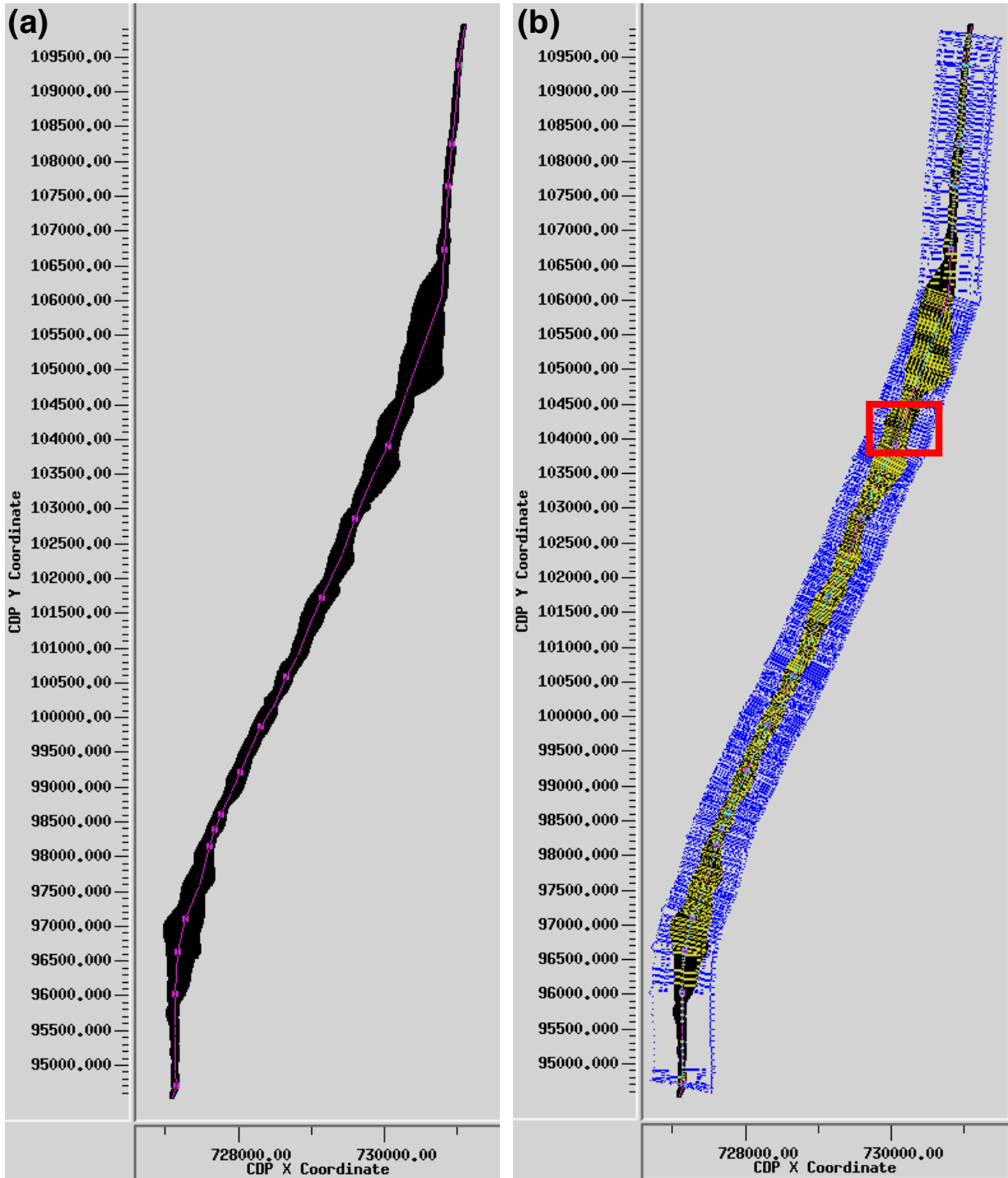


Figure 3.35: Crooked line geometry setup in ProMAX. (a) The shot and receiver midpoints are displayed in black. The pink line was picked to bin common mid points (CMPs). (b) 1908 CMP bins (blue boxes) cover the shot and receiver midpoints. The red rectangular box is a zoomed in portion and is shown in Figure 3.36.

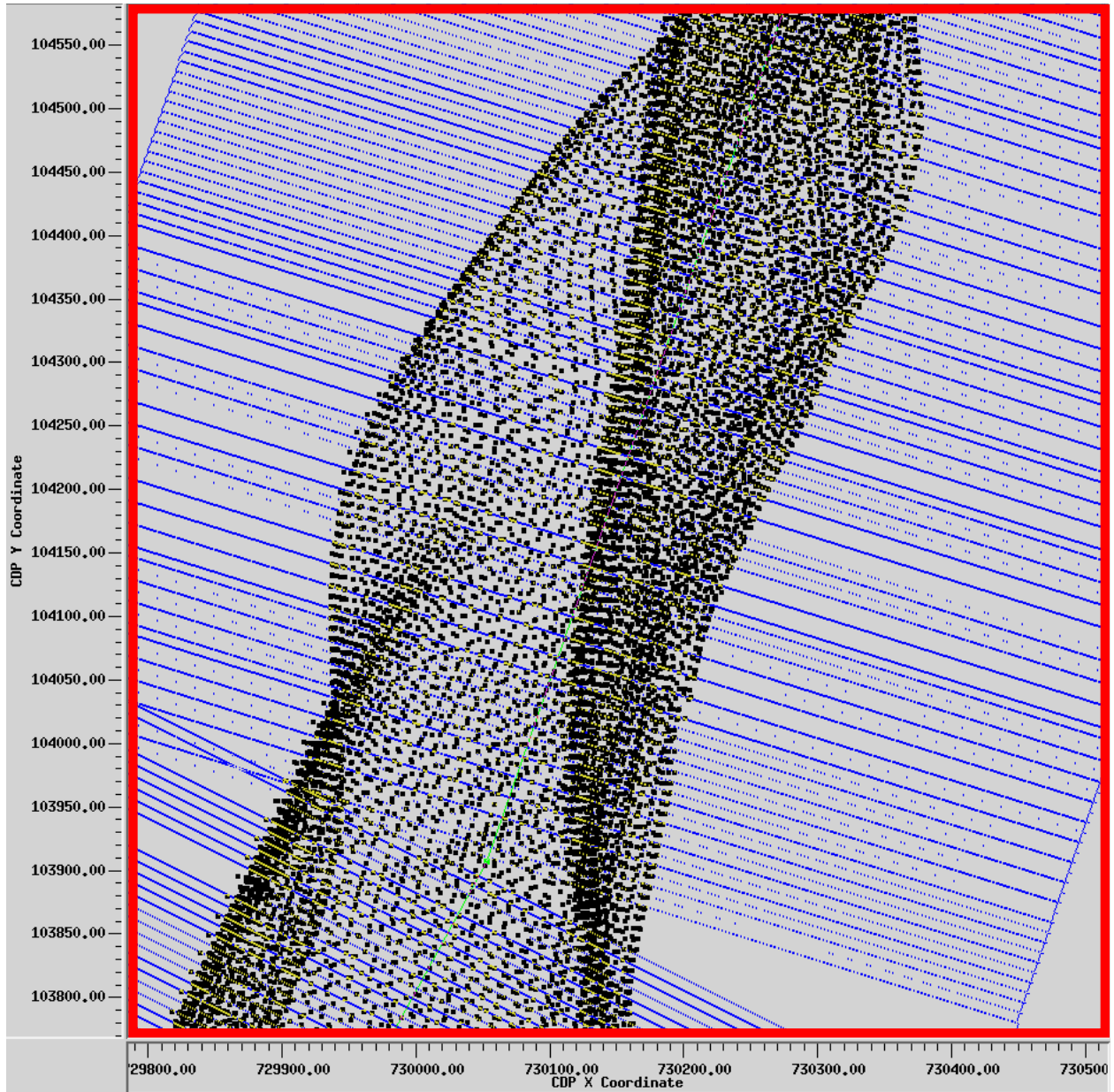


Figure 3.36: A zoomed in portion of Figure 3.35b, showing the shot-receiver midpoints (black) and CMP bins (blue boxes).

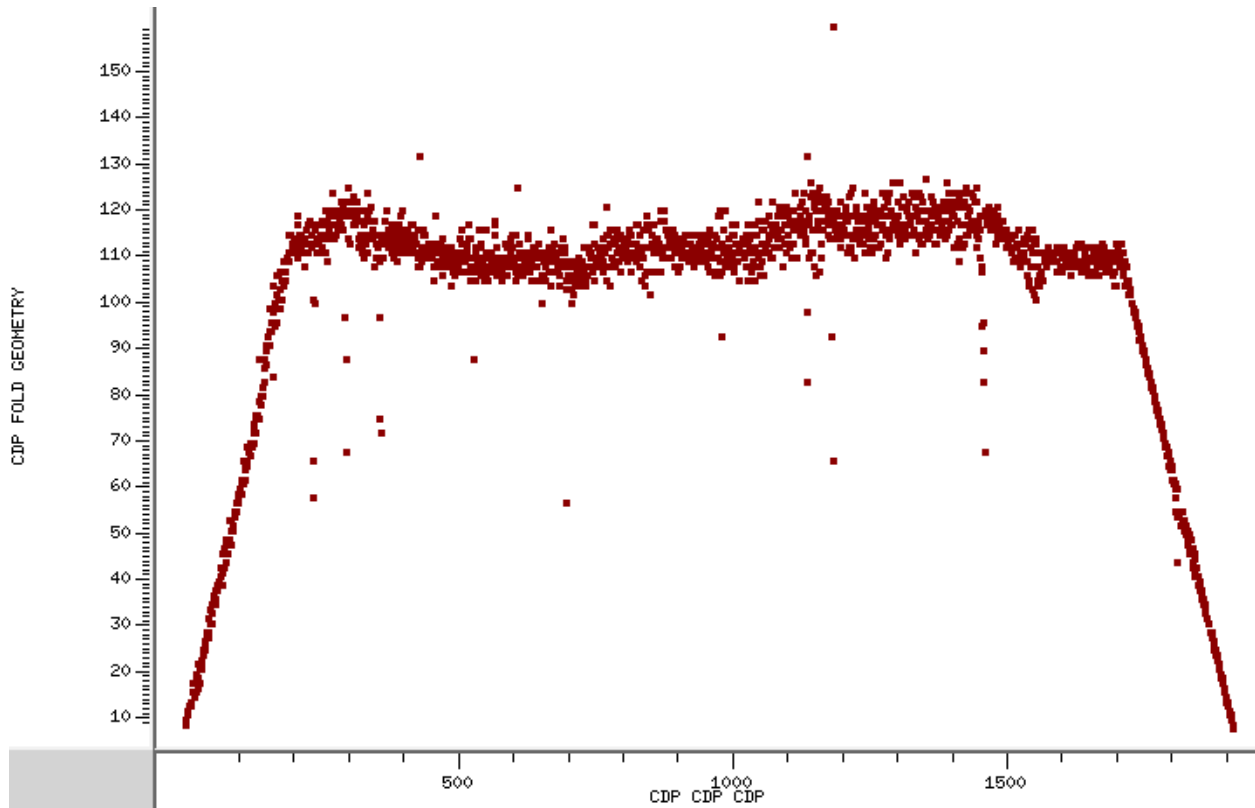


Figure 3.37: Fold chart shows the number of traces in each CMP bin.

3.3.3 Time Processing

I present the results of Arcis' post-stack time processing, and my pre-stack time processing. The goal of my processing in time was to as best as possible replicate the processing work of Arcis, before moving to depth processing, which is usually more challenging. Arcis performed three rounds of careful velocity analysis work to finalize a root mean square (RMS) velocity model in time. Figure 3.38 presents (a) the data after sorting into CMPs and (b) the CMPs after NMO and pre-stack time migration. Clear reflectors (hyperbolic shapes) are visible in the raw CMPs, which is a necessary precursor to a high-quality image. Figure 3.39 shows Arcis' post-stack time migration 'PPPROC MIG' stack and my PSTM stack. Arcis' very careful processing produced clear reflectors throughout the image.

My goal in time processing was to obtain a comparable image in time to Arcis' image before moving onto depth processing. I used the same Arcis RMS velocity model during migration. I used 1.5 km of offsets in migration, and applied a CMP stretch mute before stacking. The reflectors appear around the same times, indicating that my result was sufficiently robust as compared to the image from Arcis. In the time range of 0-300 ms, the reflectors I imaged are not as coherent as those in those imaged in the Arcis result. Also, there appear to be around 6 vertical bands

of migration smiles which are present in my result, indicating that some CMPs were improperly migrated. Although these smiles degrade the image slightly, the image is still of high-quality. One benefit of my processed result (PSTM) is that there is an increase in lateral resolution over the Arcis result (PPPROC MIG).

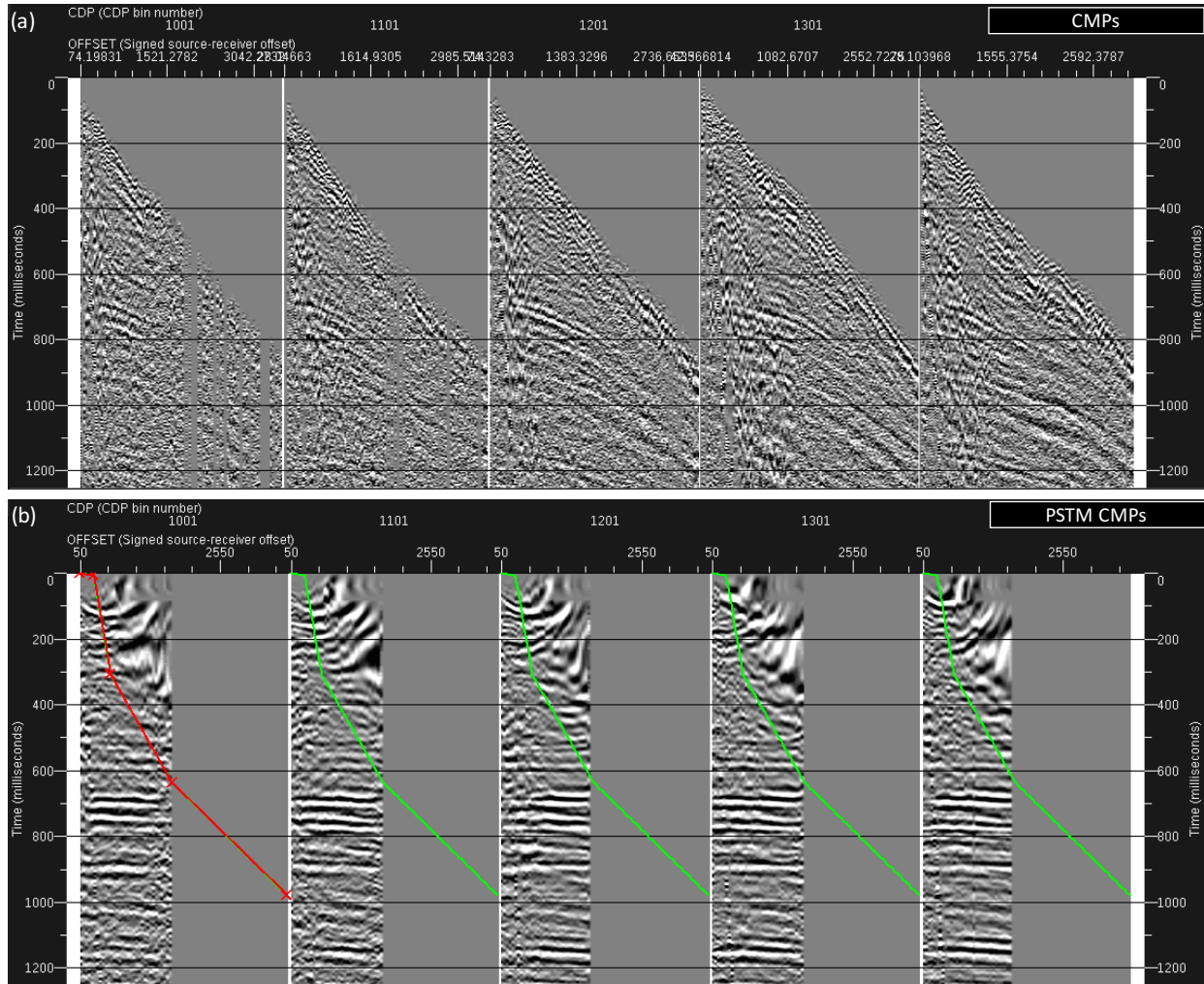


Figure 3.38: (a) The data have been sorted into CMPs with previous processing applied by Arcis. (b) The same CMPs after normal move-out (NMO) and migration were applied. The red and green lines are stretch mutes: the data above the lines were muted just prior to stacking. The offsets were limited from the original maximum of 3.5 km to 1.5 km. The previously hyperbolic reflectors now mostly appear as flat, an indicator of a high-quality RMS velocity model.

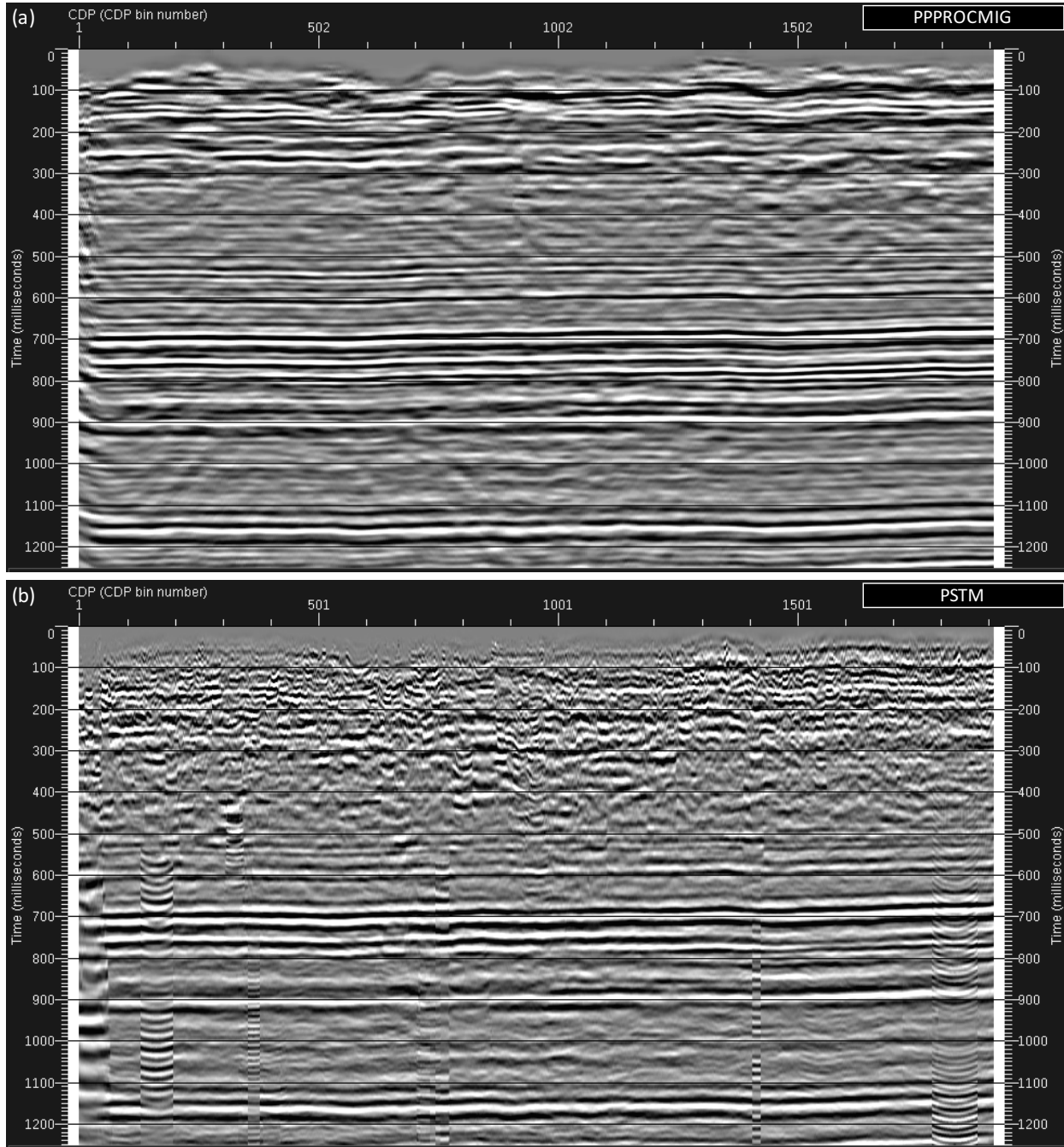


Figure 3.39: (a) Arcis' post-stack time migration result is a well-resolved image showing clear reflectors. (b) My pre-stack time migration result shows more lateral resolution, but some of the clarity of the first 0 - 300 ms was lost. The time axes represent two-way travel time. The 1908 CMP bins comprise the 16 km seismic line.

3.3.4 Depth Processing

This section presents the depth processing work I completed. Using FWI results in the near-surface may provide some benefit in determining the shape of reflectors over purely using an interval- and depth- converted RMS velocity model. Also, by using the results from a topographically accurate model (from FWI), there is the potential of skipping some of the statics calculations typically needed to properly prepare the data for migration. To get a velocity model in depth, I converted Arcis' RMS model to interval velocity using Dix conversion, followed by a conversion to depth. The model was smoothed in preparation of pre-stack depth migration. The models before and after smoothing are displayed in Figure 3.40.

The velocity model obtained through FWI was only 0.66 km in depth, which meant that another model was required for a depth to 2.5 km. To obtain such a model, I stitched my FWI result with the depth-converted model from Arcis. The result and its smoothed version used in 'FWI PSDM' are shown in Figure 3.41. There are a few challenges with using such a setup. The near-surface FWI model was computed with a 2D straight-line geometry, while the Arcis RMS was determined with a crooked-line geometry. Another challenge is that the FWI model was computed from a varying topographic surface that followed the sources and receivers, and the Arcis model was computed from a flat datum. I use a Kirchhoff Eikonal migration algorithm for depth migration. This routine is not particularly optimized for shorter wavelength features (with slower velocities from FWI). I do smooth heavily in order to maintain higher velocities.

Even with these barriers, the use of the (smoothed) FWI model in the near-surface seems to somewhat improve the shape of some of the reflectors (stratigraphy) at greater depths (around 2 km), as the trends shown in FWI PSDM align more closely with the expected trends from the S-N cross-section in Figure 3.5 than the trends in the PSDM without FWI. For the PSDM without FWI, the statics from Arcis were applied to the data as the data were migrated from a flat datum. For the FWI PSDM, the statics were removed from the data as the data were migrated from the topographic surface. Figure 3.42 shows CMPs after NMO and migration were applied for both the PSDM and PSDM with near-surface FWI. The final stacked results are shown in Figure 3.43. In both cases, it is clear that the majority of the CMPs are sloping down and would require a slower velocity to be flat. The velocity model used for FWI PSDM was slightly slower in the near-surface than the model used for PSDM without FWI (see Figure 3.41 vs. 3.40), pushing some reflectors to a deeper (> 100 m) positions (longer two-way travel times).

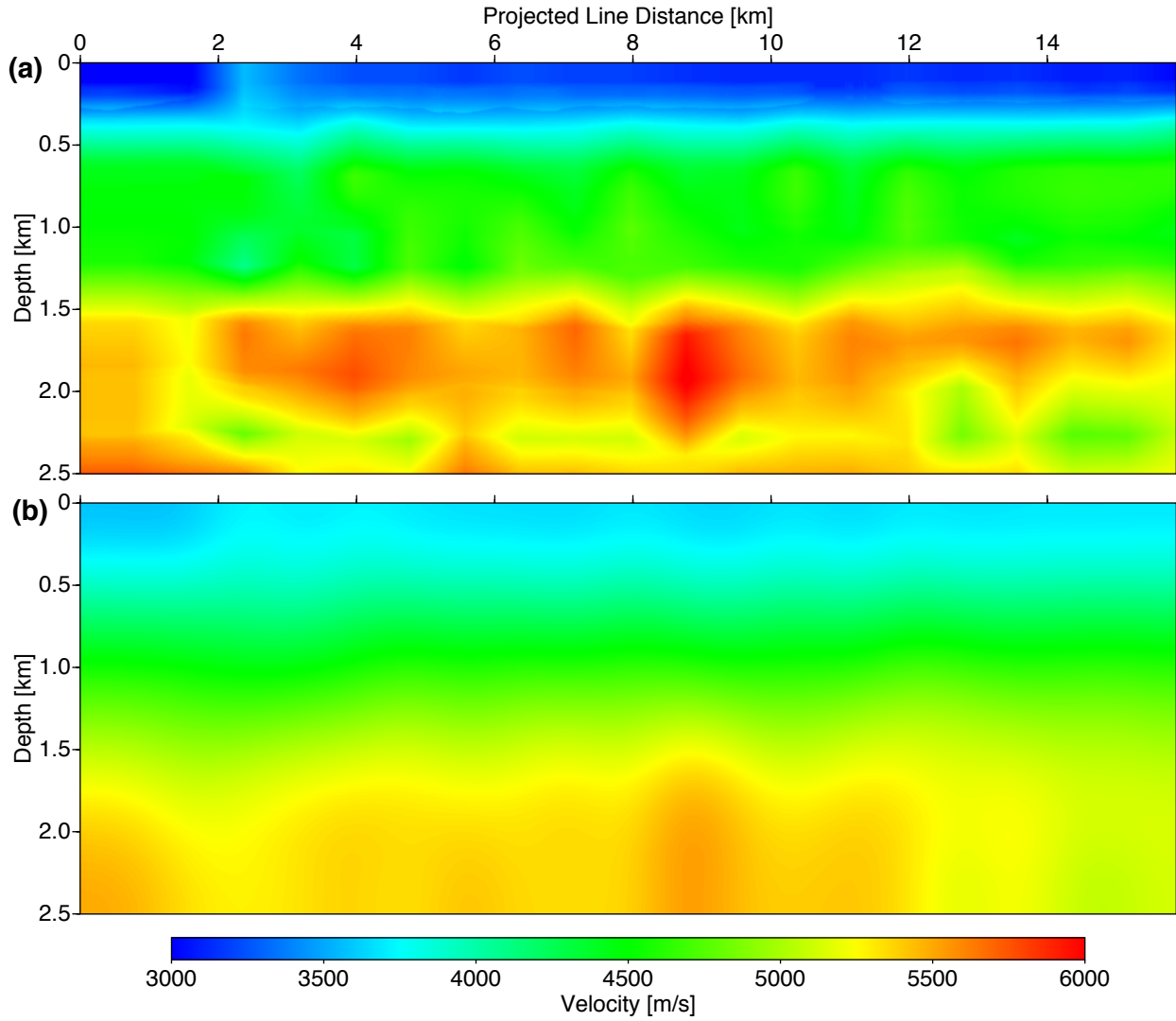


Figure 3.40: (a) Interval- and depth-converted RMS velocity model from Arcis. (b) Smoothed version used for migration 'PSDM'.

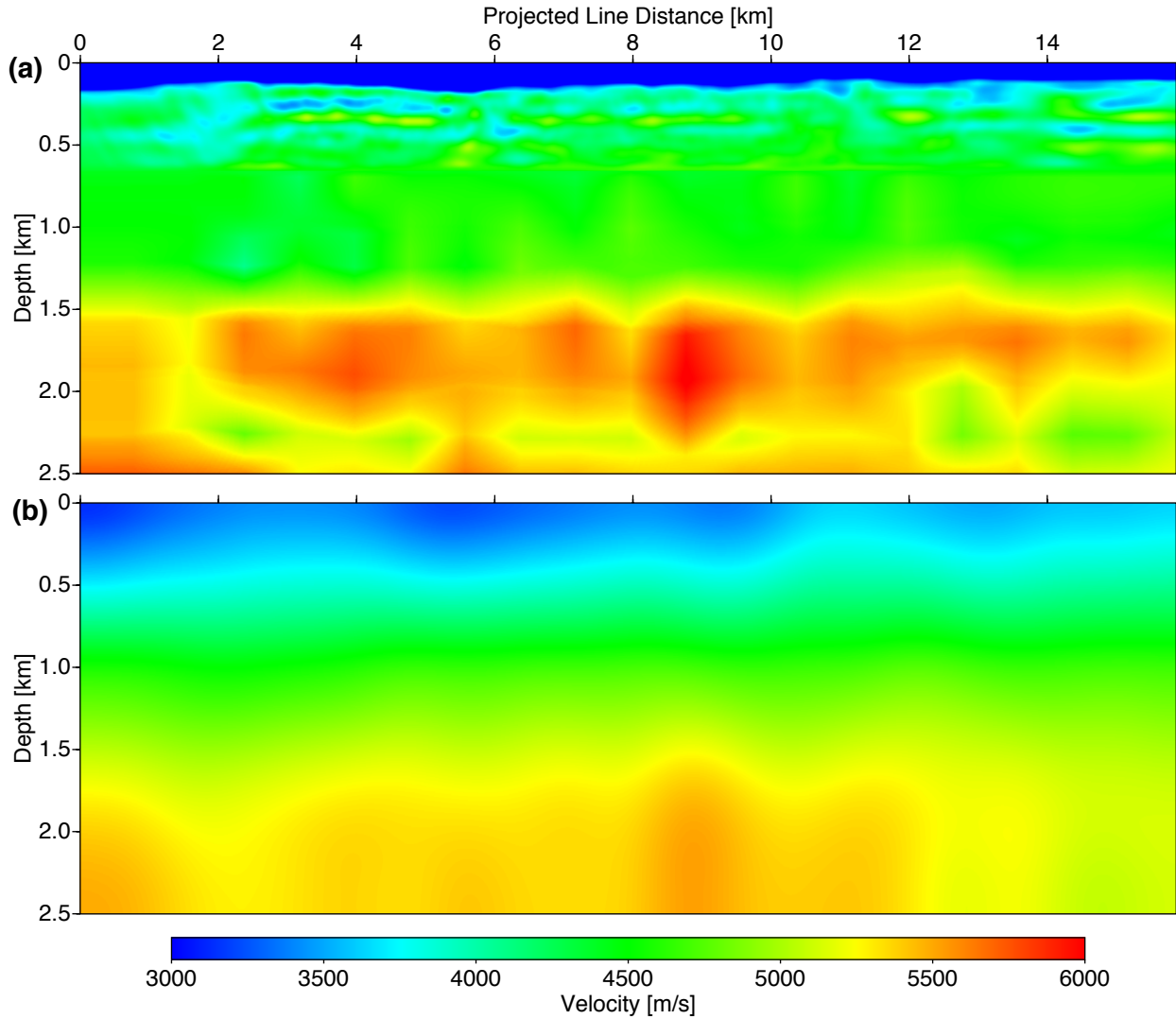


Figure 3.41: (a) A stitched velocity model of the FWI result in the near-surface (< 0.66 km) and the depth-converted Arcis model at greater depths. (b) Smoothed version used for migration 'FWI PSDM'. The velocities are much slower in the near-surface as compared to the depth-converted Arcis model in Figure 3.40.

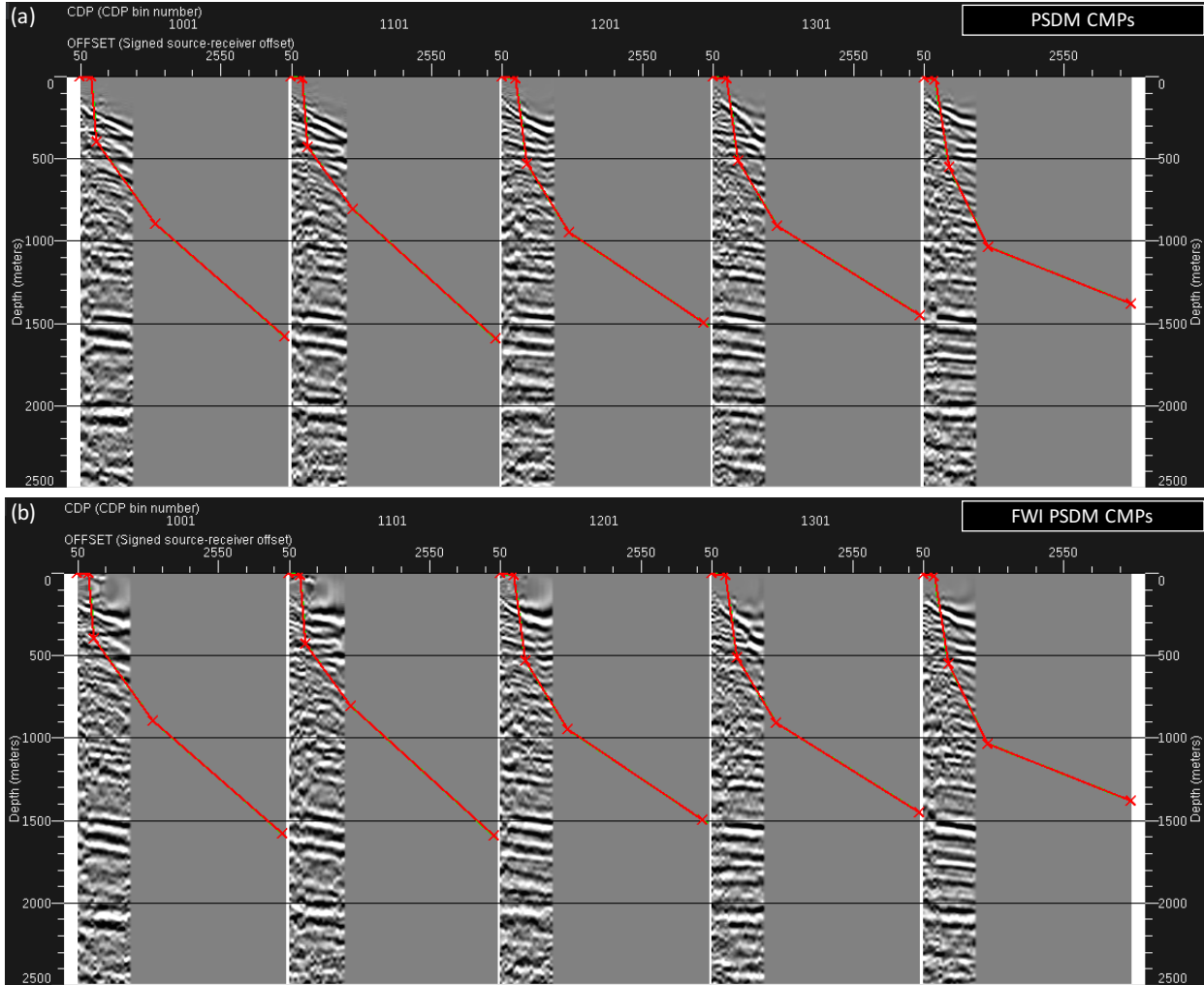


Figure 3.42: (a) CMPs after NMO correction and migration from a datum of 426.7 m above sea level, with statics applied, using the depth-converted Arcis velocity model. (b) CMPs after NMO correction and migration from topography using the stitched FWI-Arcis velocity model. The red lines are stretch mutes, applied only before final stacking.

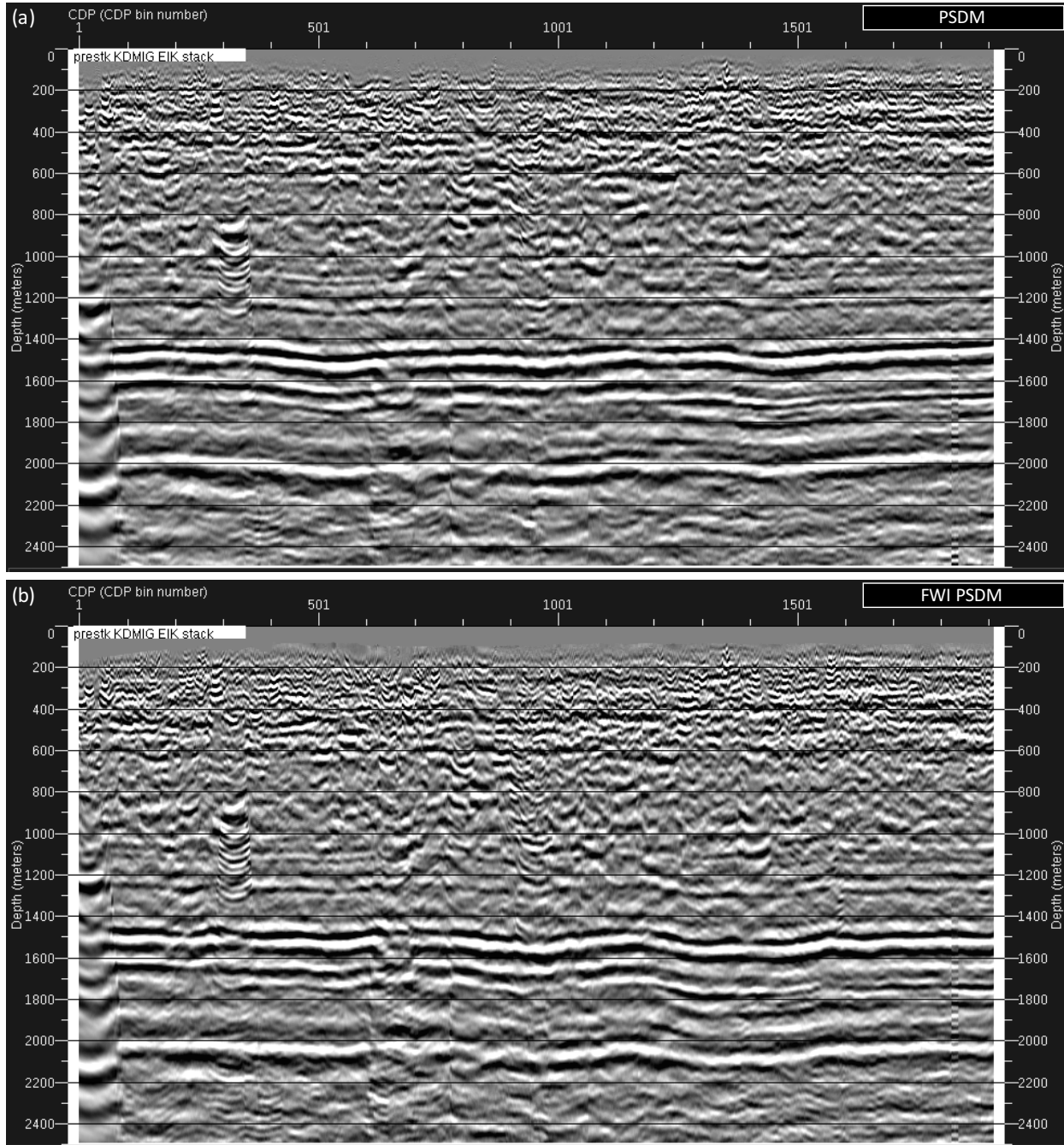


Figure 3.43: (a) Stacked image after pre-stack depth migration from a datum of 426.7 m above sea level, using a depth-converted RMS velocity model from Arcis. (b) Stacked image after pre-stack depth migration from topography, using the stitched FWI-Arcis model.

3.3.5 Interpretation

One of the first steps typically required in seismic interpretation is to generate a synthetic seismogram from well close to the line, and then tie it to the seismic image. A synthetic seismogram is

a single 1D trace generated by convolving the reflectivity (derived from density and sonic logs) with a wavelet (derived some seismic data). By placing the new synthetic 1D trace over a seismic migrated image, an interpreter can evaluate the quality of the seismic image at the well location by noting unity of impedance contrasts. As the two wells I acquired are some significant distance (1.5 km and 6 km) from the seismic line and the bandwidth of the seismic data is so limited, I chose not to create a synthetic seismogram. Moving forward, I cautiously move toward an interpretation, given the well information available.

The average resolution limit of the image is related to the wavelength,

$$\lambda = \frac{c_{avg}}{f_{dom}} = \frac{4000 \text{ m/s}}{25 \text{ Hz}}, \quad (3.2)$$

giving a resolvable wavelength of 160 m, where c_{avg} is the average velocity in the model and f_{dom} is the dominant frequency. Some of the observed formations thicknesses from the top-of-formation data, including the Big Injun sand, Berea sandstone, and Utica shale, are less than 160 m (Appendix B), meaning that their thicknesses are below the resolution limit of the image. However, given a change in impedance at a given top of a formation, a reflector should be visible. The CMPs in depth presented in Figure 3.42 show that a slower velocity is required throughout much of the model. The near-surface (< 0.66 km) portion of the model from FWI is much slower than the depth-converted Arcis model; however, there was no tomography completed in the deeper portions of the model. Using a slower velocity in the near-surface pushed down reflectors by approximately 150 m at depths greater than 1000 m. Without a well tie, I cautiously propose an interpretation of the reflectors on the final FWI PSDM, based on nearby well information. More work with well ties would be required before a well plan could be developed. Figure 3.44 shows the final FWI PSDM image overlaid with my interpretation.

Using the top-of-formation data from the Rose Reynolds well can potentially provide a benchmark for labeling the PSDM image. Figure 3.45 shows the Rose Reynolds well data for the formations between depths of 1.2 km and 1.9 km. The formation labels Big Lime, Salina Dolomite, and Little Lime on the PSDM image are between 100 m and 200 m shallower than the formation tops on the well log. As previously noted, slower velocities would be needed to flatten the CMP gathers. It would not be unreasonable for these reflectors to shift by 100 - 200 m with a slower velocity model. The FWI in the near-surface to 0.66 km did provide uplift by moving the deeper reflectors (Big Lime, Salina dolomite, Little Lime, Utica shale) down toward a position closer to the expected positions from the S-N cross-section in Figure 3.5. In order to move these reflectors closer to their true depths, more extensive tomography work would be required on the 2.5 km velocity model. However, the fact that the reflectors moved in a favourable direction gives me confidence in my FWI work. Using the Utica shale reflector shape in the S-N cross-section (Figure

3.5) as a reference, I note that the FWI work provided some benefit in matching the overall shape of the Utica shale reflector over only using the depth-converted Arcis model.

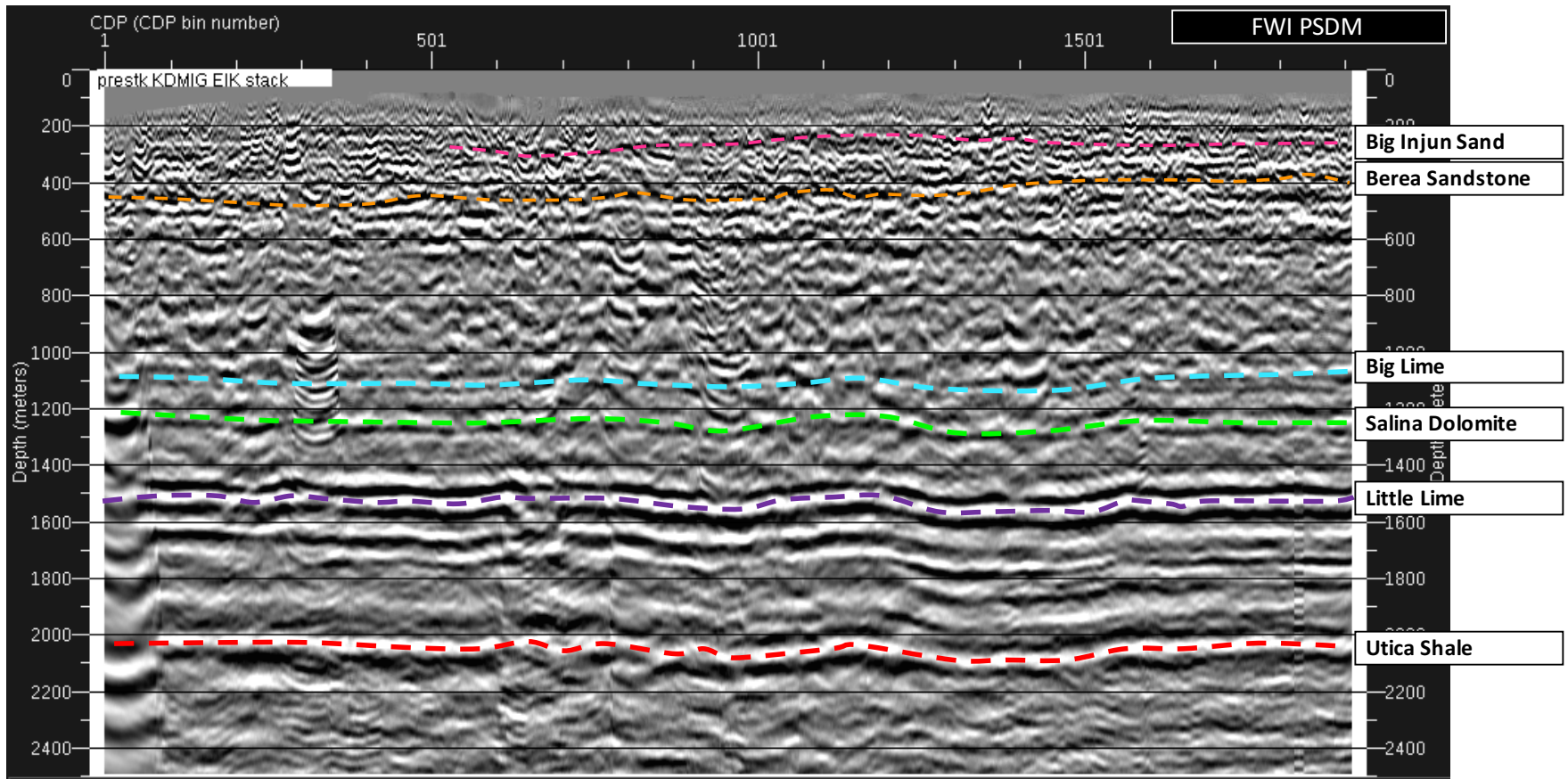


Figure 3.44: Preliminary interpretation of top-of-formations overlaid on final FWI PSDM image.

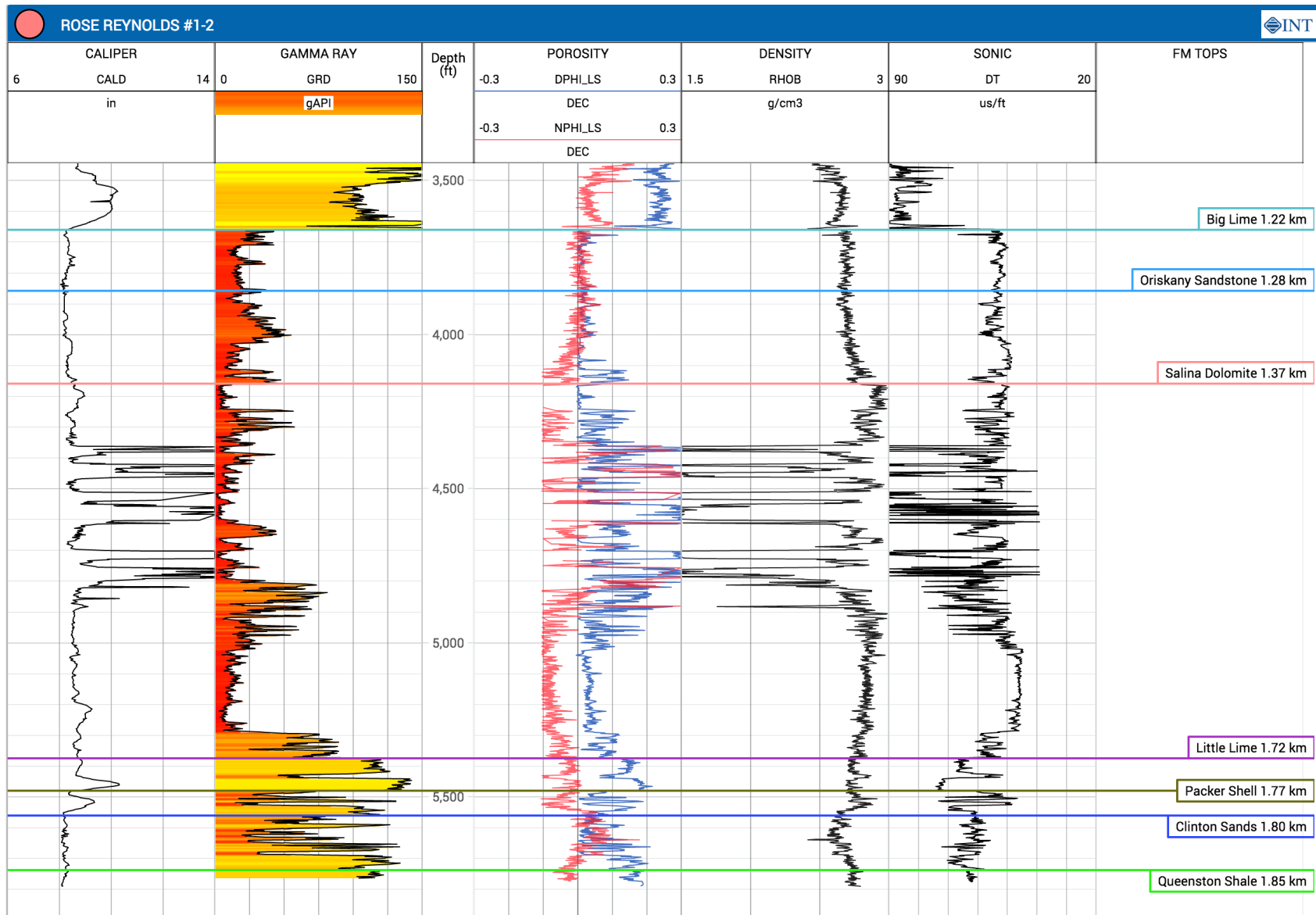


Figure 3.45: The bottom 1.2 - 1.9 km portion of the Rose Reynolds well log with formation tops labeled, located 1.5 km away from the projected survey line. The top-of-formation depths are on the right panel, referenced to the FWI velocity model datum (426.7 m above sea level).

Chapter 4

Conclusions and Future Directions

The full-waveform inversion (FWI) algorithm employed in this thesis was successful in recovering a high resolution near-surface velocity model down to a depth of 0.66 km on a crooked seismic line from eastern Ohio. The novelty of my work was mainly in resolving the near-surface geologic structures at a high-resolution of approximately 40 m. There were no visible small scale faulted features discernible on the final images, providing evidence for the first time of the absence of these structures in the near-surface. The use of FWI for land seismic data is rare due to the many difficulties in implementation; never before has there been a published FWI study in eastern Ohio. Beyond that, this study represents the first successful application of FWI with the new scaled-Sobolev preconditioner (SSP) to a field dataset.

The vibroseis seismic data were of high quality in general, but lacked useable frequencies below 12 Hz, making attempts at conventional approaches to FWI challenging. To mitigate these challenges, I applied the SSP, which allowed me to successfully recover low-wavenumber updates without very low frequencies, while also retaining high-wavenumber features. The fidelity of the final velocity model was validated by a number of measures, including an evaluation of the coherency of estimated source signatures, a comparison to sonic well log data, a qualitative comparison of the observed and forward modelled seismic data, and pre-stack depth processing. Two rock formations well known from the Ohio geology literature were identified on the final FWI velocity model: the Big Injun sand, and the Berea sandstone. The Berea sandstone and surrounding shales were identified as a lower velocity zone through FWI updates, a feature not usually resolvable using other methods.

There were several limitations of the study that should be stated. The wave equation is the forward modelling step of FWI and it governs the physics of the problem. One limitation is the assumption of an isotropic, acoustic, and 2D wave equation. A wave that travels through an isotropic medium has the same velocity in all orientations, but we know that in geology this is not always the case (Tsvankin, 2012). We saw that the velocities below 0.5 km in the FWI model did not match

well with the sonic log, which could be due to anisotropy. The assumption of an acoustic wave equation means that elastic effects are not taken into account, including S-waves and PS converted waves. The absence of elastic effects in our simulations implies that no P-wave velocity model emerging from our inversions can completely describe subsurface wave propagation. In this study, there were two horizontal components that favour S-waves that were not used. The assumption of a 2D medium instead of a 3D medium meant that the coordinates of sources and receivers had to be projected onto a 2D plane from a 3D geometry, resulting in new source-to-receiver offset location errors. The data were discarded where the projected offset errors were greater than 3%, which prevented coverage (and inhibited updates) in some regions. The conventional reflection processing that was completed was limited due to time constraints. I thus place lower confidence in those results. However, the seismic data were of high quality for vibroseis data, and FWI still produced a robust model of the subsurface with these data.

A 3D FWI workflow would accurately account for the crooked geometry of the line, without having to deal with geometry approximation errors by using a 2D projection. Other cases similar to this study also reveal that FWI in 2.5D may be a good compromise, as 2.5D can account for 3D geometry, but with some of the robustness of the 2D workflow (eg., [Smithyman and Clowes, 2013](#)). Another solution would be to use the 2D projection but apply a statics correction on the seismic data, so that no data would need to be discarded. Subsequent work on the data could also include elastic and anisotropic FWI, potentially making use of the two horizontal components from the survey. Using elastic FWI would allow the inclusion of S-waves arrivals, and PS converted arrivals, which could lead to a better result. The inclusion of anisotropy in the wave equation could help mitigate the problem of media with different preferred velocity orientations. The results presented here are encouraging for future applications of FWI with SSP to other field datasets. The results from pre-stack depth migration reveal that more tomography and migration work could be completed on the deeper (2.5 km) velocity model to improve the location and focusing of the Utica shale reflector.

Clean reflections in the vibroseis data make the use of reflection FWI (RFWI) a possibility for future work. Reflections respond primarily to high-wavenumber content, and it is difficult to converge on the global minimum solution in RFWI as compared to refraction data FWI. A potentially promising workflow could weave the efforts of refraction FWI in the near-surface and reflection FWI for greater depths together. The reflection FWI implementation by [Yao and Wu \(2017\)](#) combines reverse time-migration (RTM) and reflection FWI to produce background updates from reflections. [Ma and Hale \(2013\)](#) use another approach, combining a new wave-equation traveltimes inversion (WERTI) for low-wavenumber updates and FWI for high-wavenumber updates. The data in this thesis were acquired for reflections over short maximum offsets rather than refractions, making them a good potential candidate to test RFWI.

Bibliography

- Adamczyk, A., M. Malinowski, and A. Malehmir, 2014, High-resolution near-surface velocity model building using full-waveform inversion - a case study from southwest Sweden: *Geophysical Journal International*, **197**(3), 1693–1704, doi: 10.1093/gji/ggu070.
- Aki, K., and P. G. Richards, 1980, *Quantitative Seismology: Theory and Methods*: W. H. Freeman & Co.
- Bednar, J. B., C. Shin, and S. Pyun, 2007, Comparison of waveform inversion, part 2: phase approach: *Geophysical Prospecting*, **55**(4), 465–475, doi: 10.1111/j.1365-2478.2007.00618.x.
- Berenger, J.-P., 1994, A perfectly matched layer for the absorption of electromagnetic waves: *Journal of Computational Physics*, **114**(2), 185–200, doi: 10.1006/jcph.1994.1159.
- Birdus, S., A. Artemov, L. Li, and L. Vincent, 2015, Making anisotropy in seismic imaging models conformal with geology and velocity: application to standard tomographic and higher resolution FWI velocity modeling: 85th Annual Meeting, SEG, Expanded Abstracts, 557–561, doi: 10.1190/segam2015-5831251.1.
- Bleibinhaus, F., J. A. Hole, T. Ryberg, and G. S. Fuis, 2007, Structure of the California Coast Ranges and San Andreas Fault at SAFOD from seismic waveform inversion and reflection imaging: *Journal of Geophysical Research: Solid Earth*, **112**(B6), 1–15, doi: 10.1029/2006JB004611.
- Brenders, A. J., 2011, *Strategies for Waveform Tomography of Long-Offset, 2-D Exploration Seismic Data*: Ph.d. thesis, University of Western Ontario.
- Brenders, A. J., and R. G. Pratt, 2007, Full waveform tomography for lithospheric imaging: results from a blind test in a realistic crustal model: *Geophysical Journal International*, **168**(1), 133–151, doi: 10.1111/j.1365-246X.2006.03156.x.
- Brent, R. P., 1973, *Algorithms for minimization without derivatives*: Dover Publications.
- Brossier, R., 2011, Two-dimensional frequency-domain visco-elastic full waveform inversion: Parallel algorithms, optimization and performance: *Computers and Geosciences*, **37**(4), 444–455, doi: 10.1016/j.cageo.2010.09.013.
- Bunks, C., F. M. Saleck, S. Zaleski, and G. Chavent, 1995, Multiscale seismic waveform inversion: *Geophysics*, **60**(5), 1457–1473, doi: 10.1190/1.1443880.
- Butzer, S., A. Kurzmann, and T. Bohlen, 2013, 3D elastic full-waveform inversion of small-scale heterogeneities in transmission geometry: *Geophysical Prospecting*, **61**(6), 1238–1251, doi: 10.1111/1365-2478.12065.
- Castellanos, C., V. Etienne, G. Hu, S. Operto, R. Brossier, and J. Virieux, 2011, Algorithmic and methodological developments towards full waveform inversion in 3D elastic media: Presented at the 81st Annual International Meeting, SEG, Expanded Abstracts, doi: 10.1190/1.3627774.
- Chavent, G., 1974, *Identification of functional parameters in partial differential equations*: Joint

BIBLIOGRAPHY

- Automatic Control Conference, 155–156.
- Claerbout, J. F., 1971, Toward a unified theory of reflector mapping: *Geophysics*, **36**(3), 467–481, doi: 10.1190/1.1440185.
- , 1976, *Fundamentals of Geophysical Data Processing: With Applications to Petroleum Prospecting*: McGraw Hill.
- Consolvo, B. P., M. A. H. Zuberi, R. G. Pratt, and P. W. Cary, 2017, FWI with Scaled-Sobolev Preconditioning Applied to Short-offset Vibroseis Field Data: Presented at the 79th Annual International Conference and Exhibition, EAGE, Extended Abstracts, doi: 10.3997/2214-4609.201701164.
- Fedorov, A. F. I., 1968, *Theory of Elastic Waves in Crystals*: Plenum US.
- Gardner, G., W. Gardner, L., and A. Gregory, 1974, Formation velocity and density—The diagnostic basics for stratigraphic traps: *Geophysics*, **39**(6), 770–780, doi: 10.1190/1.1440465.
- George, A., and J. Lui, 1981, *Computer solutions of large positive definite systems*: Prentice-Hall Inc.
- Grandjean, G., 2006, Imaging subsurface objects by seismic P-wave tomography: Numerical and experimental validations: *Near Surface Geophysics*, **4**(5), 279–287, doi: 10.3997/1873-0604.2005051.
- Hadden, S., and R. Pratt, 2017, Full Waveform Inversion of Crosshole Data in Tilted Transversely Isotropic Media: Presented at the 79th Annual International Conference and Exhibition, EAGE, Extended Abstracts, doi: 10.3997/2214-4609.201700793.
- Helbig, K., 1994, *Foundations of Anisotropy for Exploration Seismics*: Pergamon.
- Helbig, K., and M. Schoenberg, 1987, Anomalous polarization of elastic waves in transversely isotropic media: *The Journal of the Acoustical Society of America*, **81**(5), 1235, doi: 10.1121/1.394527.
- Hicks, G. J., 2002, Arbitrary source and receiver positioning in finite-difference schemes using Kaiser windowed sinc functions: *Geophysics*, **67**(1), 156–166, doi: 10.1190/1.1451454.
- Hildenbrand, T. G., R. P. Kucks, and R. W. Johnson, 1981, Aeromagnetic map of east-central United States: U.S. Geological Survey Geophysical Investigations Map GP-948.
- Hole, J. A., and C. A. Zelt, 1995, 3D finite-difference reflection traveltimes: *Geophysical Journal International*, **121**(2), 427–434, doi: 10.1111/j.1365-246X.1995.tb05723.x.
- Hornby, B. E., J. M. Howie, and D. W. Ince, 2003, Anisotropy correction for deviated-well sonic logs: Application to seismic well tie: *Geophysics*, **68**(2), 464, doi: 10.1190/1.1567214.
- Jo, C.-H., C. Shin, and J. H. Suh, 1996, An optimal 9-point, finite-difference, frequency-space, 2-D scalar wave extrapolator: *Geophysics*, **61**(2), 529, doi: 10.1190/1.1443979.
- Kamei, R., T. Miyoshi, R. G. Pratt, M. Takanashi, and S. Masaya, 2015, Application of waveform tomography to a crooked-line 2D land seismic data set: *Geophysics*, **80**(5), B115–B129, doi: 10.1190/geo2014-0537.1.
- Kamei, R., and R. G. Pratt, 2013, Inversion strategies for visco-acoustic waveform inversion: *Geophysical Journal International*, **194**(2), 859–884, doi: 10.1093/gji/ggt109.
- Kamei, R., R. G. Pratt, and W. Ontario, 2012, Wide-band multifrequency waveform inversion in the Laplace-Fourier domain: Presented at the 82nd Annual International Meeting, SEG, Expanded Abstracts, doi: 10.1190/segam2012-1588.1.
- Kamei, R., R. G. Pratt, and T. Tsuji, 2013, On acoustic waveform tomography of wide-angle OBS data—strategies for pre-conditioning and inversion: *Geophysical Journal International*, **194**(2), 1250–1280, doi: 10.1093/gji/ggt165.

BIBLIOGRAPHY

- , 2014, Misfit functionals in Laplace-Fourier domain waveform inversion, with application to wide-angle ocean bottom seismograph data: *Geophysical Prospecting*, **62**(5), 1054–1074, doi: 10.1111/1365-2478.12127.
- Kirschbaum, M. A., C. J. Schenk, T. A. Cook, R. T. Ryder, R. R. Charpentier, T. R. Klett, S. B. Gaswirth, M. E. Tennyson, and K. J. Whidden, 2012, Assessment of Undiscovered Oil and Gas resources of the Ordovician Utica Shale of the Appalachian Basin Province, 2012: Technical report, US Geological Survey.
- Lailly, P., 1983, The seismic inverse problem as a sequence of before stack migrations: Bednar, J. B., Redner, R., Robinson, E., and Weglein, A., Eds., *Conference on Inverse Scattering: Theory and Application*, Society for Industrial and Applied Mathematics, Expanded Abstracts, 206–220.
- Lambaré, G., R. Plessix, and J. Virieux, 2017, Workshop 9: Velocity Model Building - Full Wave vs Kinematic Approaches: Presented at the 79th Annual International Conference and Exhibition, EAGE.
- Lewis, W., D. Amazonas, D. Vigh, and R. Coates, 2014, Geologically constrained full-waveform inversion using an anisotropic diffusion based regularization scheme : application to a 3D offshore Brazil dataset: 84th Annual International Meeting, SEG, Expanded Abstracts, 1083–1088, doi: 10.1190/segam2014-1174.1.
- Løseth, H., M. Gading, and L. Wensaas, 2009, Hydrocarbon leakage interpreted on seismic data: *Marine and Petroleum Geology*, **26**(7), 1304–1319, doi: 10.1016/j.marpetgeo.2008.09.008.
- Lu, R., S. Lazaratos, S. Hughes, and D. Leslie, 2016, Revealing overburden and reservoir complexity with high-resolution FWI: 86th Annual International Meeting, SEG, Expanded Abstracts, 1242–1246, doi: 10.1190/segam2016-13872562.1.
- Lu, R., S. Lazaratos, K. Wang, Y. Cha, I. Chikichev, and R. Prosser, 2013, High-resolution Elastic FWI for Reservoir Characterization: Presented at the 75th Annual International Conference and Exhibition incorporating SPE EUROPEC 2013, EAGE, Extended Abstracts, doi: 10.3997/2214-4609.20130113.
- Ma, Y., and D. Hale, 2013, Wave-equation reflection traveltime inversion with dynamic warping and full-waveform inversion: *Geophysics*, **78**(6), R223–R233, doi: 10.1190/geo2013-0004.1.
- Malinowski, M., and S. Operto, 2008, Quantitative imaging of the Permo-Mesozoic complex and its basement by frequency domain waveform tomography of wide-aperture seismic data from the Polish Basin: *Geophysical Prospecting*, **56**(6), 805–825, doi: 10.1111/j.1365-2478.2007.00680.x.
- Malinowski, M., S. Operto, and A. Ribodetti, 2011, High-resolution seismic attenuation imaging from wide-aperture onshore data by visco-acoustic frequency-domain full-waveform inversion: *Geophysical Journal International*, **186**(3), 1179–1204, doi: 10.1111/j.1365-246X.2011.05098.x.
- Mao, J., R.-S. Wu, and B. Wang, 2012, Multiscale full waveform inversion using GPU: Presented at the 82nd Annual International Meeting, SEG, Expanded Abstracts, doi: 10.1190/segam2012-0575.1.
- McCord, W. R., and W. E. Eckard, 1963, Lithology and Reservoir Properties of the Big Lime, Keener, Big Injun, Weir, and Berea Horizons, Spruce Creek Oilfield, Ritchie County, W. VA: Technical report, US Department of the Interior, Bureau of Mines, Washington.
- Mora, P., 1987, Nonlinear two-dimensional elastic inversion of multioffset seismic data: *Geophysics*, **52**(9), 1211–1228, doi: 10.1190/1.1442384.

BIBLIOGRAPHY

- Moser, T. J., 1991, Shortest path calculation of seismic rays: *Geophysics*, **56**(1), 59–67, doi: 10.1190/1.1442958.
- Mothi, S., H. Bi, and A. Yang, 2012, Benefits of FWI in Prestack Depth Imaging of Onshore Data: a Gulf Coast example: Presented at the 82nd Annual International Meeting, SEG, Expanded Abstracts, doi: 10.1190/segam2012-1486.1.
- Nicholson, S. W., C. L. Dicken, J. D. Horton, K. A. Labay, M. P. Foose, and J. A. L. Mueller, 2005, Preliminary integrated geologic map databases for the United States: Kentucky, Ohio, Tennessee, and West Virginia: Technical report.
- Nocedal, J., and S. J. Wright, 1999, *Numerical Optimization*: Springer-Verlag New York Inc.
- Nolen-Hoeksema, R., 2015, Elements of Hydraulic Fracturing: *Oilfield Review*, **25**(2), 51–52.
- Nye, J. F., 1957, *Physical Properties of Crystals: Their Representation by Tensors and Matrices*: Oxford University Press.
- ODNR Oil and Gas Resources Management, 2016, Ohio Oil & Gas Well Locator, <http://oilandgas.ohiodnr.gov/well-information/oil-gas-well-locator>, accessed 1 January 2017.
- Ohio Division of Geological Survey, 2006, Geologic map and cross section of Ohio: Ohio Department of Natural Resources, Division of Geological Survey, page-size map, 1 p., scale 1:2,000,000.
- , 2011, Generalized geology and profile of a Utica Shale well prototype in east central Ohio: Ohio Department of Natural Resources, Division of Geological Survey, one sheet.
- Operto, S., J. Virieux, J. X. Dessa, and G. Pascal, 2006, Crustal seismic imaging from multi-fold ocean bottom seismometer data by frequency domain full waveform tomography: Application to the eastern Nankai trough: *Journal of Geophysical Research*, **111**(9), 1–33, doi: 10.1029/2005JB003835.
- Plessix, R. E., 2006, A review of the adjoint-state method for computing the gradient of a functional with geophysical applications: *Geophysical Journal International*, **167**(2), 495–503, doi: 10.1111/j.1365-246X.2006.02978.x.
- Plessix, R. E., G. Baeten, J. W. D. Maag, F. ten Kroode, and Z. Rujie, 2012, Full waveform inversion and distance separated simultaneous sweeping: a study with a land seismic data set: *Geophysical Prospecting*, **60**(4), 733–747, doi: 10.1111/j.1365-2478.2011.01036.x.
- Plessix, R. È., and C. Perkins, 2010, Full waveform inversion of a deep water ocean bottom seismometer dataset: *First Break*, **28**(4), 71–78, doi: 10.3997/1365-2397.2010013.
- Polak, E., and G. Ribière, 1969, Note sur la convergence de méthodes de directions conjuguées: *Revue française d’informatique et de recherche opérationnelle, série rouge*, **3**(1), 35–43.
- Pratt, R., 1999, Seismic waveform inversion in the frequency domain, Part 1: Theory and verification in a physical scale model: *Geophysics*, **64**(3), 888–901, doi: 10.1190/1.1444597.
- Pratt, R. G., 1989, Wave equation methods in cross-hole seismic imaging: Ph.d. thesis, Imperial College, London.
- Pratt, R. G., C. Shin, and G. J. Hicks, 1998, Gauss-Newton and full Newton methods in frequency-space seismic waveform inversion: *Geophysical Journal International*, **133**(2), 341–362, doi: 10.1046/j.1365-246X.1998.00498.x.
- Pratt, R. G., and R. M. Shipp, 1999, Seismic waveform inversion in the frequency domain, Part 2: Fault delineation in sediments using crosshole data: *Geophysics*, **64**(3), 902–914, doi: 10.1190/1.1444598.
- Pratt, R. G., and M. H. Worthington, 1990, Inverse Theory Applied To Multi-Source Cross-Hole Tomography. Part 1: Acoustic Wave-Equation Method: *Geophysical Prospecting*, **38**(3), 287–

BIBLIOGRAPHY

- 310, doi: 10.1111/j.1365-2478.1990.tb01846.x.
- Prieux, V., R. Brossier, Y. Gholami, S. Operto, J. Virieux, O. I. Barkved, and J. H. Kommedal, 2011, On the footprint of anisotropy on isotropic full waveform inversion: The Valhall case study: *Geophysical Journal International*, **187**(3), 1495–1515, doi: 10.1111/j.1365-246X.2011.05209.x.
- Roecker, S., B. Baker, and J. McLaughlin, 2010, A finite-difference algorithm for full waveform teleseismic tomography: *Geophysical Journal International*, **181**, 1017–1040, doi: 10.1111/j.1365-246X.2010.04553.x.
- Scales, J. A., 1987, Tomographic inversion via the conjugate gradient method: *Geophysics*, **52**(2), 179–185, doi: 10.1190/1.1442293.
- Shin, C., and Y. H. Cha, 2009, Waveform inversion in the Laplace-Fourier domain: *Geophysical Journal International*, **177**(3), 1067–1079, doi: 10.1111/j.1365-246X.2009.04102.x.
- Sirgue, L., 2003, Inversion de la forme d'onde dans le domaine fréquentiel de données sismiques grands offsets: Ph.d. thesis, Ecole Normale Supérieure de Paris et Queen's University.
- Sirgue, L., O. Bakverd, J. Van Gestel, J. Askim, O., and J. Kommendal, 2009, 3D Waveform Inversion on Valhall Wide-azimuth OBC: Presented at the 71st Annual International Conference and Exhibition, EAGE, Extended Abstracts, doi: 10.3997/2214-4609.201400395.
- Sirgue, L., and R. G. Pratt, 2004, Efficient waveform inversion and imaging: A strategy for selecting temporal frequencies: *Geophysics*, **69**(1), 231–248, doi: 10.1190/1.1649391.
- Smithyman, B. R., and R. M. Clowes, 2012, Waveform tomography of field vibroseis data using an approximate 2D geometry leads to improved velocity models: *Geophysics*, **77**(1), R33–R43, doi: 10.1190/geo2011-0076.1.
- , 2013, Waveform tomography in 2.5D: Parameterization for crooked-line acquisition geometry: *Journal of Geophysical Research: Solid Earth*, **118**(5), 2119–2137, doi: 10.1002/jgrb.50100.
- Southworth, C. S., K. J. Gray, and J. F. Sutter, 1992, Middle Eocene intrusive igneous rocks of the central Appalachian Valley and Ridge Province - Setting, chemistry and implications for crustal structure: Technical Report B1839-J.
- Tarantola, A., 1984, Inversion of seismic reflection data in the acoustic approximation: *Geophysics*, **49**(8), 1259–1266, doi: 10.1190/1.1441754.
- Thomsen, L., 1986, Weak elastic anisotropy: *Geophysics*, **51**(10), 1954–1966, doi: 10.1190/1.1442051.
- Tikhonov, A. N., and V. Y. Arsenin, 1977, Solutions of ill posed problems: W. H. Winston and Sons.
- Tsvankin, I., 2012, *Seismic Signatures and Analysis of Reflection Data in Anisotropic Media*, 3 ed.: SEG.
- Umpleby, A., M. Warner, and I. Stekl, 2010, Time vs frequency for 3D wavefield tomography: Presented at the 72nd Annual International Conference and Exhibition incorporating SPE EUROPEC 2010, EAGE, Extended Abstracts, doi: 10.3997/2214-4609.20149941.
- Vigh, D., and E. W. Starr, 2008, 3D prestack plane-wave, full-waveform inversion: *Geophysics*, **73**(5), VE135–VE144, doi: 10.1190/1.2952623.
- Vinje, V., E. Iversen, and H. Gjoystdal, 1993, Traveltime and amplitude estimation using wavefront construction: *Geophysics*, **58**(8), 1157–1166, doi: 10.1190/1.1443499.
- Virieux, J., and S. Operto, 2009, An overview of full-waveform inversion in exploration geophysics: *Geophysics*, **74**(6), WCC1–WCC26, doi: 10.1190/1.3238367.

BIBLIOGRAPHY

- Warner, M., A. Ratcliffe, T. Nangoo, J. Morgan, A. Umpleby, N. Shah, V. Vinje, I. Štekl, L. Guasch, C. Win, G. Conroy, and A. Bertrand, 2013, Anisotropic 3D full-waveform inversion: *Geophysics*, **78**(2), R59–R80, doi: 10.1190/geo2012-0338.1.
- Woodward, M. J., 1992, Wave-equation tomography: *Geophysics*, **57**(1), 15–26.
- Yao, G., and D. Wu, 2017, Reflection full waveform inversion: *Science China Earth Sciences*, **60**(10), 1783–1794, doi: 10.1007/s11430-016-9091-9.
- Yilmaz, Ö., 2001, *Seismic Data Analysis: Processing, Inversion, and Interpretation of Seismic Data*: SEG. doi: 10.1190/1.9781560801580.
- Zhang, J., and M. N. Toksöz, 1998, Nonlinear refraction traveltime tomography: *Geophysics*, **63**(5), 1726–1737, doi: 10.1190/1.1444468.
- Zuberi, M. A. H., and R. G. Pratt, 2016, Mitigating Non-linearity in Full Waveform Inversion by Scaled Sobolev Pre-conditioning: Presented at the 78th Annual International Conference and Exhibition, EAGE, Extended Abstracts, doi: 10.3997/2214-4609.201601007.
- , 2017, Mitigating the non-linearity in full waveform inversion using scaled-Sobolev pre-conditioning: *Geophysical Journal International*, ggx549, doi: 10.1093/gji/ggx549.

Appendix A

Wave Equations

This appendix presents more detailed mathematical background for elastic wave equations and the acoustic wave equations. This material is relevant to the FWI work completed because acoustic wave equation was used in the forward modelling steps of FWI. The information presented here helps with underlying assumptions made in the physics that govern sound waves. Because the information presented here is available widely in literature, I have placed it in this appendix.

A.1 Elastic media

“A medium is said to be elastic if it possess a natural state (in which strains and stresses are zero) to which it will revert when applied forces are removed” (Aki and Richards, 1980). It is important to note that elasticity is assumed—that is—rocks that deform will come back to their original shape. For a seismic wave, the elastic assumption is reasonable for propagation through rocks, given that the signal being recorded is not too close to the seismic source (where permanent deformations may occur). Consider, for example, a dynamite source that explodes about 10 metres below the surface. Some of the rock will permanently deform around the explosion, and will not be perfectly elastic. It will then not obey the elastic equations derived here.

The seismic wave equation for propagation in elastic solids can be derived from Hooke’s law and Newton’s second law of motion. Understanding the concepts of stress and strain is essential to properly relate them using Hooke’s law. Stress and strain here are considered in 3D, and then reduced to 2D. *Stress can be defined as force per unit area, and strain can be defined as extension per unit length.* Seismic waves propagate through rocks and as they propagate there is a force that acts upon the rocks (stress). This stress that acts on the rocks induces slight deformations (strain). The mathematical background that follows is in large part directly from Yilmaz (2001), Aki and Richards (1980), Thomsen (1986), and Tsvankin (2012).

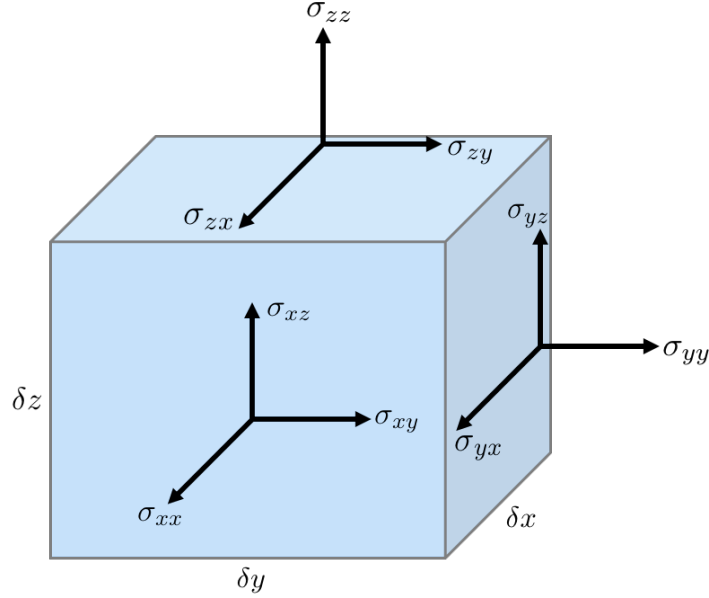


Figure A.1: Infinitesimally small cube of dimensions $\delta x \times \delta y \times \delta z$, with all nine stress components labelled. Modified from [Yilmaz \(2001\)](#).

A.1.1 Stress

Consider an infinitesimally small cube with dimensions δx , δy , and δz (Figure A.1). Stress can act on any one of the surfaces of this cube. Consider, for example, that stress acts on the surface of $\delta y \times \delta z$, and define σ_{xx} to be that stress acting in the normal direction. A positive σ_{xx} is said to be *tensional stress* and a negative σ_{xx} is said to be *compressional stress*. There are also stresses that act parallel to the surface, defined as σ_{xy} and σ_{xz} . The first subscript indicates the normal direction to the surface, while the second indicates the stress component direction. For the surfaces $\delta x \times \delta y$ and $\delta x \times \delta z$, similar definitions can be constructed. Each of these stresses make up what is commonly known as the Cauchy stress tensor matrix:

$$\sigma_{ij} = \begin{pmatrix} \sigma_{xx} & \sigma_{xy} & \sigma_{xz} \\ \sigma_{yx} & \sigma_{yy} & \sigma_{yz} \\ \sigma_{zx} & \sigma_{zy} & \sigma_{zz} \end{pmatrix}. \quad (\text{A.1})$$

The diagonal elements, σ_{xx} , σ_{yy} , and σ_{zz} , are known as the *normal stress components*, while the off-diagonals, σ_{yx} , σ_{xy} , σ_{zx} , σ_{xz} , σ_{zy} , and σ_{yz} , are known as the *shear stress components*. If the dimensions of the cube are made infinitesimally small, then the sum of the surface forces about any axis will become 0:

$$\begin{aligned}
 \sigma_{xy} - \sigma_{yx} &= 0, \\
 \sigma_{xz} - \sigma_{zx} &= 0, \\
 \sigma_{yz} - \sigma_{zy} &= 0,
 \end{aligned}
 \tag{A.2}$$

or $\sigma_{xy} = \sigma_{yx}$, $\sigma_{xz} = \sigma_{zx}$, and $\sigma_{zy} = \sigma_{yz}$, making the stress tensor matrix symmetrical. Further discussion on the symmetry of the stress tensor can be found in [Aki and Richards \(1980\)](#).

A.1.2 Strain

Strain can be defined as extension per unit length, and is thus a dimensionless quality. Consider two points, A and B , within a solid body being subject to stress. If deformed, they become new points A' and B' . The displacement from from old to new point locations can be expressed by

$$\begin{pmatrix} \delta u_x \\ \delta u_y \\ \delta u_z \end{pmatrix} = \begin{pmatrix} \partial u_x / \partial x & \partial u_x / \partial y & \partial u_x / \partial z \\ \partial u_y / \partial x & \partial u_y / \partial y & \partial u_y / \partial z \\ \partial u_z / \partial x & \partial u_z / \partial y & \partial u_z / \partial z \end{pmatrix} \begin{pmatrix} \delta x \\ \delta y \\ \delta z \end{pmatrix}.
 \tag{A.3}$$

Expanding the first row would result in a displacement of u ,

$$\delta u_x = \frac{\partial u_x}{\partial x} \delta x + \frac{\partial u_x}{\partial y} \delta y + \frac{\partial u_x}{\partial z} \delta z.
 \tag{A.4}$$

The displacements in equation [A.3](#) can be written ([Aki and Richards, 1980](#)) in a more compact notation as

$$\delta u_i = \frac{\partial u_i}{\partial x_j} \delta x_j.
 \tag{A.5}$$

When the displacement between two points becomes very small, the derivative of u_i equals the displacement. Rearranging equation [A.5](#),

$$\frac{\partial u_i}{\partial x_j} = \frac{\delta u_i}{\delta x_j}.
 \tag{A.6}$$

The displacement equation [A.3](#) is for some general displacement, but a solid body (or rock) can be deformed in various ways. Similar to the stress tensor matrix, the strain tensor matrix can be written as

$$e_{kl} = \begin{pmatrix} e_{xx} & e_{xy} & e_{xz} \\ e_{yx} & e_{yy} & e_{yz} \\ e_{zx} & e_{zy} & e_{zz} \end{pmatrix}, \quad (\text{A.7})$$

where the diagonal elements represent the *normal strain* components, and the off-diagonal components represent *shear strain* components. The normal strain components are defined in terms of particle displacement as

$$e_{xx} = \frac{\partial u_x}{\partial x}, \quad (\text{A.8})$$

$$e_{yy} = \frac{\partial u_y}{\partial y}, \quad (\text{A.9})$$

and

$$e_{zz} = \frac{\partial u_z}{\partial z}. \quad (\text{A.10})$$

A positive normal strain is called an *extension*, and a negative normal strain is called a *contraction*. Only three more types of strain are required to sufficiently approximate every kind of strain to an infinitesimally small cube: linear stretching, shearing, rotation, and a combination of both shearing and rotation. An assumption is made here that whatever shape in deformation occurs, the shapes presented are good estimates for *any* deformation. Because the cube is assumed to be infinitesimally small, this is a reasonable assumption.

Angular deformations ξ and ζ in the $\delta x \times \delta z$ plane are defined as

$$\xi = e_{xz} = e_{zx} \quad (\text{A.11})$$

and

$$\zeta = \theta_{xz} = -\theta_{zx} \quad (\text{A.12})$$

(see Figure A.2). As the volume becomes infinitesimally small, angular deformations can be defined in terms of displacement, such that

$$\xi - \zeta = \frac{\partial u_z}{\partial x} \quad (\text{A.13})$$

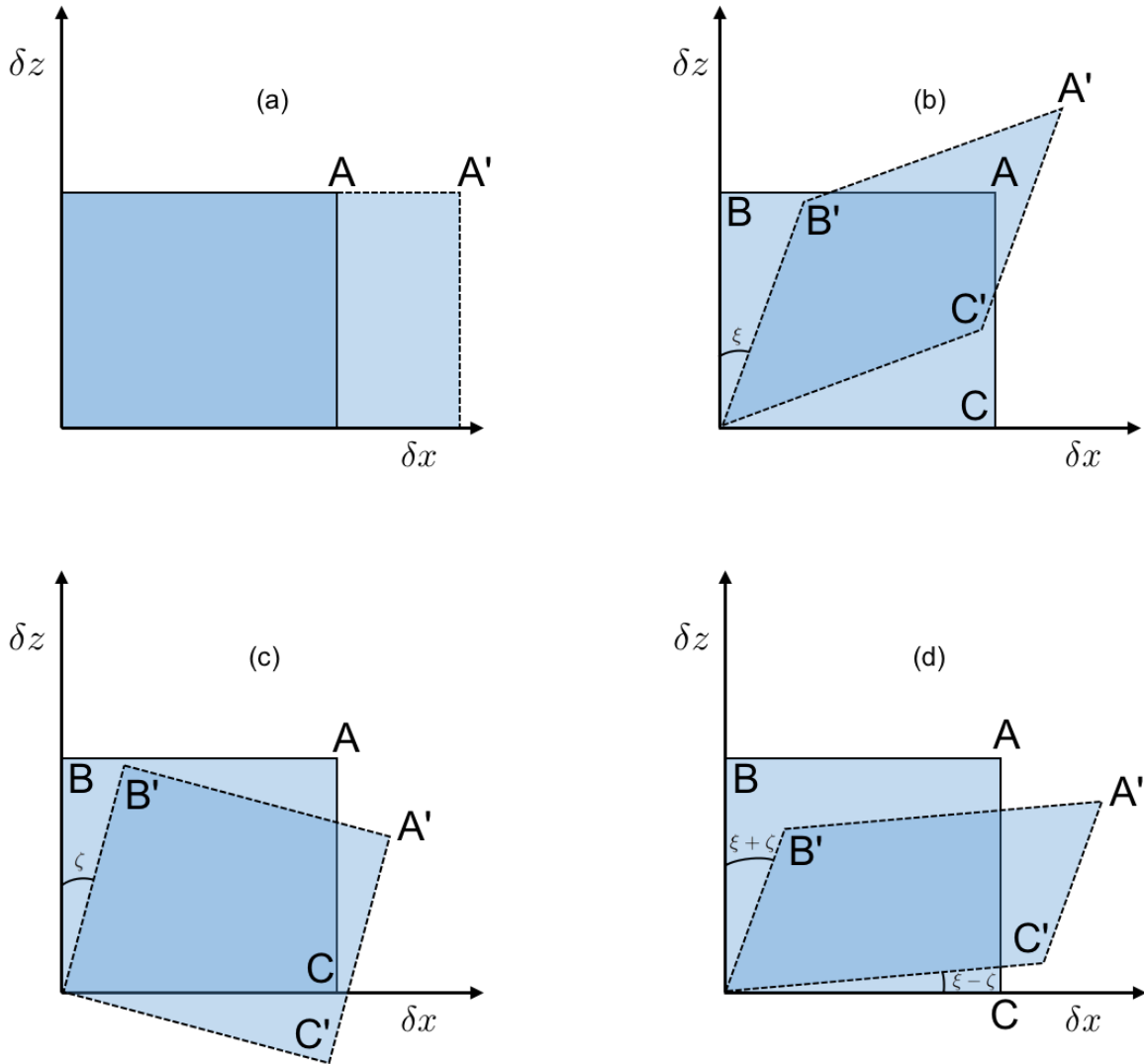


Figure A.2: Stress causes slight deformations (strain), depicted here on the $\delta x \times \delta z$ plane: (a) linear ‘stretching’; (b) shearing only; (c) rotation only; (d) combined shearing and rotation. Adapted from [Yilmaz \(2001\)](#).

and

$$\xi + \zeta = \frac{\partial u_x}{\partial z} \quad (\text{A.14})$$

(see Figure A.2). Adding equations A.13 and A.14 results in

$$2\xi = \frac{\partial u_z}{\partial x} + \frac{\partial u_x}{\partial z}. \quad (\text{A.15})$$

Thus,

$$\xi = e_{xz} = \frac{1}{2} \left(\frac{\partial u_z}{\partial x} + \frac{\partial u_x}{\partial z} \right) = e_{zx}. \quad (\text{A.16})$$

By the same analysis in the $\delta x \times \delta y$ plane,

$$e_{xy} = \frac{1}{2} \left(\frac{\partial u_y}{\partial x} + \frac{\partial u_x}{\partial y} \right) = e_{yx}, \quad (\text{A.17})$$

and in the $\delta y \times \delta z$ plane,

$$e_{yz} = \frac{1}{2} \left(\frac{\partial u_z}{\partial y} + \frac{\partial u_y}{\partial z} \right) = e_{zy}. \quad (\text{A.18})$$

The relationship between strain e_{ij} and particle displacement u_i can be written compactly for all cases as

$$e_{ij} = \frac{1}{2} \left(\frac{\partial u_i}{\partial j} + \frac{\partial u_j}{\partial i} \right), \quad i, j = x, y, z. \quad (\text{A.19})$$

Equations A.16, A.17, and A.18 represent the shear strain components from equation A.7. The rotational deformation component must now be considered. Beginning in the $\delta x \times \delta z$ plane, and subtracting equations A.13 and A.14, the result is

$$-2\zeta = \frac{\partial u_z}{\partial x} - \frac{\partial u_x}{\partial z}.$$

Thus,

$$\zeta = \theta_{xz} = -\frac{1}{2} \left(\frac{\partial u_z}{\partial x} - \frac{\partial u_x}{\partial z} \right) = -\theta_{zx}. \quad (\text{A.20})$$

By the same analysis in the $\delta x \times \delta y$ plane,

$$\theta_{xy} = -\frac{1}{2} \left(\frac{\partial u_y}{\partial x} - \frac{\partial u_x}{\partial y} \right) = -\theta_{yx}, \quad (\text{A.21})$$

and in the $\delta y \times \delta z$ plane,

$$\theta_{yz} = -\frac{1}{2} \left(\frac{\partial u_z}{\partial y} - \frac{\partial u_y}{\partial z} \right) = -\theta_{zy}. \quad (\text{A.22})$$

The displacement tensor in equation A.3 can now be written in an expanded form such that

$$\begin{pmatrix} \delta u_x \\ \delta u_y \\ \delta u_z \end{pmatrix} = \frac{1}{2} \begin{pmatrix} \partial u_x / \partial x + \partial u_x / \partial x & \partial u_y / \partial x + \partial u_x / \partial y & \partial u_z / \partial x + \partial u_x / \partial z \\ \partial u_x / \partial y + \partial u_y / \partial x & \partial u_y / \partial y + \partial u_y / \partial y & \partial u_z / \partial y + \partial u_y / \partial z \\ \partial u_x / \partial z + \partial u_z / \partial x & \partial u_y / \partial z + \partial u_z / \partial y & \partial u_z / \partial z + \partial u_z / \partial z \end{pmatrix} \begin{pmatrix} \delta x \\ \delta y \\ \delta z \end{pmatrix} - \frac{1}{2} \begin{pmatrix} 0 & \partial u_y / \partial x - \partial u_x / \partial y & \partial u_z / \partial x - \partial u_x / \partial z \\ \partial u_x / \partial y - \partial u_y / \partial x & 0 & \partial u_z / \partial y - \partial u_y / \partial z \\ \partial u_x / \partial z - \partial u_z / \partial x & \partial u_y / \partial z - \partial u_z / \partial y & 0 \end{pmatrix} \begin{pmatrix} \delta x \\ \delta y \\ \delta z \end{pmatrix}, \quad (\text{A.23})$$

reducing to

$$\begin{pmatrix} \delta u_x \\ \delta u_y \\ \delta u_z \end{pmatrix} = \begin{pmatrix} e_{xx} & e_{xy} & e_{xz} \\ e_{yx} & e_{yy} & e_{yz} \\ e_{zx} & e_{zy} & e_{zz} \end{pmatrix} + \begin{pmatrix} 0 & \theta_{xy} & \theta_{xz} \\ \theta_{yx} & 0 & \theta_{yz} \\ \theta_{zx} & \theta_{zy} & 0 \end{pmatrix} \begin{pmatrix} \delta x \\ \delta y \\ \delta z \end{pmatrix}. \quad (\text{A.24})$$

A.1.3 Hooke's law and elastic tensor

Next, we need to establish a relationship between the Cauchy stress tensor in equation A.1 and the strain tensor in equation A.7. They can be related by the generalized Hooke's law, expressed by

$$\sigma_{ij} = c_{ijkl} e_{kl}, \quad (\text{A.25})$$

where σ_{ij} is the stress tensor, c_{ijkl} is the elastic (or 'stiffness') tensor, and e_{kl} is the strain tensor. The elastic tensor is defined by crystal lattice structures in solid state physics. Additional information

on the theory of elastic waves in crystals can be found in [Fedorov \(1968\)](#), [Nye \(1957\)](#), [Helbig and Schoenberg \(1987\)](#), and [Helbig \(1994\)](#).

The elastic tensor of rank four with 81 constants can be expanded in 3D space as

$$c_{ijkl} = \begin{pmatrix} \begin{pmatrix} c_{1111} & c_{1112} & c_{1113} \\ c_{1112} & c_{1122} & c_{1123} \\ c_{1113} & c_{1123} & c_{1133} \end{pmatrix} & \begin{pmatrix} c_{1211} & c_{1212} & c_{1213} \\ c_{1212} & c_{1222} & c_{1223} \\ c_{1213} & c_{1223} & c_{1233} \end{pmatrix} & \begin{pmatrix} c_{1311} & c_{1312} & c_{1313} \\ c_{1312} & c_{1322} & c_{1323} \\ c_{1313} & c_{1323} & c_{1333} \end{pmatrix} \\ \begin{pmatrix} c_{1211} & c_{1212} & c_{1213} \\ c_{1212} & c_{1222} & c_{1223} \\ c_{1213} & c_{1223} & c_{1233} \end{pmatrix} & \begin{pmatrix} c_{2211} & c_{2212} & c_{2213} \\ c_{2212} & c_{2222} & c_{2223} \\ c_{2213} & c_{2223} & c_{2233} \end{pmatrix} & \begin{pmatrix} c_{2311} & c_{2312} & c_{2313} \\ c_{2312} & c_{2322} & c_{2323} \\ c_{2313} & c_{2323} & c_{2333} \end{pmatrix} \\ \begin{pmatrix} c_{1311} & c_{1312} & c_{1313} \\ c_{1312} & c_{1322} & c_{1323} \\ c_{1313} & c_{1323} & c_{1333} \end{pmatrix} & \begin{pmatrix} c_{2311} & c_{2312} & c_{2313} \\ c_{2312} & c_{2322} & c_{2323} \\ c_{2313} & c_{2323} & c_{2333} \end{pmatrix} & \begin{pmatrix} c_{3311} & c_{3312} & c_{3313} \\ c_{3312} & c_{3322} & c_{3323} \\ c_{3313} & c_{3323} & c_{3333} \end{pmatrix} \end{pmatrix} \quad (\text{A.26})$$

(after [Helbig, 1994](#)). The $3 \times 3 \times 3 \times 3$ elastic tensor c_{ijkl} has several symmetries that immediately reduce the number of elastic constants from 81 to 21. The symmetry of stress ($\sigma_{ij} = \sigma_{ji}$) and the symmetry of strain ($e_{kl} = e_{lk}$) result in equalities

$$c_{ijkl} = c_{jikl} \quad (\text{A.27})$$

and

$$c_{ijkl} = c_{ijlk}. \quad (\text{A.28})$$

It is also true from a thermodynamic standpoint that

$$c_{ijkl} = c_{klij}. \quad (\text{A.29})$$

[Aki and Richards \(1980\)](#) offer a proof beginning from the first law of thermodynamics to establish [A.29](#). Following from equations [A.27](#), [A.28](#), and [A.29](#), the stiffness tensor can be written in the form of a 6×6 matrix, with only 21 independent constants. To simplify notation, the ‘‘Voigt recipe’’ for indices can be used as follows:

$$\begin{array}{cccccc} 11 & 22 & 33 & 23=32 & 13=31 & 12=21 \\ \downarrow & \downarrow & \downarrow & \downarrow & \downarrow & \downarrow \\ 1 & 2 & 3 & 4 & 5 & 6 \end{array} .$$

When anisotropic symmetries are increased, the number of independent elastic constants decreases. The new elastic tensor is of rank two with 21 independent constants and can be written in what is

called triclinic form, with no symmetry planes (Tsvankin, 2012),

$$\mathbf{c}^{(\text{TRC})} = \begin{pmatrix} c_{11} & c_{12} & c_{13} & c_{14} & c_{15} & c_{16} \\ c_{12} & c_{22} & c_{23} & c_{24} & c_{25} & c_{26} \\ c_{13} & c_{23} & c_{33} & c_{34} & c_{35} & c_{36} \\ c_{14} & c_{24} & c_{34} & c_{44} & c_{45} & c_{46} \\ c_{15} & c_{25} & c_{35} & c_{45} & c_{55} & c_{56} \\ c_{16} & c_{26} & c_{36} & c_{46} & c_{56} & c_{66} \end{pmatrix}. \quad (\text{A.30})$$

Equation A.30 is known as the most general form of anisotropy for the elastic tensor. The matrix is completely symmetric, reducing the number of independent constants from what would be 36 in a 6×6 matrix to only 21. The generalized Hooke's law given by A.25 can be written in expanded form relating stress to strain such that

$$\begin{pmatrix} \sigma_{xx} \\ \sigma_{yy} \\ \sigma_{zz} \\ \sigma_{xy} \\ \sigma_{xz} \\ \sigma_{yz} \end{pmatrix} = \begin{pmatrix} c_{11} & c_{12} & c_{13} & c_{14} & c_{15} & c_{16} \\ c_{12} & c_{22} & c_{23} & c_{24} & c_{25} & c_{26} \\ c_{13} & c_{23} & c_{33} & c_{34} & c_{35} & c_{36} \\ c_{14} & c_{24} & c_{34} & c_{44} & c_{45} & c_{46} \\ c_{15} & c_{25} & c_{35} & c_{45} & c_{55} & c_{56} \\ c_{16} & c_{26} & c_{36} & c_{46} & c_{56} & c_{66} \end{pmatrix} \begin{pmatrix} e_{xx} \\ e_{yy} \\ e_{zz} \\ e_{xy} \\ e_{xz} \\ e_{yz} \end{pmatrix}. \quad (\text{A.31})$$

In seismology, it is often necessary to simplify the stiffness tensor matrix for geological reasons—that is—to reduce the number of parameters in A.30 for robust solutions. An elastic medium can be simplified by taking certain axes to be symmetric.

In exploration seismology, the tensors that follow are some of the most common simplifications of equation A.30, according to specific symmetry assumptions (Tsvankin, 2012). These symmetry assumptions are often referred to as “increasing the order of symmetry.” The monoclinic tensor can be written as

$$\mathbf{c}^{(\text{MNC})} = \begin{pmatrix} c_{11} & c_{12} & c_{13} & & & c_{16} \\ c_{12} & c_{22} & c_{23} & & & c_{26} \\ c_{13} & c_{23} & c_{33} & & & c_{36} \\ & & & c_{44} & c_{45} & \\ & & & c_{45} & c_{55} & \\ c_{16} & c_{26} & c_{36} & & & c_{66} \end{pmatrix}; \quad (\text{A.32})$$

the orthorhombic tensor, with three mutually orthogonal planes of reflection symmetry, can be written as

$$\mathbf{c}^{(\text{ORT})} = \begin{pmatrix} c_{11} & c_{12} & c_{13} & & & \\ c_{12} & c_{22} & c_{23} & & & \\ c_{13} & c_{23} & c_{33} & & & \\ & & & c_{44} & & \\ & & & & c_{55} & \\ & & & & & c_{66} \end{pmatrix}; \quad (\text{A.33})$$

and vertical transverse isotropy (VTI) tensor can be written as

$$\mathbf{c}^{(\text{VTI})} = \begin{pmatrix} c_{11} & c_{11} - 2c_{66} & c_{13} & & & \\ c_{11} - 2c_{66} & c_{22} & c_{13} & & & \\ c_{13} & c_{13} & c_{33} & & & \\ & & & c_{44} & & \\ & & & & c_{44} & \\ & & & & & c_{66} \end{pmatrix}. \quad (\text{A.34})$$

In some publications, including in [Tsvankin \(2012\)](#), c_{44} is written as c_{55} . This is only a question of notation, as $c_{44} = c_{55}$ in VTI media. In horizontal transverse isotropy (HTI), the elastic tensor can be written as

$$\mathbf{c}^{(\text{HTI})} = \begin{pmatrix} c_{11} & c_{13} & c_{13} & & & \\ c_{13} & c_{22} & c_{33} - 2c_{44} & & & \\ c_{13} & c_{33} - 2c_{44} & c_{33} & & & \\ & & & c_{44} & & \\ & & & & c_{55} & \\ & & & & & c_{55} \end{pmatrix}; \quad (\text{A.35})$$

and in isotropic media

$$\mathbf{c}^{(\text{ISO})} = \begin{pmatrix} c_{33} & c_{33} - 2c_{44} & c_{33} - 2c_{44} & & & \\ c_{33} - 2c_{44} & c_{33} & c_{33} - 2c_{44} & & & \\ c_{33} - 2c_{44} & c_{33} - 2c_{44} & c_{33} & & & \\ & & & c_{44} & & \\ & & & & c_{44} & \\ & & & & & c_{44} \end{pmatrix},$$

$$\mathbf{c}^{(\text{ISO})} = \begin{pmatrix} \lambda + 2\mu & \lambda & \lambda & & & \\ \lambda & \lambda + 2\mu & \lambda & & & \\ \lambda & \lambda & \lambda + 2\mu & & & \\ & & & 2\mu & & \\ & & & & 2\mu & \\ & & & & & 2\mu \end{pmatrix}, \quad (\text{A.36})$$

where λ and μ are defined Lamé parameters, or elastic moduli. Specifically, μ is called the shear modulus and λ is called Lamé's modulus of fluid incompressibility. These parameters make up what is known as the bulk modulus for homogeneous isotropic media, written

$$\kappa = \lambda + \frac{2}{3}\mu. \quad (\text{A.37})$$

Table A.1 summarizes the number of independent parameters for each elastic tensor.¹

Table A.1: Number of independent parameters for the elastic tensors described with increasing order of symmetry.

Symmetry	Elastic Parameters
triclinic	21
monoclinic	13
orthorhombic	9
transversely isotropic (VTI, TTI, HTI)	5
isotropic	2

A.1.4 Equations of motion and wave equations

Newton's equations of motion can be written in the frequency domain as

$$-\omega^2 \rho u_x = \frac{\partial \sigma_{xx}}{\partial x} + \frac{\partial \sigma_{xy}}{\partial y} + \frac{\partial \sigma_{xz}}{\partial z} + f_x, \quad (\text{A.38})$$

$$-\omega^2 \rho u_y = \frac{\partial \sigma_{xy}}{\partial x} + \frac{\partial \sigma_{yy}}{\partial y} + \frac{\partial \sigma_{yz}}{\partial z} + f_y, \quad (\text{A.39})$$

and

$$-\omega^2 \rho u_z = \frac{\partial \sigma_{xz}}{\partial x} + \frac{\partial \sigma_{yz}}{\partial y} + \frac{\partial \sigma_{zz}}{\partial z} + f_z, \quad (\text{A.40})$$

where ω is the angular frequency ($= 2\pi f$); ρ is the density; u_i ($i = x, y, z$) are the particle displacements; σ_{ij} ($i, j = x, y, z$) are the stress components; and f_i ($i = x, y, z$) are the source terms. By

¹Helbig (1994) uses slightly different numbers in his table for triclinic and monoclinic media, as there are further simplifications that can be made to reduce these number of parameters; these simplifications can be explored further in Helbig (1994) and Tsvankin (2012).

substituting Hooke's law (equation A.25) into the equations of motion A.38, A.39, and A.40, the wave equation can be derived. A strictly first-order hyperbolic system is considered here.

A.1.4.1 3D VTI elastic wave equations

One very commonly used form of anisotropy is VTI, because of the flat way in which geologic strata are typically layered. Hooke's law for VTI media can be stated as

$$\begin{pmatrix} \sigma_{xx} \\ \sigma_{yy} \\ \sigma_{zz} \\ \sigma_{xy} \\ \sigma_{xz} \\ \sigma_{yz} \end{pmatrix} = \begin{pmatrix} c_{11} & c_{11} - 2c_{66} & c_{13} & & & \\ c_{11} - 2c_{66} & c_{22} & c_{13} & & & \\ c_{13} & c_{13} & c_{33} & & & \\ & & & c_{44} & & \\ & & & & c_{44} & \\ & & & & & c_{66} \end{pmatrix} \begin{pmatrix} e_{xx} \\ e_{yy} \\ e_{zz} \\ e_{xy} \\ e_{xz} \\ e_{yz} \end{pmatrix}. \quad (\text{A.41})$$

Expanding, the system of equations becomes

$$\begin{aligned} \sigma_{xx} &= c_{11}e_{xx} + (c_{11} - 2c_{66})e_{yy} + c_{13}e_{zz} \\ \sigma_{yy} &= (c_{11} - 2c_{66})e_{xx} + c_{22}e_{yy} + c_{13}e_{zz} \\ \sigma_{zz} &= c_{13}e_{xx} + c_{13}e_{yy} + c_{33}e_{zz} \\ \sigma_{xy} &= c_{44}e_{xy} \\ \sigma_{xz} &= c_{44}e_{xz} \\ \sigma_{yz} &= c_{66}e_{yz}. \end{aligned} \quad (\text{A.42})$$

Substituting the stress parameters from equation A.42 into equations A.38, A.39, and A.40, the new equations of motion become

$$-\omega^2 \rho u_x = \frac{\partial}{\partial x} [c_{11}e_{xx} + (c_{11} - 2c_{66})e_{yy} + c_{13}e_{zz}] + \frac{\partial}{\partial y} (c_{44}e_{xy}) + \frac{\partial}{\partial z} (c_{44}e_{xz}) + f_x, \quad (\text{A.43})$$

$$-\omega^2 \rho u_y = \frac{\partial}{\partial x} (2c_{44}e_{xy}) + \frac{\partial}{\partial y} [(c_{11} - 2c_{66})e_{xx} + c_{22}e_{yy} + c_{13}e_{zz}] + \frac{\partial}{\partial z} (c_{66}e_{yz}) + f_y, \quad (\text{A.44})$$

and

$$-\omega^2 \rho u_z = \frac{\partial}{\partial x} (2c_{44}e_{xz}) + \frac{\partial}{\partial y} (2c_{66}e_{yz}) + \frac{\partial}{\partial z} (c_{13}e_{xx} + c_{13}e_{yy} + c_{33}e_{zz}) + f_z. \quad (\text{A.45})$$

Substituting strain (e_{ij}) from equations A.8, A.9, A.10, A.16, A.17, and A.18, the elastic wave

equations for inhomogeneous 3D VTI media can be written as

$$-\omega^2 \rho u_x = \frac{\partial}{\partial x} \left[c_{11} \frac{\partial u_x}{\partial x} + (c_{11} - 2c_{66}) \frac{\partial u_y}{\partial y} + c_{13} \frac{\partial u_z}{\partial z} \right] + \frac{\partial}{\partial y} \left[c_{44} \left(\frac{\partial u_x}{\partial y} + \frac{\partial u_y}{\partial x} \right) \right] + \frac{\partial}{\partial z} \left[c_{44} \left(\frac{\partial u_z}{\partial x} + \frac{\partial u_x}{\partial z} \right) \right] + f_x, \quad (\text{A.46})$$

$$-\omega^2 \rho u_y = \frac{\partial}{\partial x} \left[c_{44} \left(\frac{\partial u_y}{\partial x} + \frac{\partial u_x}{\partial y} \right) \right] + \frac{\partial}{\partial y} \left[(c_{11} - 2c_{66}) \frac{\partial u_x}{\partial x} + c_{22} \frac{\partial u_y}{\partial y} + c_{13} \frac{\partial u_z}{\partial z} \right] + \frac{\partial}{\partial z} \left[c_{66} \left(\frac{\partial u_z}{\partial y} + \frac{\partial u_y}{\partial z} \right) \right] + f_y, \quad (\text{A.47})$$

and

$$-\omega^2 \rho u_z = \frac{\partial}{\partial x} \left[c_{44} \left(\frac{\partial u_z}{\partial x} + \frac{\partial u_x}{\partial z} \right) \right] + \frac{\partial}{\partial y} \left[c_{66} \left(\frac{\partial u_z}{\partial y} + \frac{\partial u_y}{\partial z} \right) \right] + \frac{\partial}{\partial z} \left[c_{13} \frac{\partial u_x}{\partial x} + c_{13} \frac{\partial u_y}{\partial y} + c_{33} \frac{\partial u_z}{\partial z} \right] + f_z. \quad (\text{A.48})$$

It is important to note that the constants in the lower right quadrant (c_{44} and c_{66}) are arbitrary, and can therefore absorb the fraction of $1/2$ from equations [A.16](#), [A.17](#), and [A.18](#).

A.1.4.2 VTI Thomsen parameters

[Thomsen \(1986\)](#) defined three anisotropy parameters that have become so widely used that they are now commonly referred to as the ‘Thomsen parameters.’ They are defined as follows for VTI media:

$$\varepsilon \equiv \frac{c_{11} - c_{33}}{2c_{33}}, \quad (\text{A.49})$$

$$\gamma \equiv \frac{c_{66} - c_{44}}{2c_{44}}, \quad (\text{A.50})$$

and

$$\delta \equiv \frac{(c_{13} + c_{44})^2 - (c_{33} - c_{44})^2}{2c_{33}(c_{33} - c_{44})}. \quad (\text{A.51})$$

It is now a common practice to estimate anisotropic parameters, especially in geologically complex environments. However, only epsilon (ε) and delta (δ) are usually estimated for field data cases.

The reason for discarding gamma (γ) is that robust and computationally efficient algorithms available today are only concerned only with Primary-wave (P-wave) effects, and ignore Shear-wave (S-waves) effects, which would involve gamma (γ). Thomsen (1986) further determined that most rocks are only ‘weakly’ anisotropic, which typically exhibit anisotropy values ε , γ , and $\delta < 0.2$. For weak anisotropy, the phase velocities can be defined by

$$v_P(\theta) = \alpha_0(1 + \delta \sin^2\theta \cos^2\theta + \varepsilon \sin^4\theta), \quad (\text{A.52})$$

$$v_{SV}(\theta) = \beta_0 \left[1 + \frac{\alpha_0^2}{\beta_0^2} (\varepsilon - \delta) \sin^2\theta \cos^2\theta \right], \quad (\text{A.53})$$

and

$$v_{SH}(\theta) = \beta_0(1 + \gamma \sin^2\theta), \quad (\text{A.54})$$

where v_P is the P-wave velocity, v_{SV} is the S-wave velocity in the vertical direction, v_{SH} is the S-wave velocity in the horizontal direction, and θ is the phase angle. The parameters α_0 and β_0 are defined as

$$\alpha_0 = \sqrt{\frac{c_{33}}{\rho}} \quad (\text{A.55})$$

and

$$\beta_0 = \sqrt{\frac{c_{44}}{\rho}}. \quad (\text{A.56})$$

It is useful to note that when $\delta = \varepsilon = 0$, α_0 is by definition the P-wave velocity and when $\delta = \varepsilon = \gamma = 0$, β_0 is by definition the S-wave velocity. In that case, the media would be isotropic, and thus have the same P-wave velocity in any direction, and the same S-wave velocity in any direction.

A.1.4.3 2D VTI elastic wave equations

In seismic exploration, most datasets have historically been recorded in 2D, and therefore the forward modelling code and inversion code are written in 2D. In the last decade with the advent of computers working in parallel, that trend has been changing, with more data recorded in 3D. The computational costs for dealing with 3D data are very expensive. We now consider the 2D

case for VTI media. The elastic tensors simplify to a 3×3 matrix, with only 4 independent elastic parameters, written as

$$\mathbf{c}^{(\text{VTI-2D})} = \begin{pmatrix} c_{11} & c_{13} & \\ c_{13} & c_{33} & \\ & & c_{44} \end{pmatrix}. \quad (\text{A.57})$$

Hooke's Law for 2D VTI media can be written as

$$\begin{pmatrix} \sigma_{xx} \\ \sigma_{zz} \\ \sigma_{xz} \end{pmatrix} = \begin{pmatrix} c_{11} & c_{13} & \\ c_{13} & c_{33} & \\ & & c_{44} \end{pmatrix} \begin{pmatrix} e_{xx} \\ e_{zz} \\ e_{xz} \end{pmatrix}. \quad (\text{A.58})$$

When reducing to 2D, the displacement of y can be defined to be 0, and the particle velocity of y can be defined to be 0, written

$$\frac{\partial}{\partial y}(X) \equiv 0 \quad (\text{A.59})$$

and

$$u_y \equiv 0, \quad (\text{A.60})$$

respectively, where X is any arbitrary variable.

Using the simplifications from equations A.59 and A.60, equations A.46, A.47, and A.48 become the elastic wave equations for inhomogeneous 2D VTI media can be written as

$$-\omega^2 \rho u_x = \frac{\partial}{\partial x} \left[c_{11} \frac{\partial u_x}{\partial x} + c_{13} \frac{\partial u_z}{\partial z} \right] + \frac{\partial}{\partial z} \left[c_{44} \left(\frac{\partial u_z}{\partial x} + \frac{\partial u_x}{\partial z} \right) \right] + f_x, \quad (\text{A.61})$$

and

$$-\omega^2 \rho u_z = \frac{\partial}{\partial x} \left[c_{44} \left(\frac{\partial u_z}{\partial x} + \frac{\partial u_x}{\partial z} \right) \right] + \frac{\partial}{\partial z} \left[c_{13} \frac{\partial u_x}{\partial x} + c_{33} \frac{\partial u_z}{\partial z} \right] + f_z. \quad (\text{A.62})$$

A.1.4.4 3D isotropic elastic wave equations

The isotropic wave equation has only two parameters in the elastic tensor: the shear modulus μ and Lamé's modulus of fluid incompressibility λ . Hooke's law for isotropic media in 3D can be written as

$$\begin{pmatrix} \sigma_{xx} \\ \sigma_{yy} \\ \sigma_{zz} \\ \sigma_{xy} \\ \sigma_{xz} \\ \sigma_{yz} \end{pmatrix} = \begin{pmatrix} \lambda + 2\mu & \lambda & \lambda & & & \\ \lambda & \lambda + 2\mu & \lambda & & & \\ \lambda & \lambda & \lambda + 2\mu & & & \\ & & & 2\mu & & \\ & & & & 2\mu & \\ & & & & & 2\mu \end{pmatrix} \begin{pmatrix} e_{xx} \\ e_{yy} \\ e_{zz} \\ e_{xy} \\ e_{xz} \\ e_{yz} \end{pmatrix}. \quad (\text{A.63})$$

In expanded form,

$$\begin{aligned} \sigma_{xx} &= \lambda(e_{xx} + e_{yy} + e_{zz}) + 2\mu e_{xx} \\ \sigma_{yy} &= \lambda(e_{xx} + e_{yy} + e_{zz}) + 2\mu e_{yy} \\ \sigma_{zz} &= \lambda(e_{xx} + e_{yy} + e_{zz}) + 2\mu e_{zz} \\ \sigma_{xy} &= 2\mu e_{xy} \\ \sigma_{xz} &= 2\mu e_{xz} \\ \sigma_{yz} &= 2\mu e_{yz}. \end{aligned} \quad (\text{A.64})$$

Substituting stress parameters from equation A.64 once again into Newton's motion equations A.38, A.39, and A.40 produces the elastic wave equations for inhomogeneous 3D isotropic media,

$$\begin{aligned} -\omega^2 \rho u_x &= \frac{\partial}{\partial x} \left[\lambda \left(\frac{\partial u_x}{\partial x} + \frac{\partial u_y}{\partial y} + \frac{\partial u_z}{\partial z} \right) + 2\mu \frac{\partial u_x}{\partial x} \right] + \frac{\partial}{\partial y} \left[\mu \left(\frac{\partial u_x}{\partial y} + \frac{\partial u_y}{\partial x} \right) \right] + \\ &\quad \frac{\partial}{\partial z} \left[\mu \left(\frac{\partial u_z}{\partial x} + \frac{\partial u_x}{\partial z} \right) \right] + f_x, \end{aligned} \quad (\text{A.65})$$

$$\begin{aligned} -\omega^2 \rho u_y &= \frac{\partial}{\partial x} \left[\mu \left(\frac{\partial u_y}{\partial x} + \frac{\partial u_x}{\partial y} \right) \right] + \frac{\partial}{\partial y} \left[\lambda \left(\frac{\partial u_x}{\partial x} + \frac{\partial u_y}{\partial y} + \frac{\partial u_z}{\partial z} \right) + 2\mu \frac{\partial u_y}{\partial y} \right] + \\ &\quad \frac{\partial}{\partial z} \left[\mu \left(\frac{\partial u_z}{\partial y} + \frac{\partial u_y}{\partial z} \right) \right] + f_y, \end{aligned} \quad (\text{A.66})$$

and

$$\begin{aligned} -\omega^2 \rho u_z &= \frac{\partial}{\partial x} \left[\mu \left(\frac{\partial u_z}{\partial x} + \frac{\partial u_x}{\partial z} \right) \right] + \frac{\partial}{\partial y} \left[\mu \left(\frac{\partial u_z}{\partial y} + \frac{\partial u_y}{\partial z} \right) \right] + \\ &\quad \frac{\partial}{\partial z} \left[\lambda \left(\frac{\partial u_x}{\partial x} + \frac{\partial u_y}{\partial y} + \frac{\partial u_z}{\partial z} \right) + 2\mu \frac{\partial u_z}{\partial z} \right] + f_z. \end{aligned} \quad (\text{A.67})$$

In a homogeneous medium, parameters μ and λ are constant and can thus move outside of the derivative operators. Let

$$\Theta = \frac{\partial u_i}{\partial x_i} = \left(\frac{\partial u_x}{\partial x} + \frac{\partial u_y}{\partial y} + \frac{\partial u_z}{\partial z} \right) = e_{xx} + e_{yy} + e_{zz} \quad (\text{A.68})$$

be the dilatation (change in volume). Substituting the dilatation Θ and moving the Lamé parameters outside of the derivative operators, equation A.65 (discarding the source term) produces

$$-\omega^2 \rho u_x = \lambda \frac{\partial \Theta}{\partial x} + 2\mu \frac{\partial u_x}{\partial x^2} + \mu \left(\frac{\partial u_x}{\partial y^2} + \frac{\partial u_y}{\partial y \partial x} \right) + \mu \left(\frac{\partial u_z}{\partial z \partial x} + \frac{\partial u_x}{\partial z^2} \right). \quad (\text{A.69})$$

A rearrangement of terms on the right hand side results in

$$-\omega^2 \rho u_x = \lambda \frac{\partial \Theta}{\partial x} + \mu \left(\frac{\partial u_x}{\partial x^2} + \frac{\partial u_y}{\partial y \partial x} + \frac{\partial u_z}{\partial z \partial x} \right) + \mu \left(\frac{\partial u_x}{\partial x^2} + \frac{\partial u_x}{\partial y^2} + \frac{\partial u_x}{\partial z^2} \right). \quad (\text{A.70})$$

In vector notation, $\left(\frac{\partial u_x}{\partial x^2} + \frac{\partial u_x}{\partial y^2} + \frac{\partial u_x}{\partial z^2} \right)$ can be written as $\nabla^2 u_x$, where $\nabla^2 : (\partial^2 / \partial x^2 + \partial^2 / \partial y^2 + \partial^2 / \partial z^2)$ is the Laplacian operator. By taking out a common partial derivative $\frac{\partial}{\partial x}$ from $\left(\frac{\partial u_x}{\partial x^2} + \frac{\partial u_y}{\partial y \partial x} + \frac{\partial u_z}{\partial z \partial x} \right)$ in equation A.70), we obtain

$$-\omega^2 \rho u_x = \lambda \frac{\partial \Theta}{\partial x} + \mu \frac{\partial \Theta}{\partial x} + \mu \nabla^2 u_x, \quad (\text{A.71})$$

which simplifies further to

$$-\omega^2 \rho u_x = (\lambda + \mu) \frac{\partial \Theta}{\partial x} + \mu \nabla^2 u_x. \quad (\text{A.72})$$

In a similar fashion, equations for the particle displacements u_y and u_z can be written as

$$-\omega^2 \rho u_y = (\lambda + \mu) \frac{\partial \Theta}{\partial y} + \mu \nabla^2 u_y \quad (\text{A.73})$$

and

$$-\omega^2 \rho u_z = (\lambda + \mu) \frac{\partial \Theta}{\partial z} + \mu \nabla^2 u_z, \quad (\text{A.74})$$

respectively. Combining equations A.72, A.73, and A.74, the vector elastic wave equation for homogeneous 3D isotropic media can be written (putting back the source term) as

$$-\omega^2 \rho u_i = (\lambda + \mu) \frac{\partial}{\partial x_i} \cdot \Theta + \mu \nabla^2 u_i + f_i, \quad (\text{A.75})$$

where u_i are the components of vector of particle velocities, $\partial/\partial x_i$ are the derivative components, and f_i are the source components. In 2D, the same derivation holds but with the constraint that the wavefield is defined in two dimensions (eg., x and z).

A.1.4.5 Thomsen parameters simplified with isotropic medium

In the isotropic case, Thomsen's parameters can be written as

$$\varepsilon \equiv \frac{c_{11} - c_{33}}{2c_{33}} \equiv 0, \quad (\text{A.76})$$

leading to

$$c_{11} = c_{33}.$$

The γ parameter is defined as

$$\gamma \equiv \frac{c_{66} - c_{44}}{2c_{44}} \equiv 0, \quad (\text{A.77})$$

leading to

$$c_{44} = c_{66}.$$

The δ parameter is defined as

$$\delta \equiv \frac{(c_{13} + c_{44})^2 - (c_{33} - c_{44})^2}{2c_{33}(c_{33} - c_{44})} \equiv 0, \quad (\text{A.78})$$

leading to

$$c_{13} = c_{33} - 2c_{44}.$$

The P-wave velocity and S-wave velocity then simplify to

$$v_P = \sqrt{\frac{c_{33}}{\rho}} = \sqrt{\frac{\lambda + 2\mu}{\rho}}, \quad (\text{A.79})$$

and

$$v_{SV} = v_{SH} = \sqrt{\frac{c_{44}}{\rho}} = \sqrt{\frac{2\mu}{\rho}}, \quad (\text{A.80})$$

respectively. There is no division of S-waves into SV-waves and SH-waves, because the phase angle θ no longer plays a role.

A.1.4.6 2D isotropic elastic wave equations

In 2D, the isotropic elastic tensor in 2D simplifies to a 3×3 matrix and can be written as

$$\mathbf{c}^{(\text{ISO-2D})} = \begin{pmatrix} c_{33} & c_{33} - 2c_{44} & \\ c_{33} - 2c_{44} & c_{33} & \\ & & c_{44} \end{pmatrix} = \begin{pmatrix} \lambda + 2\mu & \lambda & \\ \lambda & \lambda + 2\mu & \\ & & 2\mu \end{pmatrix}. \quad (\text{A.81})$$

The elastic wave equations for inhomogeneous 2D isotropic media become

$$-\omega^2 \rho u_x = \frac{\partial}{\partial x} \left[\lambda \left(\frac{\partial u_x}{\partial x} + \frac{\partial u_z}{\partial z} \right) + 2\mu \frac{\partial u_x}{\partial x} \right] + \frac{\partial}{\partial z} \left[\mu \left(\frac{\partial u_z}{\partial x} + \frac{\partial u_x}{\partial z} \right) \right] + f_x, \quad (\text{A.82})$$

and

$$-\omega^2 \rho u_z = \frac{\partial}{\partial x} \left[\mu \left(\frac{\partial u_z}{\partial x} + \frac{\partial u_x}{\partial z} \right) \right] + \frac{\partial}{\partial z} \left[\lambda \left(\frac{\partial u_x}{\partial x} + \frac{\partial u_z}{\partial z} \right) + 2\mu \frac{\partial u_z}{\partial z} \right] + f_z. \quad (\text{A.83})$$

The elastic wave equation for homogeneous 2D isotropic media is equation A.75, but only with vector components x and z .

A.2 Acoustic Wave Equation

In fluid media (in which shear stresses are not supported), a more simplified wave equation called the acoustic wave equation applies. For the acoustic case, all normal stresses are equal, such that

$$\sigma_{xx} = \sigma_{yy} = \sigma_{zz} = -\sigma, \quad (\text{A.84})$$

and the shear stresses are all zero,

$$\sigma_{xy} = \sigma_{xz} = \sigma_{yz} = 0, \quad (\text{A.85})$$

or in terms of the shear modulus,

$$\mu = 0. \quad (\text{A.86})$$

In the acoustic case, Newton's motion equations can be written as

$$-\omega^2 \rho u_x = \frac{\partial}{\partial x}(-\sigma_{xx}) + f_x, \quad (\text{A.87})$$

$$-\omega^2 \rho u_y = \frac{\partial}{\partial y}(-\sigma_{yy}) + f_y, \quad (\text{A.88})$$

and

$$-\omega^2 \rho u_z = \frac{\partial}{\partial z}(-\sigma_{zz}) + f_z. \quad (\text{A.89})$$

Combining equations [A.87](#), [A.88](#), and [A.89](#),

$$-\omega^2 \rho u_i = \frac{\partial}{\partial x_i}(-\sigma) + f_i, \quad (\text{A.90})$$

where u_i are the components of vector of particle velocities, $\partial/\partial x_i$ are the spatial derivative components, and f_i are the source components. Dividing by ρ and taking the divergence of both sides, we obtain

$$\omega^2 \frac{\partial u_i}{\partial x_i} = -\frac{\partial}{\partial x_i} \left(\frac{1}{\rho} \frac{\partial \sigma}{\partial x_i} \right) + \frac{\partial}{\partial x_i} \frac{1}{\rho} f_i \quad (\text{A.91})$$

Given $\mu = 0$, the new bulk modulus from equation [A.37](#) becomes $\kappa = \lambda$. The stress-strain relationship found in equation [A.63](#) reduces to

$$\sigma_{xx} = \kappa\Theta, \quad (\text{A.92})$$

$$\sigma_{yy} = \kappa\Theta, \quad (\text{A.93})$$

$$\sigma_{zz} = \kappa\Theta. \quad (\text{A.94})$$

Adding equations A.92, A.93, and A.94 and using the stress relation from equation A.84, we obtain

$$-\sigma = \kappa\Theta. \quad (\text{A.95})$$

Rearranging, we can solve for the dilatation,

$$\Theta = \frac{-\sigma}{\kappa}. \quad (\text{A.96})$$

Substituting the dilatation into equation A.91 and recalling that

$$\Theta = \frac{\partial u_i}{\partial x_i}, \quad (\text{A.97})$$

we obtain

$$\frac{-\omega^2}{\kappa}\sigma = -\frac{\partial}{\partial x_i} \left(\frac{1}{\rho} \frac{\partial \sigma}{\partial x_i} \right) + \frac{\partial}{\partial x_i} \frac{1}{\rho} f_i. \quad (\text{A.98})$$

Rearranging to isolate the source term on the right hand side, we obtain

$$\frac{\partial}{\partial x_i} \left(\frac{1}{\rho} \frac{\partial \sigma}{\partial x_i} \right) + \frac{\omega^2}{\kappa}\sigma = \frac{\partial}{\partial x_i} \frac{1}{\rho} f_i. \quad (\text{A.99})$$

If we use the relation of P-wave velocity in an isotropic medium, $c = \sqrt{\kappa/\rho}$, we can alternatively write the equation as

$$\frac{\partial}{\partial x_i} \frac{1}{\rho} \frac{\partial \sigma}{\partial x_i} + \frac{\omega^2}{c^2 \rho} \sigma = -s, \quad (\text{A.100})$$

where the source term is

$$s = -\frac{\partial}{\partial x_i} \frac{1}{\rho} f_i. \quad (\text{A.101})$$

A negative is assigned to the source because of a convention where inward pressure is defined as positive, and outward pressure is defined as negative. Equation [A.100](#) is the acoustic wave equation [2.16](#) defined in Chapter 2, Background Theory.

Appendix B

Well Data

The top-of-formation data that were used to construct two cross-sections shown in Figures 3.5 and 3.6 are presented in Tables B.1 and B.2. The top-of-formation data are publicly available from [ODNR Oil and Gas Resources Management \(2016\)](#). Additional common formations to Ohio are identified in the table, as they may aid in evaluating other strata beyond those identified.

Table B.1: Top-of-formation data in a south-to-north fashion are displayed here. Depths have been converted from depth in feet below kelly bushing (KB) to a common depth in metres below a datum of 426.7 m above mean sea level, the same datum used throughout the study. The 'KELLY_BUSHING_NEW' row at the top of the table presents the KB values referenced to the new datum. The numbers in brackets (#) indicate that values have been interpolated from surrounding data to build the cross-section. The key formations of interest are highlighted in yellow. Figure 3.5 shows the associated cross-section.

S ————— N

Well Abbreviations: Well Top Depth (m)

FORMATION	DF	LE	SB	ML	FW	GR	CC	BC	RR
KELLY_BUSHING_NEW	40	77	73	77	119	58	57	50	100
FRESH_WATER_STRATA						67			
FRESH_WATER_STRATA_B						105			
GLACIAL_DEPOSITS									
GLACIAL_DEPOSITS_B									
COAL					160				
COAL_B					161				
1ST_COW_RUN_SAND									
1ST_COW_RUN_SAND_B									
BUELL_RUN									
BUELL_RUN_B									
2ND_COW_RUN_SAND									
2ND_COW_RUN_SAND_B									
SALT_SAND									
SALT_SAND_B									
MAXTON_SAND									
MAXTON_SAND_B									

FORMATION	DF	LE	SB	ML	FW	GR	CC	BC	RR
KEENER_SAND									
KEENER_SAND_B									
BIG_INJUN_SAND	299	(333)	286	265	311	256	284	277	238
BIG_INJUN_SAND_B	335	368	345	344	347	288	317	(310)	314
SQUAW_SAND									
SQUAW_SAND_B									
MISSISSIPPIAN_SHALE									
MISSISSIPPIAN_SHALE_B									
WEIR_SAND									
WEIR_SAND_B									
BEREA_SANDSTONE	435	430	432	431	430	(407)	410	(403)	378
BEREA_SANDSTONE_B	449	446	467	447	450	(423)	425	(418)	393
BEDFORD_SHALE	449						425		
BEDFORD_SHALE_B							428		
2ND_BEREA_SANDSTONE									
2ND_BEREA_SANDSTONE_B									
OHIO_SHALE	449	446	467	447	(450)	(423)	(425)	(418)	393
OHIO_SHALE_B		1278	1276	1277					1216
GANTZ									
GANTZ_B									
THIRTY_FOOT									
THIRTY_FOOT_B									

FORMATION	DF	LE	SB	ML	FW	GR	CC	BC	RR
GORDON									
GORDON_B									
CINNAMON									
CINNAMON_B									
RHINESTREET_SHALE			(1276)						(1216)
RHINESTREET_SHALE_B									
MARCELLUS_SHALE	1284			1266				1253	
MARCELLUS_SHALE_B				1277					
BIG_LIME	1292	1278	1279	1277	(1280)	(1279)	(1277)	1261	1216
BIG_LIME_B		1406	1410	1752					1368
SYLVANIA									
SYLVANIA_B									
ORISKANY_SANDSTONE				1369				1275	1276
ORISKANY_SANDSTONE_B				1372					1278
BASS_ISLANDS_DOLOMITE				1399					
BASS_ISLANDS_DOLOMITE_B				1412					
HELDERBERG_LIMESTONE									
HELDERBERG_LIMESTONE_B									
SALINA_DOLOMITE	1477	1406	(1414)	(1412)	(1415)	1393	(1415)	1407	1368
SALINA_DOLOMITE_B		1647							1638
SALT_SECTION								1468	
SALT_SECTION_B									
NEWBURG									

FORMATION	DF	LE	SB	ML	FW	GR	CC	BC	RR
NEWBURG_B									
LOCKPORT_DOLOMITE	1666	1647	(1597)	1625	(1628)	1613		1672	1631
LOCKPORT_DOLOMITE_B		1760							1715
LITTLE_LIME	(1796)	(1760)	1679	1676	(1680)	(1728)	(1728)	1755	(1715)
LITTLE_LIME_B			1819						
PACKER_SHELL	1846	1823	1819	1813			(1745)	1798	1771
PACKER_SHELL_B		1840	1843	1832					1786
THOROLD_SANDSTONE									
THOROLD_SANDSTONE_B									
CLINTON_SANDS	1870	1848	(1843)	1834		(1810)		(1815)	1795
CLINTON_SANDS_B				1870					1835
STRAY_CLINTON_SAND		1848							
STRAY_CLINTON_SAND_B		1850							
RED_CLINTON_SAND		1850				1810		1815	1795
RED_CLINTON_SAND_B		1862							1804
WHITE_CLINTON_SAND		1862						1844	1807
WHITE_CLINTON_SAND_B									
WHITE_CLINTON_SAND_2		1873							1835
WHITE_CLINTON_SAND_2_B									
MEDINA_SAND		1896	1843						
MEDINA_SAND_B			1896						
MANITOULIN_SHALE									

FORMATION	DF	LE	SB	ML	FW	GR	CC	BC	RR
MANITOULIN_SHALE_B									
QUEENSTON	1948	1893	1896	1888		1846		1878	1849
QUEENSTON_B			1910						
UTICA_SHALE	2347	(2292)	2323	2314		2411	(2341)	2322	(2293)
UTICA_SHALE_B	2388	2334	2363	2354		2467		2362	(2348)
POINT_PLEASANT	2388	2334	2363	2354		2467	(2397)	2362	(2348)
POINT_PLEASANT_B				2393					
TRENTON_LIMESTONE				2393				2410	
TRENTON_LIMESTONE_B				2433					
BLACK_RIVER_GROUP				2433					
BLACK_RIVER_GROUP_B				2618					
GULL_RIVER				2618					
GULL_RIVER_B				2633					
GLENWOOD_SHALE				2633					
GLENWOOD_SHALE_B				2646					
KNOX_UNCONFORMITY				2646					
KNOX_UNCONFORMITY_B				2648					
BEEKMANTOWN_DOLOMITE				2648					
BEEKMANTOWN_DOLOMITE_B				2740					
ROSE_RUN_SANDSTONE				2740					
ROSE_RUN_SANDSTONE_B				2789					
TREMPEALEAU/COPPER_RIDGE				2789					
TREMPEALEAU/COPPER_RIDGE_B									

Table B.2: Top-of-formation data in a west-to-east fashion are displayed here. Depths have been converted from depth in feet below kelly bushing (KB) to a common depth in metres below a datum of 426.7 m above mean sea level, the same datum used throughout the study. The 'KELLY_BUSHING_NEW' row at the top of the table presents the KB values referenced to the new datum. The numbers in brackets (#) indicate that values have been interpolated from surrounding data to build the cross-section. The key formations of interest are highlighted in yellow. Figure 3.6 shows the associated cross-section.

W ————— E

Well Abbreviations: Well Top Depth (m)

FORMATION	SC	BG	BL	PR	MD	CC	SF	HY	ND	JO	BN
KELLY_BUSHING_NEW	56	76	59	65	82	57	97	42	85	59	75
FRESH_WATER_STRATA											
FRESH_WATER_STRATA_B											
GLACIAL_DEPOSITS											
GLACIAL_DEPOSITS_B											
COAL											
COAL_B											
1ST_COW_RUN_SAND											
1ST_COW_RUN_SAND_B											
BUELL_RUN											
BUELL_RUN_B											
2ND_COW_RUN_SAND											
2ND_COW_RUN_SAND_B											
SALT_SAND											
SALT_SAND_B											
MAXTON_SAND											
MAXTON_SAND_B											

FORMATION	SC	BG	BL	PR	MD	CC	SF	HY	ND	JO	BN
KEENER_SAND											
KEENER_SAND_B											
BIG_INJUN_SAND	230					284	246	283	233	327	292
BIG_INJUN_SAND_B	251					317	276	(316)	(266)	(360)	315
SQUAW_SAND											
SQUAW_SAND_B											
MISSISSIPPIAN_SHALE											
MISSISSIPPIAN_SHALE_B											
WEIR_SAND											
WEIR_SAND_B											
BEREA_SANDSTONE	385	397	401	408	416	410	421	428	432	468	429
BEREA_SANDSTONE_B	413	413	416		432	425	435	(442)	(446)	482	443
BEDFORD_SHALE						425			456	490	443
BEDFORD_SHALE_B						428					
2ND_BEREA_SANDSTONE											
2ND_BEREA_SANDSTONE_B											
OHIO_SHALE	413	413	416		432	(425)	(435)	(442)	(456)	(490)	(443)
OHIO_SHALE_B	1150	1183	1201		1244						
GANTZ											
GANTZ_B											
THIRTY_FOOT											
THIRTY_FOOT_B											

FORMATION	SC	BG	BL	PR	MD	CC	SF	HY	ND	JO	BN
GORDON											
GORDON_B											
CINNAMON											
CINNAMON_B											
RHINESTREET_SHALE	(1150)	(1183)	(1201)	1096	(1244)			1127		1212	
RHINESTREET_SHALE_B											
MARCELLUS_SHALE				1207				1285	(1297)	1323	1341
MARCELLUS_SHALE_B											
BIG_LIME	1150	1183	1201		1244	1277	1287	1295	1308	1331	1352
BIG_LIME_B	1645	1643	1679		1710						
SYLVANIA											
SYLVANIA_B											
ORISKANY_SANDSTONE				1230							
ORISKANY_SANDSTONE_B											
BASS_ISLANDS_DOLOMITE				1338							
BASS_ISLANDS_DOLOMITE_B											
HELDERBERG_LIMESTONE											
HELDERBERG_LIMESTONE_B											
SALINA_DOLOMITE	1355	1318			1383	1415	1426	1433		1478	1500
SALINA_DOLOMITE_B	1469	1578			1643					(1680)	1711
SALT_SECTION											
SALT_SECTION_B											
NEWBURG	1592		1648								

FORMATION	SC	BG	BL	PR	MD	CC	SF	HY	ND	JO	BN
NEWBURG_B	1609		1669								
LOCKPORT_DOLOMITE		1578	1600	1616	1643		1622	1646	1676	1680	1711
LOCKPORT_DOLOMITE_B		1643	1679		1710						
LITTLE_LIME	1659	(1693)	1716	(1732)	(1761)	(1728)	(1738)	(1759)	(1792)	(1796)	(1826)
LITTLE_LIME_B	1665		1722								
PACKER_SHELL	1675		1733	(1749)	1779	1745	(1781)	(1776)	(1809)	(1813)	(1843)
PACKER_SHELL_B	1690		1753		1798						
THOROLD_SANDSTONE											
THOROLD_SANDSTONE_B											
CLINTON_SANDS		1730	1759		1798		1840	(1857)	(1889)		(1963)
CLINTON_SANDS_B		1768	1792		1843						
STRAY_CLINTON_SAND	1694		1759		1798				1889	1938	
STRAY_CLINTON_SAND_B	1702		1766								
RED_CLINTON_SAND	1704		1767					1883			
RED_CLINTON_SAND_B	1718		1774								
WHITE_CLINTON_SAND	1720		1774	1752			1840				1971
WHITE_CLINTON_SAND_B	1732		1792		1843						
WHITE_CLINTON_SAND_2											
WHITE_CLINTON_SAND_2_B											
MEDINA_SAND	1745		1804								
MEDINA_SAND_B	1751		1810								
MANITOULIN_SHALE		1768									

FORMATION	SC	BG	BL	PR	MD	CC	SF	HY	ND	JO	BN
MANITOULIN_SHALE_B		1789									
QUEENSTON	1751	1789	1810	1816			1913	1930	1917	1978	2036
QUEENSTON_B							2341				
UTICA_SHALE	2183			2248		(2341)	2341	2381	2384	2417	2451
UTICA_SHALE_B	2231			2296		2397	2387	2475	2446	2465	2501
POINT_PLEASANT	2231			2296		2397	2387	2475	2446	2465	2501
POINT_PLEASANT_B											
TRENTON_LIMESTONE	(2272)			2337				(2515)	(2487)	(2505)	(2541)
TRENTON_LIMESTONE_B											
BLACK_RIVER_GROUP											
BLACK_RIVER_GROUP_B											
GULL_RIVER											
GULL_RIVER_B											
GLENWOOD_SHALE											
GLENWOOD_SHALE_B											
KNOX_UNCONFORMITY											
KNOX_UNCONFORMITY_B											
BEEKMANTOWN_DOLOMITE											
BEEKMANTOWN_DOLOMITE_B											
ROSE_RUN_SANDSTONE											
ROSE_RUN_SANDSTONE_B											
TREMPEALEAU/COPPER_RIDGE											
TREMPEALEAU/COPPER_RIDGE_B											

Curriculum Vitae

Name: Benjamin Consolvo

Post-Secondary Education and Degrees: University of Western Ontario
London, Ontario, Canada
2018 Master of Science in Geophysics

Crandall University
Moncton, New Brunswick, Canada
2012 Bachelor of Education

Queen's University
Kingston, Ontario, Canada
2010 Bachelor of Science (Honours) in Mathematics

Honours and Awards: Ontario Graduate Scholarship (OGS) of \$15,000 CAD
University of Western Ontario
09/2016 - 12/2017

Bill Nickerson Education Award
Canadian Society of Exploration Geophysicists
07/2017

Full Travel Scholarship to 2017 SEG/Chevron Student Leadership Symposium and SEG Annual Meeting
Society of Exploration Geophysicists / Chevron
09/2017

Full Travel Scholarship to 2016 SEG/ExxonMobil Student Education Program and SEG Annual Meeting
Society of Exploration Geophysicists / ExxonMobil
10/2016

Related Work Experience: Graduate Teaching and Research Assistant
University of Western Ontario
09/2015 - 12/2017

Geophysics Intern - FWI Research
ExxonMobil Upstream Research Company
01/2017 - 06/2017

Contract Processing Technician
Arcis Seismic Solutions (A TGS Company)
01/2015 - 02/2015

Geophysical Data Processor
EDCON-PRJ
10/2013 - 05/2014

Publications: Consolvo, B.P., Zuberi, M.A.H., Pratt, R.G., Cary, P.W, 2017, FWI with Scaled-Sobolev Preconditioning Applied to Short-Offset Vibroseis Field Data: Presented at the 79th Annual International Conference and Exhibition, EAGE, Extended Abstracts, doi: 10.3997/2214-4609.201701164